

Development of a Novel Capillary Based pH Gradient Elution Moving Boundary Electrophoresis Method and Electrolysis Free Device for Protein Separation and Concentration

by

Jeffrey Farnese

A thesis
presented to the University of Waterloo
in fulfillment of the
thesis requirement for the degree of
Master of Applied Science
in
Mechanical Engineering

Waterloo, Ontario, Canada, 2020

© Jeffrey Farnese 2020

Author's Declaration

I hereby declare that I am the sole author of this thesis. This is a true copy of the thesis, including any required final revisions, as accepted by my examiners.

I understand that my thesis may be made electronically available to the public.

Abstract

Proteins are the raw material input required for a number of biomedical purposes. In order to keep pace with the exponential demand for protein consumption from research institutions and biopharmaceutical companies, new developments in methods to isolate and collect proteins will be necessary. On top of that, as quantum computing becomes more widespread and accessible to all levels of protein researchers, the market will undoubtedly look for high quality products at lower costs. The current state of technology can be separated into two categories: high throughput and high resolution; however, there appears to be a gap in combining the two categories into a single method. The work presented in this thesis is an attempt at bringing these two categories together through capillary electrophoresis to meet future demands in protein research. Methods in capillary electrophoresis have proved extremely effective in precision manipulation of fluids and particles at the micron scale.

The new method, termed pH gradient elution moving boundary electrophoresis (pHGEMBE), separates proteins based on their isoelectric point (pI). The technique was inspired by the high resolution capabilities of isoelectric focusing (IEF), combined with the counter-flow gradient nature of gradient elution moving boundary electrophoresis. The fundamental principles of pHGEMBE were modelled numerically using COMSOL Multiphysics to predict protein behavior in an electric field. Experiments were carried out using commercially available capillary cartridges developed by Advanced Electrophoresis Solutions (AES). These capillary cartridges have a coating which suppresses electroosmotic flow (EOF), which removed a layer of complexity in the development of the new technique. Separation tests were carried out using fluorescent IEF markers, which have a

known isoelectric point, to visualize the separation process.

Validation of the process was performed on the CE Infinite analytical imaged capillary isoelectric focusing (iCIEF) system, made by AES. Electropherograms were produced for a control sample containing the initial mixture of markers, and of samples separated by the pHGEMBE process. The electropherograms showed complete separation of sample mixtures for markers with pI difference as low as 1.4 from their published values. A prototype system was designed and tested which incorporates all of the components to perform pHGEMBE for concentrating and separating up to four proteins. Recommendations for improving the resolution are discussed.

To mitigate negative effects associated with electrolysis during capillary electrophoresis techniques such as IEF, the capillary cartridge incorporates large reservoirs to isolate the separation capillary from the electrodes. To avoid electrolysis altogether, a low voltage separation device was designed and tested. This device uses a polymer membrane with track-etched pores to act as the separation capillary. Initial results demonstrated the ability to generate a large enough electric field to interact with the dye Ponceau S with as low as 0.7 volts, which is low enough to avoid electrolysis. The prototype device demonstrated that: (1) charged particles can be manipulated while avoiding electrolysis, and (2) the membrane design could be a practical way of constructing a future device capable of separating large sample volumes, not typical of convectional capillary electrophoresis methods.

Acknowledgements

I would like to begin by thanking my advisor, Dr. Carolyn L. Ren, who provided me the opportunity to explore freely, and develop a passion for a microfluidics under her guidance. Her support and council through this educational journey are truly appreciated.

The passionate and insightful discussions with members of the Microfluidics Group were incredibly valuable. I would like to offer my deepest gratitude to Matt Courtney who inspired the initial idea of the this new technique, provided excellent training and advice throughout my studies and was a pleasure to work with. I want to thank Dr. Tiemin Huang, who generously donated his time and use of equipment which was critical to the success of this project.

To all of my friends who have shown unwavering support throughout this long journey, I am truly privileged to have you in my life. We were separated physically, but always connected. I want to extend my thanks to some of the most important people in my life, Justin Yan, Clarke Stanbra, and Liam Lamont. To my love and CP, Stephanie Koelewijn, you have been a constant source of inspiration and all of my success is owed in part to you.

I want to thank my loving family, whose support cannot be understated. Especially my parents, who were always encouraging and supportive of all of my pursuits. Thank you.

Table of Contents

Author's Declaration	ii
Abstract	iii
Acknowledgements	v
List of Figures	xi
List of Tables	xiv
Nomenclature	xv
1 Introduction	1
1.1 Background	1
1.2 Applications	2
1.3 Thesis Objectives	2
1.4 Thesis Structure	4
2 Literature Review	5
2.1 Microfluidic Transport Phenomena	6
2.1.1 Fluid Flow	6
2.1.1.1 Governing Equations	6
2.1.1.2 Flow Regime (Stokes Flow)	6
2.1.1.3 Pressure Driven (Poiseuille) Flow	7
2.1.1.4 Hydraulic Resistance	9

2.1.1.5	Electroosmotic Flow	9
2.1.2	Electrophoresis	10
2.1.2.1	Electrolysis	11
2.1.2.2	Joule Heating	13
2.1.2.3	Temperature Effects	15
2.1.3	Mass Transport	17
2.1.3.1	Taylor Dispersion	18
2.2	Membrane Technologies	21
2.2.1	Membrane Characteristics	21
2.2.1.1	Bubble Point	21
2.2.1.2	Membranes in CIEF	22
2.2.2	Polycarbonate Track-Etched Membranes	23
2.3	Protein Separation Technologies	24
2.3.1	Protein Characteristics	24
2.3.1.1	Amino Acids and Proteins	24
2.3.1.2	Amino Acid Charge	25
2.3.1.3	Protein Sequence	25
2.3.1.4	Isoelectric Point	26
2.3.1.5	Charge Dependence	26
2.3.1.6	Electrophoretic Mobility	28
2.3.1.7	Diffusion Coefficient	28
2.3.2	IEF, CIEF	29
2.3.2.1	Collection Methods	30
2.3.3	GEMBE	31
2.3.4	Continuous Free-Boundary Flow-Electrophoresis	33
2.3.5	Ion-Exchange Chromatography	35

2.3.6	pH Gradient Ion-Exchange Chromatography	35
2.3.7	CZE	35
2.4	Buffers	36
2.4.1	Ionic Strength	36
2.4.2	Types of Buffers	36
2.5	Design Methods	37
2.5.1	Numerical Simulations (COMSOL)	38
3	Experimental Methods	39
3.1	pH Measurement	39
3.2	Reference Buffers	40
3.3	Sample Buffers	40
3.4	Pressure Pump	41
3.5	Syringe Pump	41
3.6	Syringes	42
3.7	Connectors	42
3.8	High Voltage Power Supply	44
3.9	Cheminert Selector and Microelectric Actuator	45
3.10	Capillary Cartridge	45
3.11	Fluorescent Markers	46
3.12	Fluorescent Microscopy	47
4	Capillary Electrophoresis pHGEMBE Separation Technique Development	49
4.1	Fundamental Equations	49
4.1.1	Mechanism Analysis	50
4.1.2	Peptide and Protein Mobilities	53
4.1.3	Fundamental Concepts	54
4.2	2D COMSOL Simulation	56

4.2.1	Velocity Field Equations	57
4.2.2	Transport of Diluted Species Equations	58
4.2.3	Electrostatics Equations	58
4.2.4	Equation Coupling	59
4.2.5	Peptide Simulation	59
4.2.6	Protein Simulation	60
4.3	IEF Marker Separations	64
4.3.1	Determining Experimental Parameters	64
4.3.1.1	Electric Field Response	64
4.3.1.2	Stacking Effect	66
4.3.1.3	Flow Rate	68
4.3.1.4	Conductivity	69
4.3.2	Concentration Factor	71
4.3.3	Separations	72
4.4	Instrumentation Prototyping	75
4.5	Recommendations	78
5	Development of a Low Voltage Protein Separation Device	80
5.1	Motivation	80
5.2	Development	81
5.2.1	Membrane and Electrode Selection	81
5.2.2	Chemicals	84
5.2.3	TEM Grid and Membrane Simulation (COMSOL)	84
5.2.4	Enclosure Design	88
5.3	Experimental Results	91
5.4	Recommendations	93

6	Conclusions and Recommendations	94
6.1	Recommendations for Future Works	94
6.1.1	High Resolution Separation	95
6.1.2	Electrolysis Free Protein Separations	95
	References	97
	Appendices	105
A	Test Logging	105
B	Mass Concentration Factor	108
C	Drawings	111

List of Figures

2.1	Change in Buffer pH Due to Electrolysis Products	12
2.2	Ohm's Law Plot for Buffers	14
2.3	Temperature Profile of Glass Capillary with Polyimide Coating	16
2.4	Taylor Dispersion of Initial Sample in a Microchannel	19
2.5	Dispersion under EOF and Pressure Driven Flow	20
2.6	Bubble Point Method Diagram	21
2.7	Capillary Cartridge Schematic	23
2.8	Guide to 20 Common Amino Acids	24
2.9	Titration Curve of Beta-Lactoglobulin	27
2.10	Titration Curves of 17 Model Proteins	28
2.11	CE Infinite Separation and Transfer Capillary	31
2.12	GEMBE Process Schematic	32
2.13	GEMBE Current Detection Results	33
2.14	Schematic of Continuous Free-Boundary Flow-Electrophoresis Apparatus .	34
3.1	Orion 5 Star Benchtop pH Meter	40
3.2	Capillary Adapter Manufacturing Process	43
3.3	Custom polymer tubing capillary adapter.	44
3.4	Syringe Assembly for Connecting to the Capillary Cartridge	44
3.5	Capillary Cartridge Image and Schematic	46

3.6	Mercury Burner Emission Spectrum	47
3.7	Dichroic Filter Spectrum	48
4.1	Linear Charge Relationship Versus pH Near the pI	50
4.2	Velocity Plot of two IEF Markers	52
4.3	Peptide Electrophoretic Mobilities as a Function of pH	53
4.4	Protein Electrophoretic Mobilities Versus pH	54
4.5	Process Diagram for pH Gradient Elution MBE	55
4.6	Simulation of Peptides in pH Step Environment	60
4.7	Simulation of proteins in pH Step Environment	61
4.8	Simulation one protein in pH Step Environment	62
4.9	Simulation one protein in pH Step Environment	62
4.10	Plot of Total Protein Molar Quantity Versus Time	63
4.11	Fluorescent Imaging Setup for pH Gradient Elution MBE	64
4.12	Image Intensity Analysis to Demonstrate Electric Field Influence on IEF Markers	65
4.13	Fluorescent Imaging of pI 7.6 Marker Stacking	67
4.14	Illustrated Technique to Approximate a Velocity Balance to Find Optimal Flow Rate	68
4.15	Experimentally Determined Tris Buffer Conductivity	71
4.16	Separation Results of pI 5.2 and 8.1 IEF Markers	73
4.17	Separation of pI 5.2, 7.6, and 8.1 IEF Markers	74
4.18	Automated Prototype Schematic	76
4.19	Solid Model of Syringe Adapter Components	76
4.20	Solid Model of Prototype Enclosure and Component Layout	77
4.21	Automated Prototype for performing pH Gradient Elution MBE	78
5.1	Ideal Membrane Pore and Electrode Configuration	82

5.2	TEM Grid with Tab and Membrane Pore Distribution in a Unit Cell	83
5.3	3D Electric Field Simulation of a TEM Grid Unit Cell and Membrane	85
5.4	2D Electric Field and Time Dependent Concentration Simulation of a Charged Species	86
5.5	2D Unit Cell Simulation of Concentration Field	87
5.6	Low Voltage Device Exploded View	89
5.7	LV System Assembly	90
5.8	Mesh Offset	90
5.9	Colour Image Results of the Separation of Ponceau S	92
5.10	Bubbles Generated from Electrolysis During Ponceau S Separations	92
5.11	Image of Membrane Deformation After Low Voltage Separations	93
A.1	Test Logging Form	106
A.2	Live Voltage and Current Plots from Test Log	107
B.1	Control Volume Analysis Diagram for Capillary Cartridge	108
C.1	Machine Drawing of the Proximal Connector	112
C.2	Machine Drawing of the Distal Connector	113

List of Tables

2.1	Electrolysis Reactions of Water	12
2.2	Amino Acid Letters in FASTA Format	25
2.3	Titration Curve Parameters	26
2.4	Commonly Used CE Buffers	37
3.1	IEF Marker Properties	47
4.1	Parameters for Generating a Velocity Plot	52
4.2	Experimental Determined Tris Buffer Conductivity	70
4.3	Buffer Compositions for Separating Three IEF Markers	73
5.1	PCTE Membrane Properties	82
5.2	TEM Grid Properties	83
5.3	Test parameters for Low Voltage Separation of Ponceau S	91

Nomenclature

Characters

Symbol	Description	Unit
A	constant in viscosity equation	1
B	buffer temperature constant in viscosity equation	K
c	concentration	$\text{mol} \cdot \text{m}^{-3}$
c_b	buffer concentration	$\text{mol} \cdot \text{m}^{-3}$
D	diffusion coefficient	$\text{m}^2 \cdot \text{s}^{-1}$
D_{eff}	effective diffusion coefficient	$\text{m}^2 \cdot \text{s}^{-1}$
D_h	hydraulic diameter	m
D_{pore}	pore diameter	m
e	elementary charge constant	$1.602 \times 10^{-19} \text{ C}$
E	electric field vector	$\text{V} \cdot \text{m}^{-1}$
E_z	axial electric field strength	$\text{V} \cdot \text{m}^{-1}$
F_d	hydrodynamic drag vector	N
f_m	mass concentration factor	1
g	gravity vector	$9.81 \text{ m} \cdot \text{s}^{-2}$
G	electrical conductance	S or Ω^{-1}
h	channel height	m
I	electrical current	A

k_b	Boltzmann's constant	$1.3806503 \times 10^{-23} \text{ m}^2 \cdot \text{kg} \cdot \text{K} \cdot \text{s}^{-2}$
k	thermal conductivity	$\text{kg} \cdot \text{m} \cdot \text{s}^{-3} \cdot \text{K}^{-1}$
K_a	acidic dissociation constant	1
L	length	m
M	molecular weight	Da or $\text{g} \cdot \text{mol}^{-1}$
\hat{n}	unit outward normal vector	1
p	pressure	Pa
p_c	capillary pressure	Pa
P	power	W
Pe	Peclet number	1
q	volumetric power generation (Joule heat)	$\text{W} \cdot \text{m}^{-3}$
Q	volumetric flow rate	$\text{m}^3 \cdot \text{s}^{-1}$
r	radial coordinate	m
r_s	hydrodynamic radius	m
\mathcal{R}	chemical species rate of production	$\text{mol} \cdot \text{L}^{-1} \cdot \text{s}^{-1}$
R	radius	m
R_1	inner radius of capillary	m
R_2	outer radius of capillary	m
R_c	outer radius of capillary with polyimide coating	m
R_h	hydraulic resistance	m
Re	Reynolds number	1
t	time	s
T	temperature	K
T_1	inner wall temperature of capillary	K
\mathbf{u}	velocity vector	$\text{m} \cdot \text{s}^{-1}$
\mathbf{u}_b	average bulk-flow velocity vector	$\text{m} \cdot \text{s}^{-1}$

\mathbf{u}_{ep}	electrophoretic velocity vector	$\text{m} \cdot \text{s}^{-1}$
u_{eof}	electroosmotic velocity	$\text{m} \cdot \text{s}^{-1}$
u_x	x component of velocity	$\text{m} \cdot \text{s}^{-1}$
u_y	y component of velocity	$\text{m} \cdot \text{s}^{-1}$
u_z	z component of velocity	$\text{m} \cdot \text{s}^{-1}$
\bar{u}_z	mean velocity in the axial direction, equivalent to u_b	$\text{m} \cdot \text{s}^{-1}$
V	electric potential	V
w	channel width	m
w_b	bolus width	m
\mathbf{x}	position vector	m
z	charge number	1
α	thermal diffusivity	$\text{m}^2 \cdot \text{s}^{-1}$
ϵ_0	permittivity of free space	$8.85419 \times 10^{-12} \text{ C}^2 \cdot \text{N}^{-1} \cdot \text{m}^{-2}$
ϵ_r	relative permittivity	1
Λ_b	equivalent buffer conductance	$\text{m}^2 \cdot \text{S} \cdot \text{mol}^{-1}$
η	dynamic viscosity	$\text{N} \cdot \text{s} \cdot \text{m}^{-2}$
ρ	density	$\text{kg} \cdot \text{m}^{-3}$
ρ_{el}	charge density	$\text{C} \cdot \text{m}^{-3}$
σ	conductivity	$\text{S} \cdot \text{m}^{-1}$
σ_b	buffer conductivity	$\text{S} \cdot \text{m}^{-1}$
μ	viscous mobility	$\text{m} \cdot \text{N}^{-1} \cdot \text{s}^{-1}$
μ_{eof}	electroosmotic mobility	$\text{m}^2 \cdot \text{V}^{-1} \cdot \text{s}^{-1}$
μ_{ep}	electrophoretic mobility	$\text{N} \cdot \text{s} \cdot \text{m}^{-1}$
λ	wave length	m
ζ	zeta potential	V

Operators

Symbol	Description
Δ	difference
∇	gradient operator
\cdot	dot product

Abbreviations

Acronym	Description
AES	Advanced Electrophoresis Solutions
APTES	(3-Aminopropyl)triethoxysilane
BSA	bovine serum albumen
CAPS	3-(Cyclohexylamino)-1-propanesulfonic acid
CE	capillary electrophoresis
CFD	computational fluid dynamics
CIEF	capillary isoelectric focusing
CYTC	cytochrome C
CZE	capillary zone electrophoresis
EDL	electric double layer
EOF	electroosmotic flow
FB	fractionation buffer
GEMBE	gradient elution moving boundary electrophoresis
HEPES	4-(2-hydroxyethyl)-1-piperazineethanesulfonic acid
HER	hydrogen evolution reaction
HPLC	high performance liquid chromatography
HV	high voltage

IEC	ion-exchange chromatography
IEF	isoelectric focusing
Mb	myoglobin
OER	oxygen evolution reaction
pI	isoelectric point
PCTE	polycarbonate track-etched
PVC	polyvinyl chloride
PVP	polyvinylpyrrolidone
PDMS	polydimethylsiloxane
SB	sample buffer
TEM	transmission electron microscopy
TDS	transport of diluted species

Chapter 1

Introduction

1.1 Background

The need to purify and isolate proteins represents a massive market in applications such as proteomics, protein therapeutics, and disease diagnostics. MarketWatch predicts the global purification and isolation market is expected to exceed \$8.0 billion USD by 2024 at a compound annual growth rate of 8% [1]. As microfluidic systems and devices advance, they have seen large growth as a platform geared towards biological separations, with over 200 publications in 2016 referencing the terms "separations" and "microfluidics" together [2]. Microfluidic separation technologies include capillary isoelectric focusing (CIEF), capillary zone electrophoresis (CZE), and gradient elution moving boundary electrophoresis (GEMBE). These technologies are discussed in more detail in Chapter 2. These techniques offer high resolution separations and small reagent consumption but perform separations at lower rates compared to other techniques. One of the challenges of CIEF is collecting the separated samples while avoiding a phenomenon called Taylor dispersion, which reduces the concentration of the separated samples and can cause separated samples to partially combine. A different group of methods for performing separations are pressure driven chromatography techniques. High performance liquid chromatography (HPLC) is a popular method for high throughput separations, but is limited in resolution for in sepa-

rating proteins which have either similar properties or are of low abundance compared to electrophoretic techniques [2]. With this said, there appears to be an opportunity to develop a technique which offers both high resolution and high throughput.

1.2 Applications

The purpose of separating proteins includes proteomics, drug development, and capture of therapeutic proteins. Proteomics is the study of proteins in regard to their structure and function in biological samples. Chandramouli [3] lists several uses for proteomics which include proteome profiling to determine their characteristics, comparative expression analysis between two or more proteins, and studying interactions between two proteins. Proteomic technologies are used to identify certain diseases based on the behaviour of proteins such as protein pathways and signaling cascades [4]. Proteomics has had many successes such as the Human Proteome Project, but there still exists the problem of collecting low abundant proteins in a high enough concentration to perform analysis [4]. Personalised medicine requires an understanding of low abundant proteins which act as a signal in early diagnosis of diseases [5]. The challenge in collecting enough low abundant proteins becomes a bottleneck in the supply-chain of creating personalized treatments for patients. Therapeutic proteins can require dosages as low as tens of nanograms to a few milligrams per day [3]. Insulin requires 1.4 to 2.8 milligrams per day for a 70kg person [6]. This data gives a sense for the scale of protein consumption, and as advancements in personalized treatments are made, the demand will only grow.

1.3 Thesis Objectives

This thesis attempts to address the aforementioned opportunity to create a microfluidic technique that can separate proteins with equal or greater separation resolutions compared to IEF, while achieving them at a higher rate. The major advantage of using microfluidics is the precise nature in which incredibly small quantities of fluids can be controlled

or manipulated [7]. Since the sizes of peptides and proteins are at the nanometer scale, miniaturizing technologies closer to this scale makes sense, hence, microfluidics. The fundamental physics of fluid flows at the micron scale are well understood but are very different compared to our daily experience. Transport phenomena at low Reynolds numbers is where viscosity is dominant and inertia is negligible [8]. This means there is no turbulence and flows are generally smooth and continuous. Fluids and particles at the micron scale effectively reach terminal velocity instantaneously which significantly simplifies the mathematics as there are very few time dependent properties. However, proteins are smaller than the micron scale, giving rise to coefficients of diffusion which act on a time scale that can significantly influence their concentrations and plays a large role in Taylor dispersion. Nevertheless, with the use of numerical simulations this time dependent parameter can be accurately predicted. Another advantage of microfluidics is the low reagent consumption of processes. Experiments at this scale can be carried out faster and at lower costs compared to using other analytical techniques.

The major objectives of this thesis are to:

1. Develop a technique for separating proteins based on their isoelectric point,
2. Simulate the proposed technique to investigate its effectiveness,
3. Use standard equipment and components to perform the separation technique,
4. Design and construct a low-cost prototype which can perform separation of up to three peptides,
5. Validate the process by using a third-party platform,
6. Evaluate the performance of the technique and make recommendations for future improvements,
7. Develop a low voltage device which can perform separations while avoiding the effects of electrolysis,
8. Evaluate the performance of a low voltage device and make recommendations for future improvements.

1.4 Thesis Structure

Chapter 2 provides an overview of the fundamental equations used in microfluidics applications. The chapter highlights the most important aspects of developing an electrophoretic based technique. An overview of what proteins are and their properties, and how they can be manipulated is then presented. The rest of the chapter discusses the state of current separation technologies, and design methods available in microfluidics.

Chapter 3 describes the basic measurement techniques used throughout the thesis, and the types of chemicals and equipment used.

In Chapter 4, the novel pH gradient elution moving boundary electrophoresis method is introduced. The fundamental relationships associated with it are described with increasing complexity. Numerical simulations capture the time dependent nature of the concentration field and provide insight into the appropriate values for generating the electric field and the setting up an appropriate flow field. The experimental setup and preliminary results of this new technique using fluorescent peptides are detailed. The validation of the technique is done by using a commercial protein analysis platform, CE Infinite, which shows separations occurred as expected. Finally, the development of a standalone prototype system is reviewed, highlighting the low cost of development.

Chapter 5 describes the development of a low voltage device with the purpose of performing separations while avoiding electrolysis. This device is intended to be a proof of concept in generating an electric field within the pores of track-etched membranes. Tests are performed using Ponceau S which has a constant net charge that is independent of pH. The qualitative results are presented and future tests and improvements to experiments are suggested.

Chapter 6 presents a summary of the work contained in this thesis. Improvements to the novel technique are recommended to achieve higher resolution separations. Recommendations for improving the low voltage device are made, as well as a potential pathway for achieving high throughput separations.

Chapter 2

Literature Review

Developing a new method for performing protein separations using electrophoresis requires knowledge from many different disciplines besides mechanical engineering, which include biology, chemistry, physics, and electrical engineering. Mechanical engineers in general develop components and systems which move based on energy transformations. Understanding how these systems interact with each other at the microscale and how to precisely manipulate them for specific purposes is at the heart of the field of microfluidics.

This chapter provides the necessary background information for understanding the behaviour of chemical species, in this case proteins, influenced by electrokinetic forces. The basics of transport phenomena are discussed which describe the effects and limitations of manipulating flows and chemical species in a microscale environment. A brief discussion of acid-base chemistry and how it relates to electrophoresis is provided. This is followed by information on heat generation and mass transport of chemical species. A review on membranes and their role in capillary electrophoresis (CE) is briefly covered. The fundamental properties of proteins which can be used to control their behaviour for the specific purpose of separating different proteins are presented. This is followed by an introduction of current methods used for protein analysis and collection. Finally, a background on the design methods used to develop a new separation technique is discussed.

2.1 Microfluidic Transport Phenomena

2.1.1 Fluid Flow

In microfluidic systems, the physics of fluid flows are very different compared to macroscale flows experienced in daily life, such as aerodynamic flows or simple pipe flow. However, the starting point for determining the important physics remains the same which is the Navier-Stokes equation. This thesis assumes that the fluids being examined are Newtonian with a constant viscosity and are incompressible.

2.1.1.1 Governing Equations

The general Navier-Stokes equation is a momentum balance equation [9]:

$$\rho \left(\frac{\partial \mathbf{u}}{\partial t} + \mathbf{u} \cdot (\nabla \mathbf{u}) \right) = -\nabla p + \eta \nabla^2 \mathbf{u} + \rho \mathbf{g} + \rho_{el} \mathbf{E} \quad (2.1)$$

where ρ is the density, \mathbf{u} is the velocity vector, p is the pressure, η is the fluid viscosity, ρ_{el} is the charge density, \mathbf{E} is the electric field, and \mathbf{g} is the gravitational field. It is also common that the gravitational and electric body forces are expressed as a single generic body force term.

To enforce a fluid to be incompressible, the continuity equation is written as:

$$\nabla \cdot \mathbf{u} = 0 \quad (2.2)$$

where it is assumed that the density of the fluid does not change with respect to space and time and can be assumed to be constant [9].

2.1.1.2 Flow Regime (Stokes Flow)

Many applications of microfluidics rely on the assumption that at small scales, the viscosity of the fluid becomes the dominant force compared to inertial forces. This is evaluated

through the dimensionless Reynolds number which is given by:

$$Re = \frac{\rho u_b D_h}{\eta} \quad (2.3)$$

where D_h is the hydraulic diameter of the fluid channel, u_b is the average bulk flow velocity, η is the dynamic viscosity, and ρ is the density of the fluid. In the case of a circular channel, the hydraulic diameter this is simply the diameter of the channel [10]. Since the diameter for microfluidic applications is in the micron range, the Reynolds number is generally much less than one. Assuming Reynolds numbers much less than one and ignoring body forces allows for the simplification of the Navier-Stokes equation, which reduces to the Stokes equation [9]:

$$0 = -\nabla p + \eta \nabla^2 \mathbf{u} \quad (2.4)$$

From the Stokes equation, the drag force on a sphere is found to be:

$$\mathbf{F}_d = 6\pi\eta r_s \mathbf{u} \quad (2.5)$$

where r_s is the radius of the sphere, \mathbf{u} is the velocity of the sphere, and η is the dynamic viscosity of the fluid. This result is extremely important and powerful in modeling the behavior of particles that are near spherical.

2.1.1.3 Pressure Driven (Poiseuille) Flow

Upon application of a pressure gradient in a microchannel the resulting flow is described as Poiseuille flow. Kirby [10] makes the distinction between Poiseuille flow and Hagen-Poiseuille flow as the latter being specifically for pressure-driven flow in a microchannel with a circular cross section. Using Equation 2.4 and cylindrical coordinates, the velocity field is given by:

$$\mathbf{u}_z(r) = -\frac{1}{4\eta} \frac{\partial p}{\partial z} (R^2 - r^2) \quad (2.6)$$

where \mathbf{u}_z is the velocity in the axial direction and R is the radius of the tube. The volumetric flow rate is obtained by integrating the velocity field with respect to the cross-sectional area and yields:

$$Q = \int_0^R \int_0^{2\pi} \mathbf{u}_z(r) r d\theta dr = -\frac{\pi R^4}{8\eta} \frac{\partial p}{\partial z} \quad (2.7)$$

where Q is the volumetric flow rate. Assuming the pressure gradient is linear and uniform, the volumetric flow rate can be written as:

$$Q = \frac{\pi R^4}{8\eta} \frac{\Delta p}{L} \quad (2.8)$$

where L is the length of the channel for which the pressure drop is defined. ΔP is defined as $p_{in} - p_{out}$, where $p_{out} < p_{in}$. Therefore, $-\frac{\partial p}{\partial z}$ can be replaced with $\frac{\Delta p}{L}$ [10]. The mean velocity is simply the volumetric flow rate divided by the cross-sectional area:

$$\bar{\mathbf{u}}_z = \frac{Q}{A_c} = \frac{\Delta p}{L} \frac{R^2}{8\eta} \quad (2.9)$$

Bruus [9] lists a variety of Poiseuille flow solutions for other microchannel cross sections such as an ellipse and triangle, which have analytical solutions. The rectangular cross section, which is common when using photolithography techniques to make microfluidic chips, does not have a known analytical solution. The flow field is best described using a Fourier series [9]. The volumetric flow rate in a rectangular cross section is given by:

$$Q = \frac{h^3 w}{12\eta} \frac{\Delta p}{L} \left[1 - \sum_{n, \text{odd}}^{\infty} \frac{192}{(n\pi)^5} \frac{h}{w} \tanh\left(n\pi \frac{w}{2h}\right) \right] \quad (2.10)$$

The sum can be approximated as:

$$Q = \frac{h^3 w \Delta p}{12\eta L} \left[1 - 0.630 \frac{h}{w} \right], \text{ for } h \leq w. \quad (2.11)$$

where h and w are the height and width of the channel respectively. The aspect ratio is defined as $\frac{h}{w} \leq 1$ for this equation. When discussing aspect ratios in the context of microfabrication, the channel height is the pattern height and the aspect ratio can be greater than 1 [11]. Therefore, when using Equation 2.11 where the pattern height is greater than the pattern width, the pattern height and width become w and h respectively. Bruus [9] states that the error in Equation 2.11 when $h = w$ and when $h = \frac{w}{2}$ is 13% and 0.2% respectively.

2.1.1.4 Hydraulic Resistance

Due to the linear relationship between flow rate and pressure, the flow rate can be written in terms of hydraulic resistance giving the Hagen-Poiseuille Law:

$$Q = \frac{\Delta p}{R_h} \quad (2.12)$$

where the hydraulic resistance for a circular channel is defined as:

$$R_h = \frac{8\eta L}{\pi R^4} \quad (2.13)$$

This relationship is analogous to Ohm's law for an electrical circuit, and thus, techniques for circuit analysis such as Kirchhoff's laws are valid to use.

2.1.1.5 Electroosmotic Flow

Electroosmotic flow (EOF) occurs when there is an electric double layer (EDL) present in an applied electric field. The flow profile is represented by a plug-like velocity profile. In this thesis the EOF is ignored due to the use of EOF suppressant coatings applied to the capillary walls as discussed in Section 3.10. A detailed description and derivation of EOF,

EDL, and the zeta potential is beyond the scope of this review. References available for these topics include: Bruus [9], Kirby [10], Glawdel [12].

The Helmholtz-Smoluchowski equation for EOF velocity is given by:

$$u_{eof} = \mu_{eof} E_z \quad (2.14)$$

where E_z is the electric field strength parallel in the axial direction of the channel, and μ_{eof} is the electroosmotic mobility of the fluid defined by:

$$\mu_{eof} = -\frac{\epsilon_0 \epsilon_r \zeta}{\eta} \quad (2.15)$$

where ϵ_0 is the permittivity of free space, ϵ_r is the relative permittivity of the fluid, and ζ is the zeta potential. The zeta potential is a function of the electrolyte ionic strength and the wall material. The flow profile of EOF is assumed to be plug-like and uniform with the assumption of a slip velocity at the wall. The slip velocity assumption comes from the thin, oppositely charged EDL, where Coulomb forces induced by the electric field cause the ions in the EDL to migrate. Since the thickness of the EDL is typically much smaller than the diameter of the channel, the bulk flow appears to move with a profile that is plug-like outside of the EDL region [10]. The zeta potential for a glass wall was reported as -88 to -66 mV, depending on the type and concentration of the electrolyte [13]. This holds true when the channel size is much larger than the EDL such that changes in the velocity profile can be ignored.

2.1.2 Electrophoresis

Electrophoresis is the movement of charged particles in a fluid in the presence of a uniform electric field. A charged species will experience a force in an electric field given by:

$$F_e = zeE \quad (2.16)$$

where F_e is the electric body force, z is the charge number, and e is the elementary charge constant, 1.6×10^{-19} C. Equating the drag force to the electric force and solving for the velocity yields:

$$\mathbf{u}_{ep} = \frac{ze}{6\pi\eta r_s} \mathbf{E} \quad (2.17)$$

The electrophoretic mobility, μ_{ep} is defined as:

$$\mu_{ep} = \frac{ze}{6\pi\eta r_s} \quad (2.18)$$

where in the case of an ion or protein, r_s is the hydrated radius. This mobility is now a property of the charged particle. To relate the diffusivity and electrophoretic mobility of an ion or protein, the Nernst-Einstein relation can be used:

$$\mu_i = \frac{\mathcal{D}_i}{k_B T} = \frac{\mu_{ep,i}}{z_i e} = \frac{1}{6\pi\eta r_s} \quad (2.19)$$

where μ_i is the viscous mobility, \mathcal{D}_i is the diffusion constant, k_b is Boltzmann's constant, T is temperature, and z is the charge number; all of which are with respect to species i [10]. The electrophoretic velocity profile of a species in a uniform electric field will be uniform i.e. there will be no variation in velocity in the radial direction.

2.1.2.1 Electrolysis

Electrolysis of water occurs with the application of a potential difference between submerged electrodes and produces changes in pH and generates oxygen and hydrogen gas bubbles. [12, 14–16]. In CE applications, oxygen is produced at the anode and often referred to as the oxygen evolution reaction (OER), hydrogen is produced at the cathode and called the hydrogen evolution reaction (HER) [17]. The reactions for the electrolysis of water are given in Table 2.1.

Table 2.1 Oxygen and Hydrogen Evolution Reactions for Water. Source: [17]

	Acidic Solution	Basic Solution
Anode (OER)	$2H_2O \rightarrow 4H^+ + 4e^- + O_2$	$4OH^- \rightarrow 4e^- + O_2 + 2H_2O$
Cathode (HER)	$2H^+ + 2He^- \rightarrow H_2$	$2H_2O + 2e^- \rightarrow H_2 + 2OH^-$

From the table it is clear that the anode reduces the local pH with the production of protons in acidic solutions and the removal of hydroxide ions in basic solutions. The opposite is true at the cathode.

Persat [17] compared the effects of tris and acetate buffers in electrode reservoirs to map their changes in pH over time under constant applied voltage as shown in Figure 2.1.

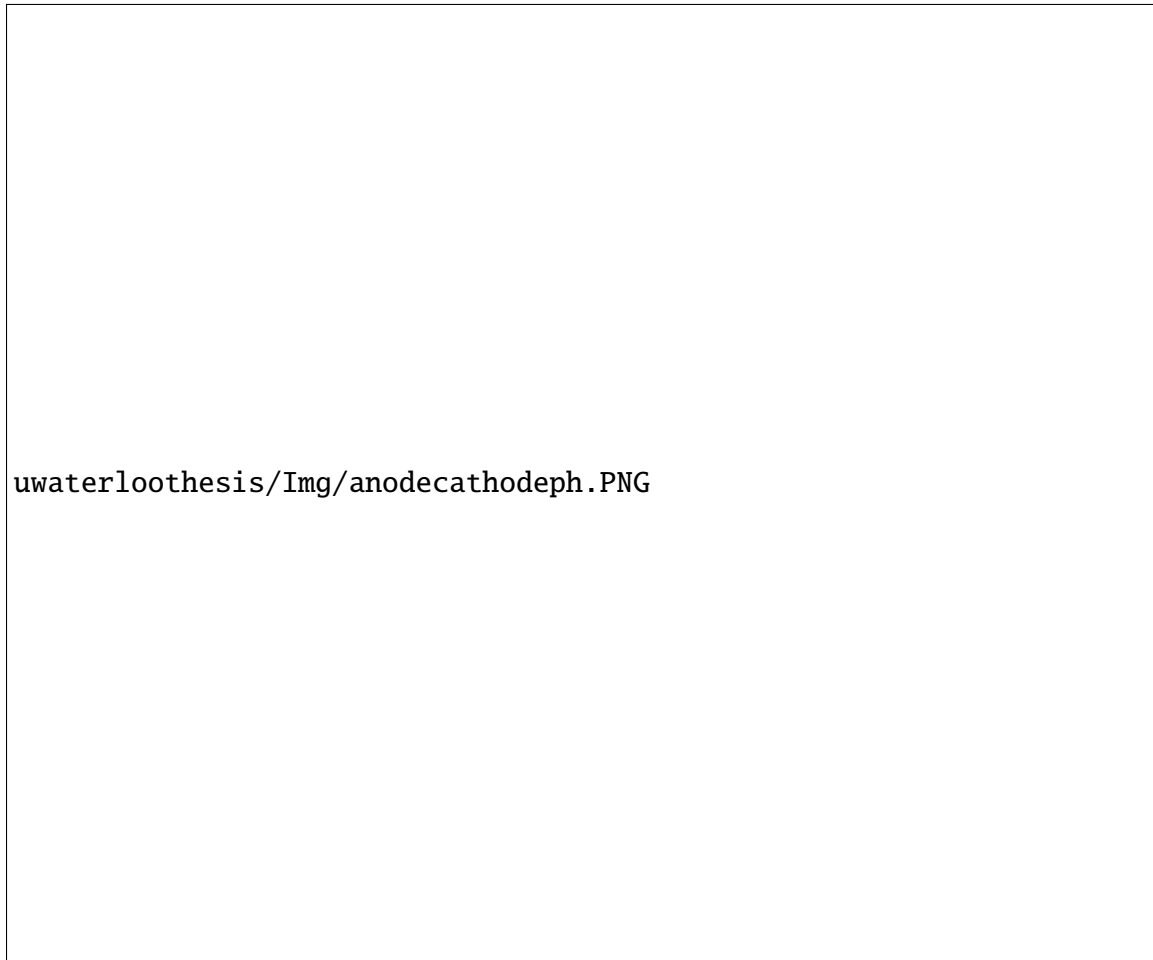


Figure 2.1 Local changes in pH near the electrodes for Tris and acetate buffers under constant applied 2.5 kV voltage. (a) 10mM Tris at the anode; (b) 10 mM Tris at the cathode; (c) 10 mM acetate at the anode; (d) 10 mM acetate at the cathode. Source: [17].

Persat [17] notes that for the Tris buffer at the anode, when the pH is below the pK_a , the pH can drop quickly over time. For the acetate buffer in the cathode reservoir, the pH values above the pK_a will cause the pH to increase quickly as hydroxide ions are produced and push the pH out of the buffering capacity range.

Electrochemically stable electrodes made from platinum are usually the best choice as they will not react with the electrolysis products [12, 17].

2.1.2.2 Joule Heating

Joule heating is an induced temperature increase caused by the electric current in the capillary electrophoresis (CE) systems. Joule heating in CE produces undesirable effects such as band broadening in isoelectric focusing, deterioration of analytes [18], as well as dramatic changes in pH for buffers with a strong temperature dependency such as tris [19]. Excessive Joule heating is influenced by three major factors: capillary properties such as material and dimensions, buffer type, and applied electric field. To reduce the effects of Joule heating from a capillary property perspective, larger surface-to-volume ratios should be used to adequately dissipate the excessive heat [20], or use a longer capillary [18]. The high surface-to-volume ratio of small diameter capillaries allows for more effective heat transfer. The ionic strength (molar concentration) of buffers can play an important role in excessive Joule heating. An Ohm's Law Plot can be made to determine the acceptable amount of Joule heating that a buffer and capillary combination can effectively dissipate. Figure 2.2 shows the Ohm's Law Plot of a phosphate, CAPS (3-(Cyclohexylamino)-1-propanesulfonic acid) and borate buffer of equal 100mM ionic strengths.

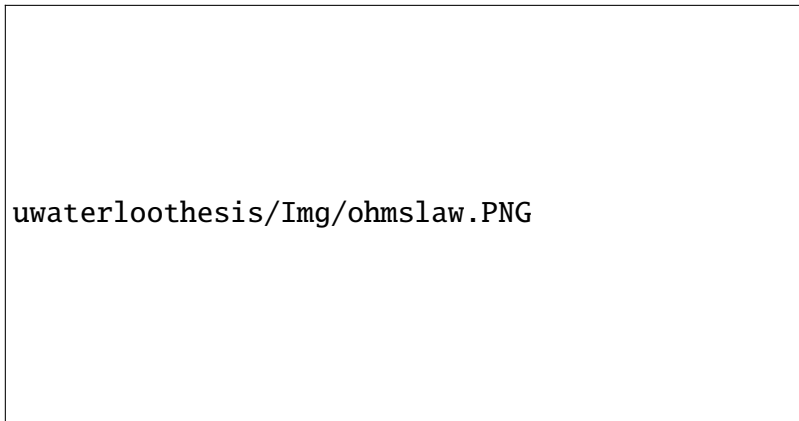


Figure 2.2 (a) An example of an Ohm's Law Plot for three buffers: 100 mM phosphate, pH 2.5; 100 mM CAPS, pH 11.0; 100 mM borate.(b) A plot of current versus applied voltage for 100 mM CAPS. Source: [18].

The phosphate and CAPS buffers show deviations away from their respective linear trendlines at large applied voltages, indicating excessive Joule heating and an inability to dissipate heat effectively. The borate buffer shows a high degree of temperature stability due to the highly linear relationship between current and voltages up to 30kV.

Mitigation of Joule heating is fundamental to building a robust CE system. Joule heat, P , is the resistive power generated from electrical current, I , flowing through an electrolyte [18]. Joule heat is calculated by:

$$P = IV \quad (2.20)$$

where V is the applied voltage. The electrical conductance is the inverse of resistance and is calculated by:

$$G = \frac{I}{V} \quad (2.21)$$

Ross [21] developed a temperature measurement technique using fluorescent microscope and dye to determine the effects of Joule heating. The average temperature of a 20 mM Carbonate buffer of pH 9.4 with Rhodamine B used as the fluorescent dye was found to change by 10°C in approximately 5 seconds after applied electric field of 1000 V/cm. He

also found the radial temperature profile of the capillary begins to deviate from a uniform profile to a parabolic profile at temperatures above 30°C.

2.1.2.3 Temperature Effects

To perform any CE experiments, care should be taken to mitigate temperature effects as it can influence many parameters of CE experiments [18]. With respect to electrophoretic mobility of ions or constant charge molecules, temperature gradients within the capillary will introduce viscosity gradients in the radial direction of the tube [22]. This viscosity gradient will introduce an electrophoretic velocity profile that varies radially.

Grushka [22] modelled the temperature dependent viscosity by:

$$\eta(T) = Ae^{(B/T)} \quad (2.22)$$

where A and B are experimentally determined coefficients for a given liquid, and T is the temperature. The viscosity of a buffer which is assumed to be identical as water is given as [23]:

$$\eta(T) = 2.761 \times 10^{-6} e^{(1713/T)} \quad (2.23)$$

The temperature profile from the surrounding environment to the center of the capillary is shown in Figure 2.3.

uwaterloothesis/Img/capillarytemperatedistribution.pdf

Figure 2.3 Schematic of the temperature profile from the surrounding environment to the center of a fused silica capillary with a polyimide coating.

The temperature at the center of a fused silica capillary with a polyimide coating is given by:

$$T_0 = T_a + \frac{qR_1^2}{2} \left[\frac{1}{2k_1} + \frac{1}{k_2} \ln \left(\frac{R_2}{R_1} \right) + \frac{1}{k_c} + \frac{1}{k_2} \ln \left(\frac{R_c}{R_2} \right) + \frac{1}{R_c h} \right] \quad (2.24)$$

where T_a is the ambient temperature far from the outside of the capillary, R_1 is the internal capillary radius, R_2 and R_c is the outside capillary radii without and with the coating respectively, k_1 , k_2 and k_c are the thermal conductivities of the buffer solution, fused silica, and polyimide coating respectively, and h is the heat transfer coefficient to the ambient surroundings.

To find the internal wall temperature of a fused silica capillary with a polyimide coating the equation above is modified to:

$$T_1 = T_a + \frac{qR_1^2}{2} \left[\frac{1}{k_2} \ln \left(\frac{R_2}{R_1} \right) + \frac{1}{k_c} + \frac{1}{k_2} \ln \left(\frac{R_c}{R_2} \right) + \frac{1}{R_c h} \right] \quad (2.25)$$

Equation 2.25 can be modified for the absence of a coating by letting $R_c = R_2$ which yields:

$$T_1 = T_a + \frac{qR_1^2}{2} \left[\frac{1}{k_2} \ln \left(\frac{R_2}{R_1} \right) + \frac{1}{R_2 h} \right] \quad (2.26)$$

Grushka [22] derived a parabolic electrophoretic flow profile in capillary zone electrophoresis using Equation 2.25, which includes the contribution from the uniform electroosmotic flow profile, and the parabolic EOF component attributed to the viscosity gradient:

$$u(r) = u_1 \left[1 + \frac{qBR_1^2}{4k_1T_1^2} \left(1 - \frac{r^2}{R_1^2} \right) \right] \quad (2.27)$$

where u_1 is the electroosmotic velocity at the wall and k_b is the thermal conductivity of the buffer. q is the heat per volume generated within the capillary and can be written in several useful ways:

$$q = \frac{IV}{\pi R_1^2 L} = \frac{IE}{\pi R_1^2} = \frac{I^2}{\sigma A_c^2} \quad (2.28)$$

where σ is the buffer conductivity and A_c is the cross-sectional area of the capillary. q also relates to the equivalent conductance for a buffer solution:

$$\Lambda_b = \frac{q}{c_b E^2} \quad (2.29)$$

where Λ_b is the equivalent buffer conductance, and c_b is the ‘concentration of the buffer.

The temperature dependent electrical conductivity of a solution can be written as [12]:

$$\sigma(T) = \sigma_0(1 + 0.02(T - T_0)) \quad (2.30)$$

2.1.3 Mass Transport

The migration of a species in electrophoresis can be described by the following equation [24]:

$$\frac{\partial c_i}{\partial t} + \nabla(c_i \mathbf{u} + c_i \mathbf{u}_{ep,i}) = \mathcal{D}_i \nabla^2 c_i \quad (2.31)$$

Where c_i is the molar concentration of species i , \mathbf{u} is the velocity field, $\mathbf{u}_{ep,i}$, is the electrophoretic migration velocity, and \mathcal{D}_i is the diffusion coefficient of species i .

2.1.3.1 Taylor Dispersion

To describe how the concentration of a species changes over time in the presence of Poiseuille flow within a microchannel, the Peclet number and length ratio are needed. The Peclet number, Pe , is defined as:

$$Pe = \frac{u_b R}{\mathcal{D}} \quad (2.32)$$

where u_b is the average bulk flow velocity and R is the characteristic length of the microchannel by which diffusion of the species occurs. In the case of a tube, R is the radius. The length ratio is defined as L/R . Figure 2.4 illustrates how the concentration of an initial bolus of sample with a circular cross-section (Figure 2.4(a)) evolves in the presence of Hagen-Poiseuille flow.



Figure 2.4 Evolution of a sample bolus within a microchannel due to Taylor dispersion. The reduction in colour intensity represents the reduction in sample concentration.

The initial deformation of the bolus in Figure 2.4(b) occurs in a state of pure convection which can be assumed when $Pe \gg L/R$. In pure convection the diffusion of the species in the axial or radial direction can be neglected. As the sample moves along the channel, the length ratio increases to be the same magnitude as the Peclet number as shown in Figure 2.4(c). Eventually a state of convection-diffusion is reached where $Pe \ll L/R$ and the bolus of sample appears to be a wider rectangular concentration profile compared to the initial state as shown in Figure 2.4(d). The bolus width, w_b , widens over time, t , with an effective axial diffusivity, \mathcal{D}_{eff} , in long circular channels defined as [10]:

$$\mathcal{D}_{eff} = \mathcal{D} \left(1 + \frac{Pe^2}{48} \right) \quad (2.33)$$

$$w_b = 4\sqrt{\ln 2} \sqrt{\mathcal{D}_{eff} t} \quad (2.34)$$

The fundamentals of this phenomenon were first described by Taylor [25]. Given a long enough channel, a pressure driven flow will act on larger timescales than diffusion and a

coupling of the effects occurs called Taylor dispersion [26].

Analytes suspended in a medium can disperse in two ways: through diffusion due to their natural Brownian motion, and through convective forces from the velocity field. Figure 2.5 illustrates these two dispersion modes. To visualize these differences, fluorescent analytes were concentrated at the inlet of a microfluidic chip to form a sample plug.



Figure 2.5 The image show that different flow profiles produce different dispersion effects. (a) Electroosmotic flow of a concentrated fluorescent analyte. (b) Pressure driven flow of a concentrated fluorescent analyte. Source: [27].

In Figure 2.5a the sample plug is driven to the right under electroosmotically driven flow. The average velocity of the plug migrates at the EOF velocity, but the width of the plug increases due to the natural diffusion of the analyte. In Figure 2.5b, the plug is driven to the right under pressure driven flow. The analyte is smeared with the convective flow in the characteristic parabolic profile expected with pressure driven flows. The pressure driven flow can act at shorter timescales than diffusion which yields a sharp edge around the parabolic profile since diffusion has not had enough time to contribute to deviations from the parabolic profile.

2.2 Membrane Technologies

Membranes play an important role in microfluidics. They have applications in chemical and biological engineering. The purpose of membranes can vary and include but are not limited to: filtration, energy conversion, gas separation, and dialysis [28]. This section will focus on filtration membranes and how they can be applied to separating proteins and reducing pressure driven flows for the purpose of separating electrode reservoirs in CE applications.

2.2.1 Membrane Characteristics

2.2.1.1 Bubble Point

The bubble point method is a simple technique used to determine the largest pore size of a membrane [29]. The test begins by filling the pores with the wetting phase, in industrial applications the wetting phase is usually isopropyl alcohol. On one side of the membrane, air is pressurized to a point where the alcohol is removed up to the surface of the membrane in contact with the air. This is better visualised in Figure 2.6.

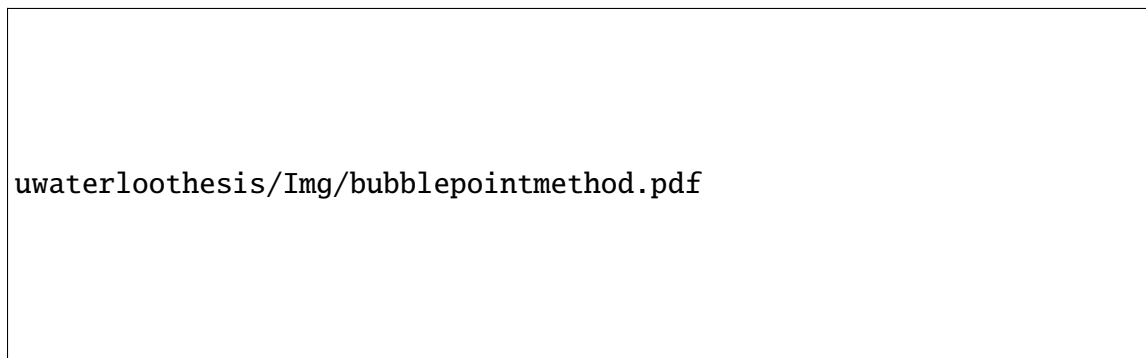


Figure 2.6 Cross sectional view of a membrane during a bubble point test. The non-wetting phase has reached the capillary pressure to allow flow through the largest pore. Bubbles are produced in the wetting phase region.

In order to force air through the pores of the membrane, the pressure must reach a certain value governed by the Washburn equation:

$$D_{pore} = -\frac{4\gamma\cos(\theta)}{\Delta p_c} \quad (2.35)$$

where ΔP_c is the capillary pressure, γ is the interfacial tension between the two phases, θ is the contact angle of the wetting phase, and D_{pore} is the diameter of the pore. During the test, the pressure is incrementally increased up to the point where bubbles are detected. Since pore size and capillary pressure are inversely proportional, the point at which bubbles appear on the opposite side of the membrane indicates the largest pore diameter. Isopropyl alcohol is used because of its low surface tension which means lower pressures can be used [30]. It is also used because it tends to completely wet most surfaces which is described by a contact angle of 0 degrees, eliminating the $\cos(\theta)$ term in the Washburn equation. The bubble point is a common value listed for commercially available membranes.

2.2.1.2 Membranes in CIEF

In capillary isoelectric focusing (CIEF) reservoirs are separated by hollow fiber dialysis tubing which are glued to the ends of the separation column capillaries as shown in Figure 2.7 [31].



Figure 2.7 Schematic of a capillary cartridge developed for CIEF. Source: [31]

This style of cartridge is used in the commercial protein analysis system CE Infinite (Advanced Electrophoresis Solutions Ltd., Cambridge, Ontario). This hollow membrane allows for protons and hydroxide ions to pass freely during CIEF operation. Further information regarding the membrane is unknown as it is considered proprietary.

2.2.2 Polycarbonate Track-Etched Membranes

Polycarbonate track-etched (PCTE) membranes have been used to compartmentalize different channels in microfluidic chips in electrophoretic applications [32]. Polycarbonate membranes manufactured with the ion track etching method produce highly controlled pore sizes and distributions [33]. Suppliers such as Sterlitech and Sigma Aldrich offer a wide variety of pore sizes from 0.01 to 8 μm , for applications in cell biology, fuel testing, bioassays, or water microbiology. The membranes can be hydrophobic or hydrophilic depending on the application and are treated with Polyvinylpyrrolidone (PVP) for low protein binding applications. A full description of these commercially available filters can be found here: <https://www.sterlitech.com/Products/Track-Etched-Membranes.aspx>

[//www.sterlitech.com/hydrophilic-polycarbonate-membrane-filters.html](http://www.sterlitech.com/hydrophilic-polycarbonate-membrane-filters.html).

2.3 Protein Separation Technologies

2.3.1 Protein Characteristics

2.3.1.1 Amino Acids and Proteins

There are 20 amino acids found in the human body and are the building blocks for proteins (polypeptides) as shown in Figure 2.8. Peptides are short chains of amino acids bonded together with peptide bonds. Long chain peptides are called polypeptides. Proteins are formed from two or more polypeptide chains.

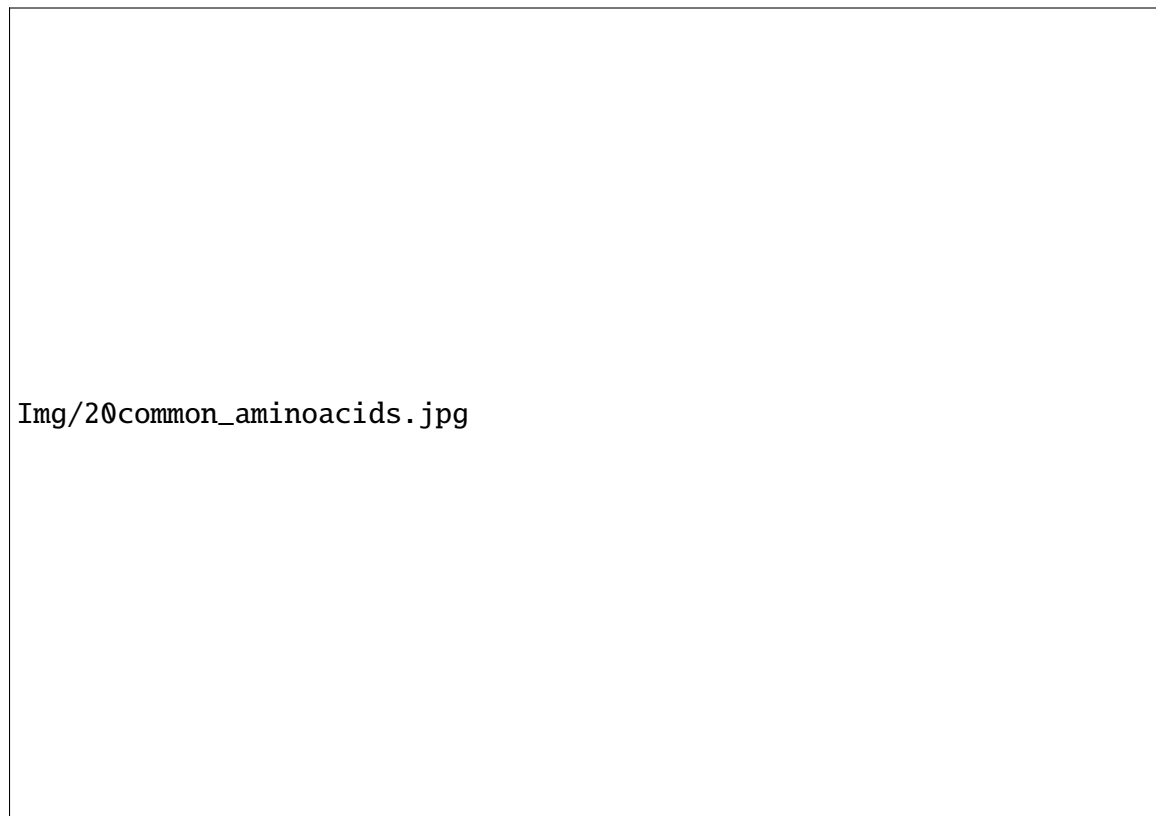


Figure 2.8 A guide to the 20 common amino acids found in the human body. Source: [34].

2.3.1.2 Amino Acid Charge

The charge of an amino acid can be estimated using the Henderson-Hasselbach equation [35]:

$$\begin{cases} z_i^+(pH) = \frac{1}{1 + \frac{K_i}{10^{-pH}}} \\ z_i^-(pH) = \frac{1}{1 + \frac{10^{-pH}}{K_i}} \end{cases} \quad (2.36)$$

where K_i is the acidic dissociation constant of amino acid i , which is also called the K_a [36].

The global charge of the protein is the sum of the positive and negative charge components:

$$z(pH) = \sum_{i \in A^+} \frac{1}{1 + \frac{K_i}{10^{-pH}}} - \sum_{i \in A^-} \frac{1}{1 + \frac{10^{-pH}}{K_i}} \quad (2.37)$$

where $A^- = [Y, C, D, E, C\text{-ter}]$ and $A^+ [K, R, H, N\text{-ter}]$. Y = Tyrosine, C = Cysteine, D = Aspartic Acid, E = Glutamic Acid, K = Lysine, R = Arginine, and H = Histidine.

2.3.1.3 Protein Sequence

Amino acids are represented by a single letter of the alphabet under the FASTA format as shown in Table 2.2.

Table 2.2 Amino Acid Letters in FASTA Format. Source: <https://zhanglab.cmb.med.umich.edu/FASTA/>.

A	alanine	N	asparagine
B	aspartate or asparagine	P	proline
C	cystine	Q	glutamine
D	aspartate	R	arginine
E	glutamate	S	serine
F	phenylalanine	T	threonine
G	glycine	U	selenocysteine
H	histidine	V	valine
I	isoleucine	W	tryptophan
K	lysine	Y	tyrosine
L	leucine	Z	glutamate or glutamine
M	methionine		

2.3.1.4 Isoelectric Point

The net charge of a protein depends on the pH of its environment. A protein can either be positively or negatively charged, but there exists a point of charge equilibrium where the protein is neutral. The origin and history of the isoelectric point is well described by Cohn [37], and attributes the origin of a protein's charge dependence on pH to Hardy [38] who observed the migration direction of a protein was function of whether the fluid was acidic or basic. A comprehensive table of protein pI's was published in 1978 by Malamud [39]. Ahamed *et al.* [40] compiled a list of 17 proteins and their pI points as shown in Table 2.3

Table 2.3 Titration curve parameters. Source: [40]

Proteins	PAN ^a	M ^b (kDa)	Calculated pI	Experimental pI
Amyloglucosidase	P69328	65.8	3.9	3.6
Glucose oxidase	P13006	126.6	4.6	4.2
Trypsin inhibitor	P01070	20.1	4.4	4.6
β -Lactoglobulin A	P02754	18.3	4.6	5.1
Ovalbumin	P01012	42.8	4.9	4.9
BSA	P02769	66.4	5.5	5.5
CA-II	P00921	29.0	6.3	5.9
CA-I	P00915	28.7	6.5	6.6
Penicillin G acylase	P06875	86.2	5.9	6.3
Myoglobin	P68082	17.0	8.1	7.2
Conalbumin	P02789	75.8	6.6	6.6
Lectin	P02870	50.9	5.4	8.2
Trypsinogen	P00760	23.9	9.5	9.3
RNase A	P61823	13.7	9.8	9.4
Cytochrome C	P00004	11.7	10.0	10.0
Aprotinin	P00974	6.5	10.7	10.5
Lysozyme	P00698	14.3	11.0	11.2

^a Primary access number in UniProtKB/Swiss-Prot database (www.expasy.org).

^b Molecular mass of the polypeptide chain.

2.3.1.5 Charge Dependence

Due to the pH dependence of charge on a single amino acid, the overall charge of a protein will also be a function of the pH of its environment. Since proteins are long chains of amino acids, it is too tedious to determine the charge relationship of a protein without the

aid of a computational tool. Prot Pi (www.protpi.ch/Calculator/ProteinTool) is a free-to-use bioinformatic tool that is able to provide insight into the charge dependency of any protein given its FASTA sequence.

As an example, beta-lactoglobulin has the following sequence (source: <https://www.uniprot.org/uniprot/P02754.fasta>):

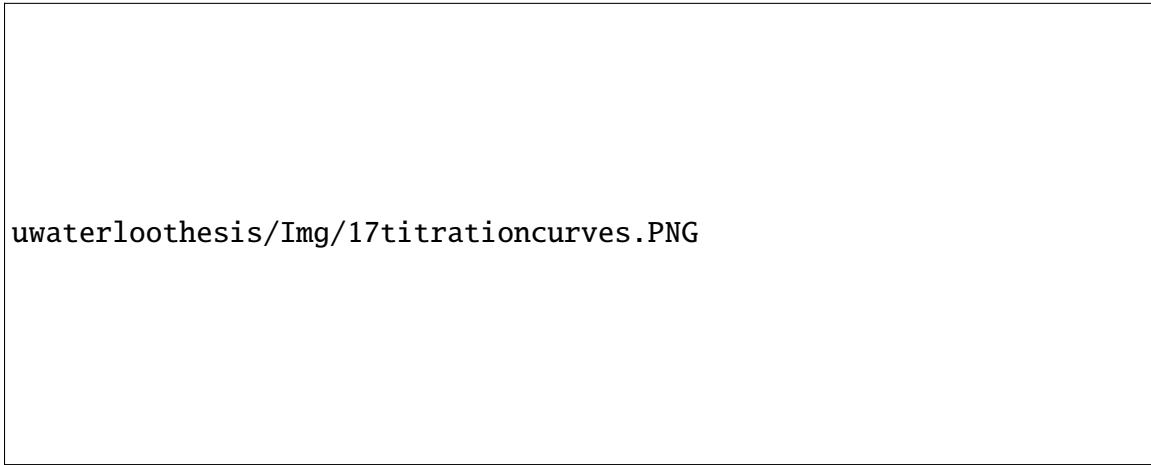
```
MKCLLLALALTCGAQALIVTQTMKGLDIQKVAGTWYSLAMAASDISLLDAQSAPLRVYVE■  
ELKPTPEGDLEILLQKWENGECAQKKIIAEKTKIPAVFKIDALNENKVLVLDTDYKKYLLFC■  
MENSAEPEQSLACQCLVRTPEVDDEALEKFDKALKALPMHIRLSFNPTQLEEQCHI
```

Figure 2.9 shows the charge relationship versus the pH generated by the Prot Pi tool.



Figure 2.9 Titration curve of beta-lactoglobulin generated with the Prot Pi tool.

Ahamed *et al.* [40] plotted the titration curves of 17 model proteins as shown in Figure 2.10.



uwaterloothesis/Img/17titrationcurves.PNG

Figure 2.10 Titration curves of 17 model proteins: (A) Acidic proteins (pH<6); (B) Neutral Proteins (pH 6-8); (C) Basic proteins (pH>8). Source: [40]

The author notes that all of the proteins have a near flat slope in the pH range of approximately 6-9. In this range the overall net charge of the protein does not significantly deviate from zero.

2.3.1.6 Electrophoretic Mobility

With the pH dependence of a protein's charge, the electrophoretic mobility is more accurately described as:

$$\mu_{ep} = \frac{z(pH)e}{6\pi\eta r_s} \quad (2.38)$$

where $z(pH)$ is the charge of a protein as a function of the pH of its environment.

2.3.1.7 Diffusion Coefficient

If the hydrodynamic radius of the protein is known, the Nernst-Einstein relation can be used to find the diffusion coefficient. Interestingly, not only are proteins approximately spherical and hard, they all have approximately the same specific volume of 0.73 cm³/g (or equivalently a density of 1.35g/cm) for molecular weights above 20kDa [41–43]. Therefore, the diffusion coefficient can be found using only the molecular weight of the protein. Wolfe

used the following equation to estimate the diffusion coefficient of a protein under the assumption of constant specific volume:

$$D = 8.34 \times 10^{-8} \frac{T}{\eta M^{1/3}} \quad (2.39)$$

where T is the temperature, η is the dynamic viscosity of the fluid, and M is the molecular weight. For proteins with lower molecular weights, Fischer [43] fitted the following equation to experimental data:

$$\rho(M) = \left[1.410(6) + 0.145(28) \times \exp\left(-\frac{M(kDa)}{13(4)}\right) \right] g/mL \quad (2.40)$$

The numbers in parenthesis in the equation represent the standard uncertainty of that value.

Bovine albumin with a molecular weight of 67kDa, has a diffusion coefficient of $5.9 \times 10^{-11} \text{ m}^2/\text{s}$ [41]. A list of diffusion coefficients of common proteins in water was published by Nauman *et al.* [44].

2.3.2 IEF, CIEF

Isoelectric focusing (IEF) separates analytes based on their different pI points. Carrier ampholytes are required to generate a linear pH gradient so that each analyte can migrate to its pI point in the presence of a constant electric field. As the proteins migrate to their respective pI points, they form concentrated bands. Righetti [45] describes carrier ampholytes as "*a compound capable of 'carrying' the current (a good conducting species) and capable of 'carrying' the pH (a good buffering species).*" In the presence of an electric field, the carrier ampholytes arrange themselves in a manner to create the linear pH environment the analytes of interest respond to. Capillary isoelectric focusing (CIEF) refers to IEF carried out in a capillary. The CE Infinite CIEF system is used in this thesis to obtain the pI points of analytes and validate the novel method of separating proteins. The composition of carrier ampholytes used with this system is proprietary information.

IEF is a very powerful technique due to its high resolving power and speed at which

separations can be performed [18]. The resolution of IEF, $\Delta(pI)$, for each species can be described as [45]:

$$\Delta(pI) = 3 \sqrt{\frac{\mathcal{D}[d(pH)/dx]}{E[-du_{ep}/d(pH)]}} \quad (2.41)$$

The factor of 3 comes from the 3σ of a Gaussian distribution whereby 99.7 % of the species is within this pI difference. This can be visualized as the width of the band of a specific protein. A small $\Delta(pI)$ is desired and is achieved with a high electric field, low diffusion coefficient and mobility slope for the analyte, and a lower step size in the pH gradient.

2.3.2.1 Collection Methods

The CE Infinite system uses the capillary cartridge design shown in Figure 2.7. In order to collect the separated protein bands, the proteins are eluted from the capillary by hydrodynamic flow and collected into vials controlled by an auto-sampler. Since the bands migrate at the same average bulk flow velocity, their initial spacing will dictate when each band will reach the outlet of the capillary. If two adjacent proteins are too close together, they may end up overlapping due to Taylor dispersion and a high capillary length ratio as described in Section 2.1.3.1. To overcome this problem, the CE Infinite uses a transfer capillary with a smaller ID than the separation capillary as shown in Figure 2.11. This increases the spacing between adjacent analytes.

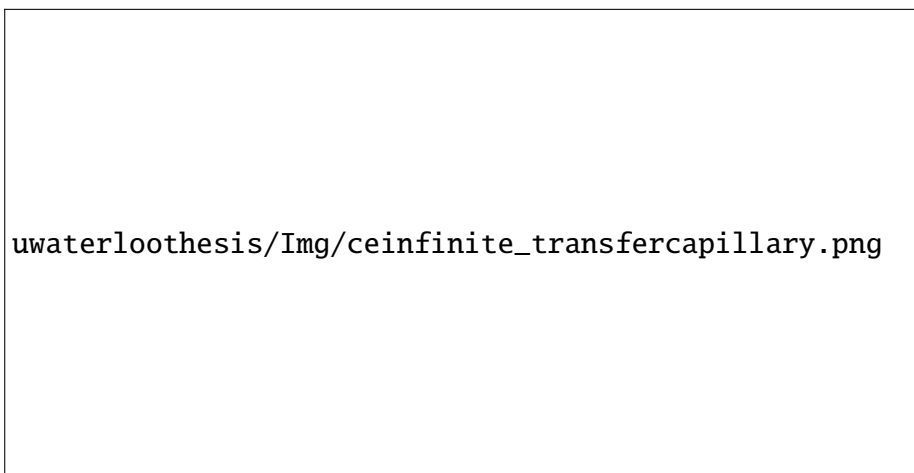


Figure 2.11 Illustration of the separation and transfer capillaries used in the CE Infinite capillary cartridge. From top to bottom are increased instances in time. The small diameter transfer capillary is used to quickly elute separated analytes in order to reduce the effects of Taylor dispersion. Source: [46].

Another inherent problem with CIEF is the low volume of each protein that can be collected. During CIEF operation, the sample inside the separation capillary only migrates due to the applied electric field. Therefore, the molar amount of protein that can be concentrated is dependent on the molar amount already within the volume of the separation capillary. This in turn leads to μg scale amounts of protein that can be collected during each run of the system, making this method less suitable for large scale (mg) collection of proteins.

2.3.3 GEMBE

Gradient Elution Moving Boundary Electrophoresis is a relatively new method for separating chemical species based on their electrophoretic mobility [47]. Two reservoirs are connected via a separation capillary. One reservoir contains the mixture of chemical analytes. The analytes are electrophoretically driven towards the capillary against a varying bulk flow driven by a pressure system. Species with a high mobility can overcome the hydrodynamic drag and enter the capillary. The bulk flow is slowly reduced which allows sequentially lower mobility analytes to pass through the capillary into the other reservoir [48]. Fig-

Figure 2.12 illustrates how a sample initially cannot enter the separation capillary because the electrophoretic force is overcome by the hydrodynamic drag induced by the bulk flow of the run buffer. As the bulk flow is lowered, the electrophoretic force can overcome the hydrodynamic drag force and enter the separation capillary.

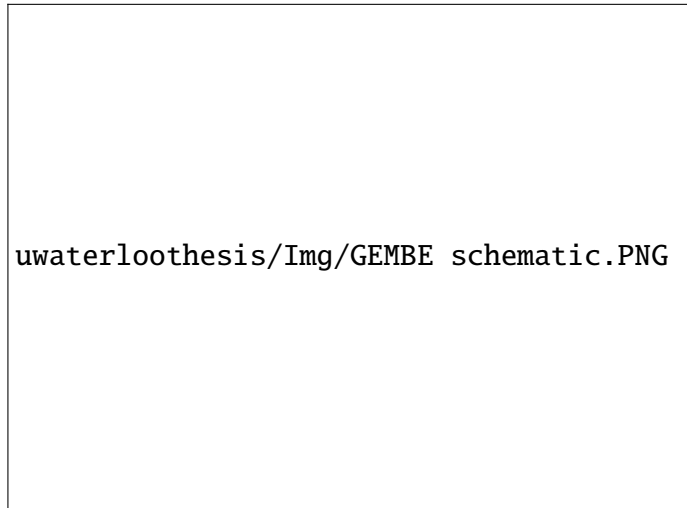


Figure 2.12 Illustration of the principle used in GEMBE. (A) shows the net force acting on the sample is dominated by the bulk flow of the run buffer. (B) shows a lowered bulk flow, which allows the sample to be electrophoretically driven into the capillary. Source: [48].

Ross [48] further developed GEMBE to include channel current detection, whereby the short separation channel also behaves as a conductivity cell. Ross notes that "*because the channel is so short, only a single moving boundary 'step' is present in the channel at any given time, and the measured current through the channel can therefore be used to give a signal comparable to what is normally generated by more complicated detector arrangements.*" Plotting the current as a function of time allowed for the detection of the analytes in the form of steps. Ross also plotted the current derivative as a function of time which produced a more familiar electropherogram as shown in Figure 2.13(B).

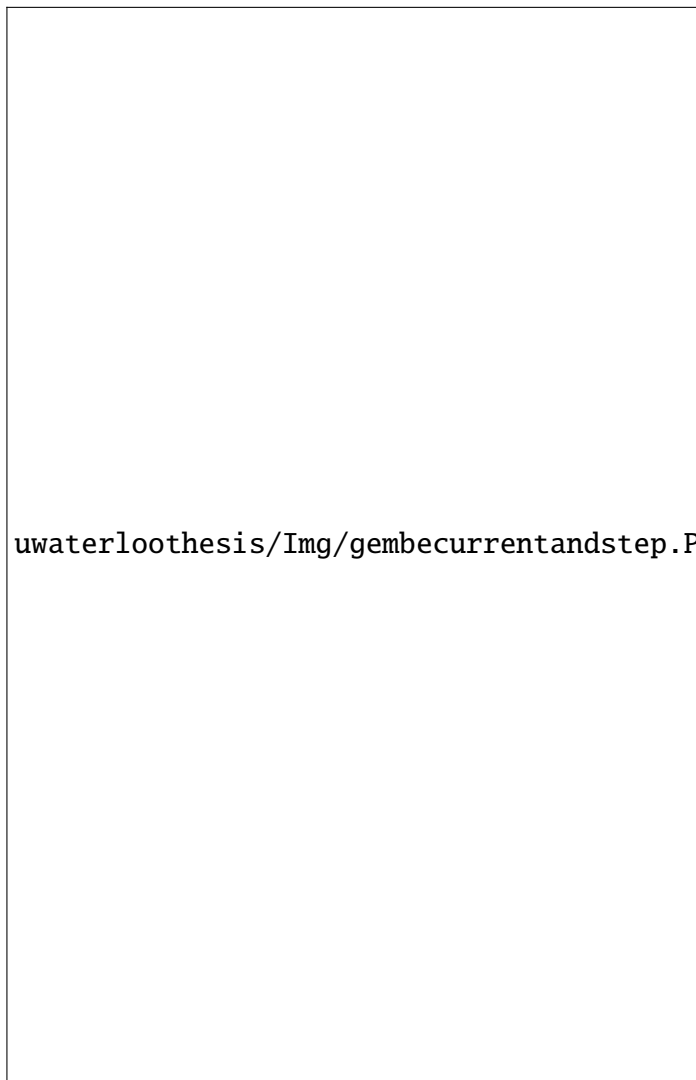


Figure 2.13 (A) plot of current versus time for seven analytes. (B) current derivative versus time which produces a more familiar electropherogram as seen in CZE. Source: [48].

2.3.4 Continuous Free-Boundary Flow-Electrophoresis

Continuous free-boundary flow-electrophoresis is a preparative electrophoretic separation technique which separates charged proteins from neutral proteins [49]. A cell is constructed using two semi-permeable parallel membranes which separate the sample fluid from the electrodes as shown in Figure 2.14. A shorter membrane is placed in the center to act as a baffle, dividing the cell into three distinct regions and fluid paths. For a mixture of two proteins, the pH of the buffer is prepared so that it matches the isoelectric point one of

the proteins. Therefore, the sample contains an electrophoretically mobile and immobile protein. The sample is pumped into the cell through the inlet. An electric field is generated perpendicular to the fluid flow, causing the mobile protein to migrate towards the outer cell wall. The fluid then bifurcates with the immobile protein flowing around the dividing membrane to the top outlet, Y. The mobile protein, which was forced near the membrane wall, A, follows streamlines towards the outlet, Z.



Figure 2.14 Schematic of continuous free-boundary flow-electrophoresis apparatus. A, A' are the outer membranes separating the electrodes; B is the baffle membrane; X is the sample inlet; Y is the outlet for collecting immobile proteins; Z is the outlet for collecting mobile proteins. Adapted from: [49].

This apparatus can purify the immobile protein but reduces the initial concentration by at least 20 percent. The mobile protein extracted at the lower outlet still contains the remaining immobile protein since it homogeneously fills the inlet and can follow the same streamlines as the mobile protein. The method is capable of high flow rates of up to 4 mL/min using constant current of 2 Amperes. This process, however, requires a secondary process to increase the concentration of the purified sample.

2.3.5 Ion-Exchange Chromatography

Ion-exchange chromatography (IEC) is a method for separating charged analytes based on their electrostatic interactions with a charged stationary phase. An IEC column is filled with an insoluble charged matrix which is the stationary phase, such as polymer beads. Analytes are pumped into the IEC column, and analytes with opposite charges to the stationary phase will bind together. Analytes with the same charge will flow through the column. The analytes will elute over time as a function of their net charge [50].

2.3.6 pH Gradient Ion-Exchange Chromatography

A similar method to the one developed in this thesis, called pH Gradient Ion-Exchange Chromatography, was applied as an analytical tool for separating proteins in 2007 by Ahmed *et al.* [40]. Figure 2.10 shows the titration curves they modeled using the bioinformatics tool ExPASy. This method was reported to separate proteins with a difference in pI point as small as 0.1. Through their analysis of the titration curves of acidic, neutral and basic proteins, the author concluded that the method is only appropriate for separating acidic or basic proteins. This is because the neutral proteins have an electrophoretic mobility close to zero and will elute at pH values much greater than their pI points.

2.3.7 CZE

Capillary zone electrophoresis (CZE) is a basic CE method used to separate analytes based on the difference between electrophoretic mobilities as described by Equation 2.18 [18]. This is accomplished by using a homogeneous buffer solution and a constant electric field. A sample mixture which has been injected into the separation region of the capillary, begins to separate over the length of the capillary with higher mobility analytes leading and lower mobility analytes trailing. Jorgenson [51] was the first to apply zone electrophoresis to a glass capillary [52]. The separation efficiency of CZE is described by the number of theoretical plates, N , defined as:

$$N_{plates} = \frac{\mu_{ep}V}{2D} \quad (2.42)$$

where V is the applied voltage over the length of the capillary. Since N_{plates} is proportional to V , high voltages (>30kV) are typically used to achieve the high separation efficiencies. However, since high voltages give rise to larger power dissipation, small internal diameter (75 μm) capillaries of length >80 cm are used to ensure adequate heat dissipation [51].

2.4 Buffers

Buffers play an integral role in CE. Factors which should be considered when selecting an appropriate buffer include type, useful pH range, ionic strength, concentration, temperature dependency, conductivity, and minimum useful absorbance wavelength if UV detectors are being used. For a more detailed guide on selecting an appropriate buffer, Landers, Section 1.3.3.5 [18] provides an excellent starting point.

2.4.1 Ionic Strength

The concept of ionic strength was first introduced by Lewis and Randall in 1921 [53]. The ionic strength of any ionic solution is given by:

$$I = \frac{1}{2} \sum_1^n c_i z_i^2 \quad (2.43)$$

It is not within the scope of this review to go into more depth on ionic strength. A more detailed description on ionic strength and how it plays a role in electrophoresis is covered by Sastre de Vincente [54].

2.4.2 Types of Buffers

The choice of buffer in CE applications is a crucial step to achieving successful separations. Buffers should be chosen such that they do not interfere with detection of the analytes,

have enough buffering capacity to maintain the desired pH, has a low conductivity to avoid Joule heating effects, and sustains solubility of the analytes [18, 55]. Table 2.4 shows a list of common buffers used in CE applications and their useful pH ranges which has enough buffering capacity to resist changes in pH with an increase in proton or hydroxide ion concentrations.

Table 2.4 Commonly Used CE Buffers. Source: [18]

Buffer	Useful pH Range	Minimum Useful Wavelength (nm)
Phosphate	1.14 - 3.14	195
Formate	2.75 - 4.75	200
Acetate	3.76 - 5.76	200
Citrate	3.77 - 4.77	200
MES*	5.15 - 7.15	230
Citrate	5.40 - 7.40	200
PIPES	5.80 - 7.80	215
Phosphate	6.20 - 8.20	195
HEPES*	6.55 - 8.55	230
Tricine*	7.15 - 9.15	230
Tris	7.30 - 9.30	220
Borate	8.14 - 10.14	180
CAPS*	9.70 - 11.10	220
Phytic	1.9 - 9.5	200

* Zwitterionic buffers

2.5 Design Methods

The linear Stokes equations allows for many analytical solutions of different fluid phenomenon to be found, whereas would be near impossible in the case of turbulent flows which rely on statistics to find approximate solutions. However, coupling the Stokes equations with other physics such as electrokinetic, or chemical interactions complicates the matter to the point where numerical methods are necessary to model the interactions. Microfluidic flows and transport simulation for electrokinetic applications are detailed in the text by Erickson [56] as well as by Zhao [57].

2.5.1 Numerical Simulations (COMSOL)

The commercial numerical simulation software COMSOL Multiphysics is used to validate and predict fluid phenomena throughout this study. COMSOL was chosen for its user friendly graphical-user-interface and extensive library of tutorials. Although it is possible to control COMSOL through custom code written in MATLAB to gain more control over all aspects of the simulation, it is a more time intensive task which may not be necessary depending on the goal of the simulation. Although microfluidics is concerned with the behaviour of phenomena at the micron scale, the reality is that there is a wide range of length scales which must be considered since devices are manufactured at a macroscale. To simulate the entire domain of a microfluidic device would be too computationally expensive and impractical, so only regions of interest are typically simulated. Ermakov [58] and Dutta [59] provide details on creating numerical simulations involving electrokinetic transport of chemical species in microfluidic applications. Full details on numerical simulations used in this thesis is described in Chapter 4.

Chapter 3

Experimental Methods

This chapter provides details on experimental methods, chemicals, and equipment used throughout this thesis. This chapter also includes information on constructing custom adapters used to connect glass capillaries of any size directly to polymer tubing.

3.1 pH Measurement

Accurate and precise measurement of buffer pH is vital in the development of a pH-based separation mechanism. The Orion™ 5 star benchtop pH meter shown in Figure 3.1 is capable of measuring pH to a precision of ± 0.001 . Thermo Orion™ 911600 semi micro low maintenance gel pH electrode has a limiting tolerance of ± 0.1 pH units. During measurements, the meter displayed pH measurements to three significant digits. The manual for the the pH meter can be found here: <https://www.manualslib.com/manual/1275093/Thermo-Scientific-Orion-Star.html>. Details on the pH electrode can be found here: <https://assets.thermofisher.com/TFS-Assets/LSG/manuals/D15848~.pdf>.

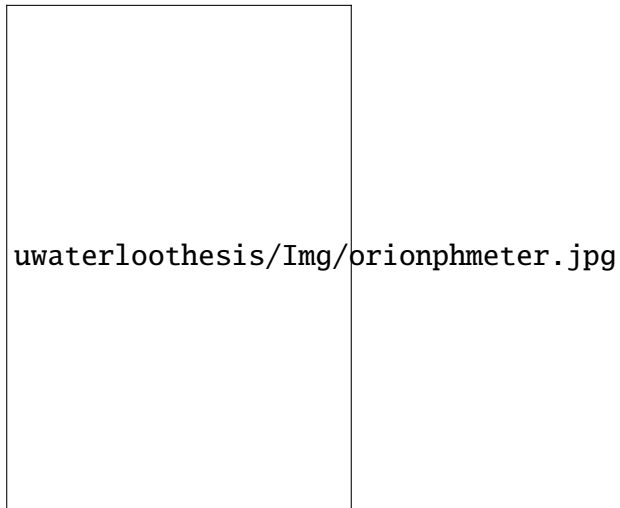


Figure 3.1 Orion 5 star benchtop pH meter used to measure buffer pH.

3.2 Reference Buffers

To ensure accurate measurements of pH, reference buffers were used to calibrate the pH meter and electrode. Reference buffers of pH 7.000 and 10.012 ± 0.010 at 25°C were purchased from VWR Canada.

3.3 Sample Buffers

Tris buffers were prepared using a tris base (Sigma-Aldrich Canada Co., Ontario) and titrated to the desired pH value using 0.1 M Sulfuric acid (Sigma-Aldrich Canada Co., Ontario). Once the right pH was attained, the deionized (DI) water was added to achieve the desired concentration. Sodium Acetate buffer solution with concentration of 3 M and $\text{pH } 5.2 \pm 0.1$ (Sigma-Aldrich Canada Co., Ontario) was diluted with DI water to reduce the concentration to 50 mM. This was used in reservoir buffer containing the cathode (outlet).

3.4 Pressure Pump

The pressure pump (Fluigent MFCS-8C) is an eight-channel gas driven system capable of supplying pressures up to 2 bar. The pressure pump connects to a reservoir holder (Fluwell-4C) which holds up to four reservoirs for individually controlled pumping. The pressure pump has a faster response time and negligible oscillations as compared with syringe pumps. The main drawback of using a pressure pump over a syringe pump is the flow rate is a function of the hydrodynamic resistances of the microfluidic network, which must be characterized before the flow rates can be determined. This is done by using an external flow meter to measure the flow rate and a corresponding pressure versus flow rate relationship can be established.

3.5 Syringe Pump

A Harvard Apparatus Pump 11 PicoPlus syringe pump can accept up to two syringes which are actuated simultaneously by a single pusher block. The pump can operate in two modes: infuse and withdraw. The minimum and maximum flow rates are thereby determined by the internal diameter of the syringe being used in combination with the travel rate of the pusher block. The syringe pump automatically calculates the correct travel rate from the requested flow rate and diameter set by the user. The pusher block minimum and maximum travel rates are 0.0388 $\mu\text{m}/\text{min}$ and 0.8333 mm/min respectively. The travel rates are average velocities and do not represent the instantaneous velocity of the pusher block due to the cyclic nature of the stepper motor. The pusher block is advanced by a stepper motor with an advance per step of 0.0444 μm per step. To minimize the influence of the cyclic nature inherent with any syringe pump using a stepper motor, the pump should operate near the upper end of its travel rates [60].

To facilitate additional syringes, a custom syringe mount and pusher block adapter were created by 3D printing. The mount allows up to five syringes to be mounted instead of only two. The pusher block adapter has a recess feature to mate with the syringe plunger.

3.6 Syringes

Gas-tight syringes (1710 CX SYR) made from borosilicate glass from Hamilton Company provide precise volume dispensing and interface with most syringe pumps. The 1/4-28 threaded end connects to an appropriate fluid adapter for tubing or capillaries. This series of syringes have a nominal dead volume due to the threaded end and needs to be accounted for when calculating sample concentrations. The dead volume also means when drawing liquids, an air bubble is formed between the plunger tip and the liquid. If the bubble is not removed when using the syringe with a syringe pump, the bubble will act as a damper and drastically slow the response time. A simple trick to remove the bubble is to draw water to the maximum volume, and quickly push the plunger down to the end. This will force the water around the bubble and displace it from the plunger tip. This is repeated until the bubble is completely removed and the water fills the dead volume space.

3.7 Connectors

The number of connectors to interface between syringes, capillaries, and tubing are vast and can be challenging finding the best connector suitable for the task. Vendors such as VICI, Hamilton, and IDEX have large catalogues and guides for selecting the right connector. However, with respect to capillaries which come in many different outside diameters, capillary connectors are only manufactured for 360 μm diameter capillaries. In order to interface between smaller capillaries, a simple method for manufacturing an adapter was developed. Connectors between polymer tubing and syringes are relatively easy to source, therefore, the following procedure will be concerned with connecting a capillary directly to the polymer tubing. To manufacture an adapter for a 150 μm capillary to connect with a syringe, polymer tubing with an inside diameter of 254 μm (0.010") was used as the connector because it is the smallest internal diameter that can be sourced. The tubing is cut to 10 cm length and is gripped securely on one end with a vice. A capillary with a diameter smaller than the connecting capillary (in this case 100 μm) is used as a mandrel and

inserted into the tubing. A heating element such as a soldering iron is positioned under the tubing. Once sufficiently heated, the free end of the tubing is slowly pulled with pliers while ensuring the iron remains under the tubing at the same material position. As the tubing is elongated, the softened zone of the tubing will begin to collapse around the mandrel. While maintaining constant tension, the iron is removed, and the tubing is permitted to cool into its final shape. The mandrel is then removed by hand. If the applied tension is too high, the mandrel will be difficult to remove without breaking. The vice and pliers will create tooth marks on the surface of the tubing, so it is trimmed on both ends to the desired length. The fabrication process is illustrated in Figure 3.2.

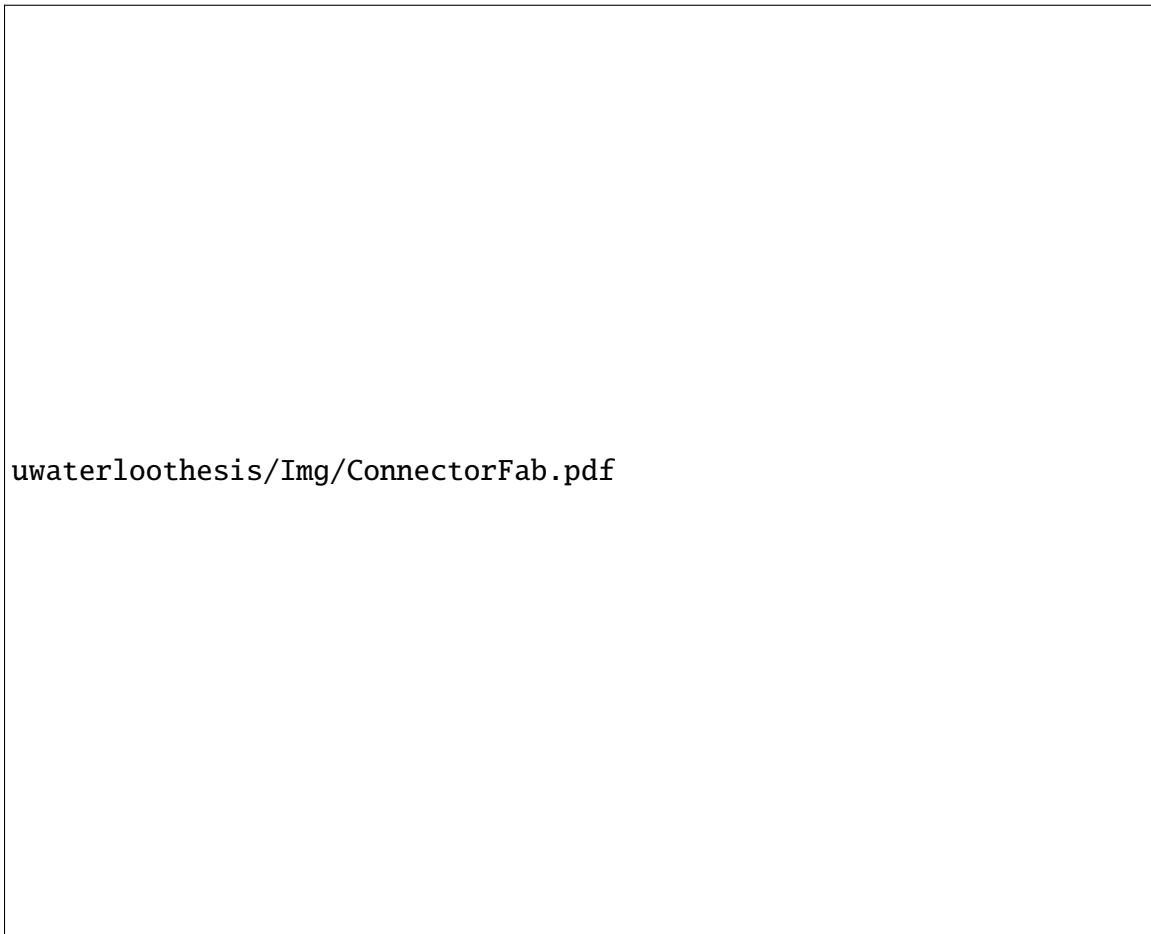


Figure 3.2 Cross-sectional view of custom capillary adapter manufacturing process.

Figure 3.3 shows a capillary inserted into the adapter. A proper seal has been achieved

when the end of the capillary appears larger and darker as shown in the magnified window.

Img/capillaryconnectorseal.png

Figure 3.3 Custom polymer tubing capillary adapter.

Typical equipment used in performing separations are shown in Figure 3.4.

uwaterloothesis/Img/syringeequipmentandsolutions.png

Figure 3.4 This image shows the typical chemicals and syringe assembly used to perform separations. The lower image shows the disassembled syringe adapters and fittings. The fully assembled syringe is loaded into the syringe pump and the capillary cartridge is connected to the capillary adapter tubing.

3.8 High Voltage Power Supply

To generate high voltages, the LabSmith HV power sequencer (HVS448 3000V) was used. The system provides eight independently controlled channels which can be used as current or voltage sources, or just a voltage monitor. All experiments contained within this

thesis used the HV sequencer as a voltage source. The sequencer is controlled using LabSmith's Sequence software which can monitor and record the voltage and current during an experiment.

A more compact and lower output power supply by LabSmith is the uEP01-300 Power Module. It is a single channel capable of supplying up to 300 V, or 0.25 A in constant current mode. LabSmith's uProcess Automation Interface EIB200 is required to control the power module as well as their uProcess Automation software for controlling their uProcess line of devices.

3.9 Cheminert Selector and Microelectric Actuator

To manipulate fluid paths, a Cheminert, five-position, low pressure selector (H-C25F-3185D) from VICI can direct a supply line of fluid to one of five outputs. This model is a flow-through option means the non-selected lines flow to individual outlets.

The microelectric actuator (EMH) from VICI is used to automate the path selection process of the selector. The actuator comes with an actuator control module and manual controller. The manual controller has an eight-segment display to indicate the current position or path, and two buttons to step the actuator and adjust the selector to the next or previous path. To further automate the actuator, a serial cable is connected to the control module. The selector is initially set up for RS-232 serial communication.

3.10 Capillary Cartridge

The capillary cartridge provided by AES was chosen because of its robust and proven design. Another major reason for choosing this capillary cartridge is that EOF is suppressed. The capillary cartridge was designed for use in isoelectric focusing applications, which requires EOF to be suppressed, and is accomplished by a proprietary coating that is applied to the inner diameter of the separation capillary.

A detailed schematic of the capillary is shown in Figure 3.5. Equation 4.3 shows the bulk flow velocity is inversely proportional to the inside diameter of the capillary squared. Consequently, it is advantageous to use a large inside diameter separation capillary for a given flow rate, in order to increase the effectiveness of the electrophoretic velocity, acting to *hold* analytes at the inlet. Therefore, 320 μm was selected, which was the largest separation capillary available.



Figure 3.5 (Top) Image of the capillary cartridge used in all experiments. (Bottom) Schematic of the capillary configuration. The three capillaries are joined together with a hollow fiber membrane, which allows current to flow from the buffer solution reservoirs into the separation capillary.

3.11 Fluorescent Markers

In order to visualize the separation, fluorescent IEF markers (Sigma-Aldrich Canada Co., Ontario) were used in place of proteins. The IEF markers are short chain amino acids which still exhibit zwitterionic properties and have a known pI point. IEF markers are traditionally used with UV-based imaging systems, therefore, tend to have emission wavelengths that are lower than what fluorescence imaging systems are designed for. The fluorescence system

used set the lower bound for emission wavelengths at 330 nm. Table 3.1 shows the properties of the IEF markers used in experiments.

Table 3.1 IEF Marker Properties

pI	λ_{ex} (nm)	λ_{em} (nm)	mg/mL	Stock Solution	Molecular Weight (g/mol)
5.2	336	424	1	5mM HCl	285.30
7.6	385	495	1	10mM HCl	No Data
8.1	340	420	3	H ₂ O	No Data
9.0	385	495	1	10mM HCl	370.49

3.12 Fluorescent Microscopy

Imaging fluorescent markers was performed with an Olympus GX-71 inverted microscope equipped with a 100W mercury lamp system. The emission spectrum of the mercury burner was taken from the user manual of the Olympus GX-71 and is shown in Figure 3.6.

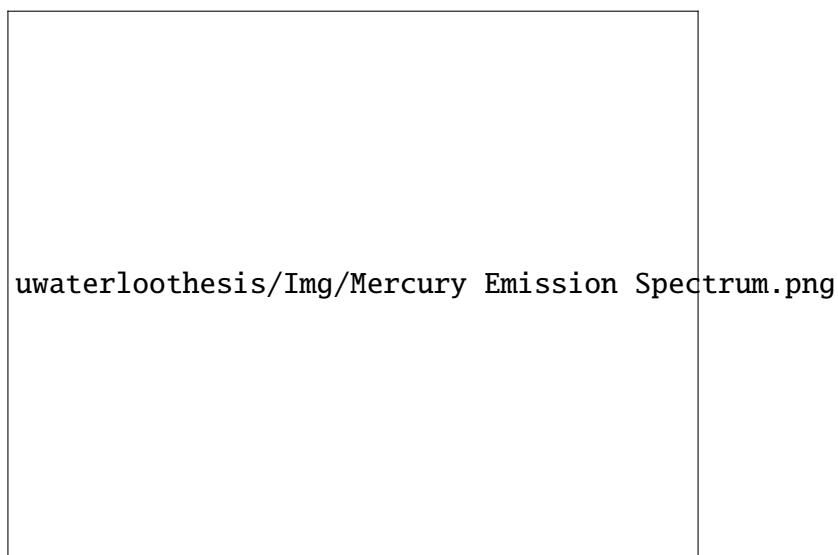
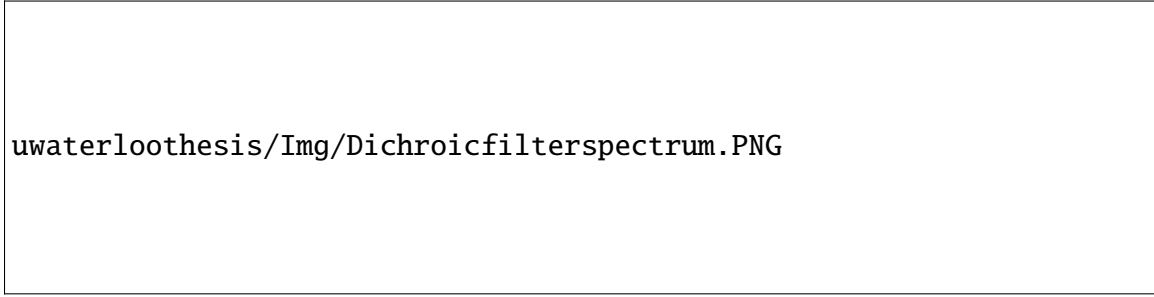


Figure 3.6 Emission spectrum of an ultra-high-vacuum Mercury Burner used in the GX-71 inverted microscope for fluorescence imaging.

When choosing IEF markers, it is important that their excitation wavelength falls within a peak of emission wavelengths from the mercury burner so that there is enough energy

available for the fluorescent sample to be able to emit light. To effectively see the fluorescent markers, a dichroic mirror, or UV excitation cube (U-MWU2) with an excitation range of 330-385 nm and an emission limit of 420 nm.



uwaterloothesis/Img/Dichroicfilterspectrum.PNG

Figure 3.7 Dichroic filter spectrum of the Olympus U-MWU2 dichroic filter cube. The left peak in blue is the excitation filter; the right signal in yellow is the emission filter. Source: <http://webtools.olympus.eu/micro/fluorophore/en-GB/Cube/Detail/34>.

The excitation filter only allows light from the mercury burner to pass through to the sample in that range. The light that is emitted from the sample below the 420 nm wavelength is removed, and anything above is passed to the camera. Images were captured on a Q-imaging Retiga Exi which interfaces directly with the GX-71 microscope. The software used to capture images is μ Manager 2.0-gamma, an open source microscopy program.

Chapter 4

Capillary Electrophoresis pHGEMBE

Separation Technique Development

This chapter describes the development process of a novel electrophoretically driven protein separation method. The mechanism is described mathematically and illustrated through diagrams and numerical simulations. The method is termed *pH Gradient Elution Moving Boundary Electrophoresis* or pHGEMBE.

4.1 Fundamental Equations

The initial goal of experiments was to separate two analytes with a large difference in pI. For simplicity, the charge slope of the analytes is assumed to be linear near their respective isoelectric points. The pH of the buffer solution is chosen to match the higher pI of the two analytes so that it has a net neutral charge, and therefore, the lower pI analyte will have a net negative charge. This principle is shown in Figure 4.1.

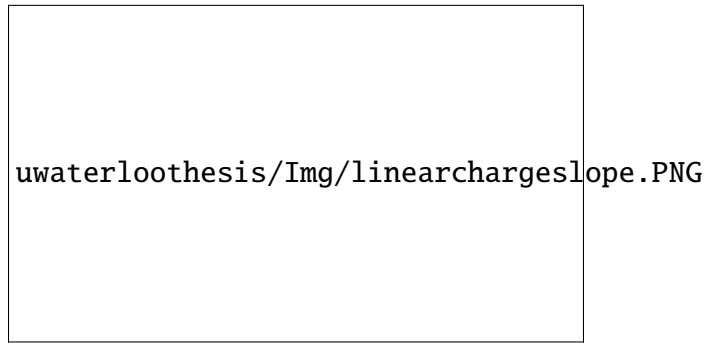


Figure 4.1 Charge relationship of a zwitterion near its pI point.

In the presence of an electric field and pressure driven flow, analytes will migrate according to the vector equation:

$$\mathbf{u}_{net} = \mathbf{u}_b + \mathbf{u}_{ep} \quad (4.1)$$

where \mathbf{u}_b is the average bulk fluid velocity. All experiments were carried out using syringe pumps operating at a constant flow rate. The average bulk fluid velocity can be determined by:

$$u_b = \frac{Q}{A_{cs}} \quad (4.2)$$

where Q is the flow rate, and A_{cs} is the cross sectional area of the circular capillary. The net velocity of the analyte can then be written as:

$$u_{net} = \frac{4Q}{\pi D^2} + \mu_{ep} E_z \quad (4.3)$$

4.1.1 Mechanism Analysis

To test the separation mechanism, fluorescently labelled IEF markers listed in Table 3.1 were chosen for their well defined pI points and ability to visualize their response to the change in pH and electric field by fluorescent microscopy. Sigma-Aldrich does not provide the charge slope information of the marker, but cite the works of Horka *et al.* [61] which does provide

the charge slope of each marker they used at their respective pI points. The supplier cited providing the markers was Fluka Production GmbH, which was later acquired by Sigma-Aldrich. Therefore, it is assumed that the markers are the same and that the markers are peptides. The electrophoretic mobility of the IEF markers is not provided by the supplier, therefore it must be approximated using the molecular weight and assuming the density of the marker. Fischer [43] provides a plot of an experimentally fit curve for proteins less than 10 kDa with a density of 1420 kg/m^3 .

The radius of the peptide can be calculated by:

$$m = M_w (\text{kg/mol}) (6.022 \times 10^{-23} (\text{mol}))$$

$$r_s = \left(\frac{3m}{4\pi\rho_{peptide}} \right)^{1/3} \quad (4.4)$$

Using Equation 2.38, substituting the above value for the radius, and replacing the charge function with a linear function, the mobility can be approximated as:

$$\mu_{ep} = \left(-\frac{d(z)}{d(pH)} pH + z_0 \right) \frac{e}{6\pi\eta} \left(\frac{4\pi\rho_{peptide}}{3m} \right)^{1/3} \quad (4.5)$$

Using an approximate molecular weight of 0.5 kg/mol yields a radius of 0.5 nm. Values used to generate the velocity plot shown in Figure 4.2 are listed in Table 4.1. The velocity plot shows that when the buffer solution has a pH of 8.1, the pI 8.1 marker will be electrically neutral and elute at the bulk flow rate velocity. The pI 5.2 marker has a net negative charge and its velocity is in the opposite direction of the bulk flow velocity.

Table 4.1 Parameters used to generate the velocity plot to compare two fluorescent markers.

Parameter	Value	Unit
Capillary ID, D	320	μm
Flow Rate, Q	400	nL/min
Bulk Velocity, u_b	0.5	cm/min
Electric Field, E_z	20	kV/m
Analyte Radius, r_s	0.5	nm
Buffer viscosity, η	0.001	Pa · s
$dz/d(\text{pH})_{5.2}$	-0.27	
$dz/d(\text{pH})_{8.1}$	-0.23	



Figure 4.2 Velocity plot versus pH of two IEF Markers. The red line represents the behaviour of the marker with a pI of 8.1. When the buffer pH is at 8.1, the pI 8.1 marker will elute with the bulk flow. The blue line represents a pI 5.2 marker, which will be negatively charged at a pH of 8.1 and will move with an opposing velocity to the bulk velocity. The dashed line represents the constant average bulk flow velocity.

4.1.2 Peptide and Protein Mobilities

The electrophoretic mobilities of peptides in reality is not linear over of the large pH range shown in Figure 4.2. The movement of the peptides is essentially governed by two competing forces, the hydrodynamic drag and the electrophoretic force. These forces are determined by the applied volumetric flow rate and the electric field respectively. It only serves as a rough approximation for determining the magnitude of the flow rates and electric fields to achieve separation. Figure 4.3 shows how the mobilities of various peptides change with respect to pH. The Prot Pi tool was used to generate the charge versus pH data sets for each peptide as well as the molecular weight. Equation 2.38 and Equation 4.4 were used to map the electrophoretic mobilities as a function of pH.

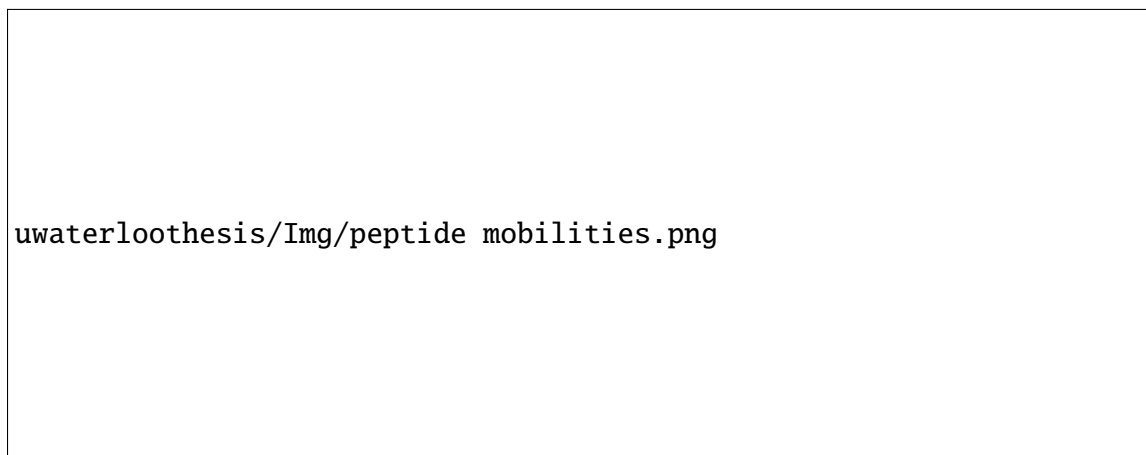


Figure 4.3 Peptides with pI points between 3 and 11 are shown. (left) titration curves generated using the Pi Prot tool and ExPASy data set. (right) normalized mobilities plotted against pH.

The peptides have been divided into basic, neutral, and acidic categories outlined in Figure 2.10. However, the peptides in the neutral range (pH 6-9) do not suffer from the flat slope seen by proteins, maintaining a relatively steep slope around their pI points. Figure 4.4 was generated using the same procedure for the peptides. Each protein represents an acid, neutral, and basic protein.



Figure 4.4 (left) Electrophoretic mobilities of bovine serum albumin (BSA), myoglobin (Mb) and cytochrome C (CYTC) as a function of pH. Charge values were calculated the Prot Pi tool and used to generate the electrophoretic mobilities. (right) electrophoretic mobilities normalized with respect to their maximum at pH = 0.

4.1.3 Fundamental Concepts

The process of concentrating and separating proteins is iterative. Figure 4.5 illustrates the process for two charged proteins (big red and small purple circles) in an initial sample mixture, but the process can be expanded to higher numbers of proteins. With a constant flow rate generated by a syringe pump, a constant average bulk velocity u_b is maintained.



Figure 4.5 Illustration of elution steps in a capillary with positive and negative membranes shown in blue. The view is a cross-section and is radially symmetric, including the membranes. (a) Low concentration proteins with a net negative charge enter the separation capillary via pressure driven flow. The large red proteins have a higher pI than the smaller purple proteins. The solid edge around each protein represents a net charge. The net negative charge of all proteins is a result of the sample buffer solution having a higher pH than the pI of the proteins. (b) All proteins begin to stick to the positively charged membrane. Proteins are unable to pass further into the capillary as they experience an electrophoretic force greater than the hydrodynamic drag force. (c) Once the proteins reach the desired concentration, a pure sample buffer is flushed through the system to concentrate any remaining upstream proteins. (d) The solution buffer pH is lowered to match the pI of the red protein. The loss of the solid edge represents a neutrally charged protein at its isoelectric point. The protein elutes at a higher concentration and is pumped until the capillary is flushed. (e) The pH is lowered again to neutralize the purple protein, which is then eluted with the bulk flow of the buffer solution.

An electric field is generated between the membranes, in the direction of the bulk flow,

by a positive electric potential at the inlet and a ground potential at the outlet. This is termed the separation region or separation capillary. The pH of the sample buffer is higher than the pI of the proteins, which ensures a net negative charge. The sample mixture is introduced as shown in Figure 4.5a. The proteins electric field experience an electrophoretic force towards the positive membrane as shown in Figure 4.5b. Any protein which enters the separation region experiences an electrophoretic force greater than the hydrodynamic force, preventing elution. As time progresses, the concentration of the proteins begins to increase near the membrane. Once an adequate concentration has been achieved, a pure buffer solution is pumped through, collecting any remaining proteins up stream of the membrane, as shown in Figure 4.5c. The pH of the buffer solution is then lowered to match the higher pI protein, in this case the red protein. Figure 4.5d shows the red protein is neutralized, illustrated by the loss of a solid boundary, and begins to elute. Once the red protein completed eluted from the system and collected, the pH is lowered again to match the pI of the purple protein. This protein is then eluted and collected as shown in Figure 4.5e. It is noteworthy that the pH step-gradient could be used for more proteins which are concentrated at the inlet.

4.2 2D COMSOL Simulation

The simplified calculations to produce the velocity plot serve as a guide to more accurate simulations. The syringe pump can deliver flow rates in the $\mu\text{L}/\text{min}$, nL/min , or pL/min range. It is clear from the velocity plot that for the capillary geometry, the nL/min flow rate range is the right starting point. To develop a more accurate model of the electrokinetic behaviour of the analytes, a 2D model was generated in COMSOL. The following physics modules were coupled together to solve for the complete solution: creeping flow to solve for the laminar and low Reynolds flow; Electrostatics to solve for the electric field; and transport of diluted species (TDS) to incorporate the concentration of the dilute analytes. Coupling these three modules together solves the transient transport behaviour of the analytes caused by the convective flow and migration in an electric field. Since the capillaries used in experiments are circular, the 2D model is treated as axisymmetric in the simulation, which

greatly reduces computational costs.

The liquid used in simulations was assumed to be water, for which only three properties are used: the dynamic viscosity set to 0.001 Pa·s; density set to 998 kg/m³; and relative permittivity set to 80. To model the charge behaviour of each analytes, step functions were used to determine the net charge as a function of time. The step function serves to simplify simulating pH changes of the buffer solution. Although 2D simulations are less computationally expensive than 3D, simulating the effects over a capillary length on the order of centimeters with a diameter 320 μm would not be computational cost effective. Therefore, the simulated length of the capillary is reduced to 3000 μm, and the potential difference is chosen to achieve an electric field strength of 10 kV/m. A flow rate of 400 nL/min and simulation time of 60 seconds were used.

4.2.1 Velocity Field Equations

The creeping flow module used in generating the steady state velocity field is governed by the following equations:

$$\rho \frac{\partial \mathbf{u}}{\partial t} = \nabla \cdot [-p\mathbf{I} + \mu(\nabla \mathbf{u} + (\nabla \mathbf{u})^T)] + \mathbf{F} \quad (4.6)$$

$$\rho \nabla \cdot \mathbf{u} = 0 \quad (4.7)$$

where \mathbf{F} represents external body forces such as gravity, or the electric body force, responsible for electroosmotic flow. The creeping flow module allows inertial terms to be neglected which eliminates the left hand side of Equation 4.6, which reduces to the linear Stokes equation (Equation 2.4) with the addition of body forces. Gravity can be neglected at the small scales since the Froude number, which compares inertial forces to the gravitational force, is very small. Since the low Reynolds number indicates inertial forces are negligible to viscous forces, gravitational forces will be further negligible compared to viscous forces. As discussed in Section 3.10, electroosmotic flow is assumed to have been suppressed,

which allows for the assumption of no electric body force.

4.2.2 Transport of Diluted Species Equations

The transport of diluted species (TDS) module uses the convection-diffusion equation to solve for the time-dependent concentration field:

$$\frac{\partial c_i}{\partial t} + \nabla(c_i \mathbf{u}_b + c_i \mathbf{u}_{ep,i}) - \mathcal{D}_i \nabla^2 c_i = \mathcal{R}_i \quad (4.8)$$

where c_i is the molar concentration of species i , \mathbf{u}_b is the velocity field, $\mathbf{u}_{ep,i}$ is the electrophoretic velocity of species i , \mathcal{D}_i is the diffusion coefficient of species i , and \mathcal{R}_i is the volumetric production rate of species i by chemical reaction. The chemical reaction rate for all simulations was zero. Simulations assumed an initial concentration in a specified subdomain of the simulation domain. Inflow of chemical species is assumed zero at the inlet and walls, and an outflow condition was applied to the outlet boundary.

4.2.3 Electrostatics Equations

The electrostatic module was used to create the electric field within the simulation domain. The governing equations are:

$$\nabla \cdot \mathbf{D} = \rho_{el} \quad (4.9)$$

$$\mathbf{E} = -\nabla V \quad (4.10)$$

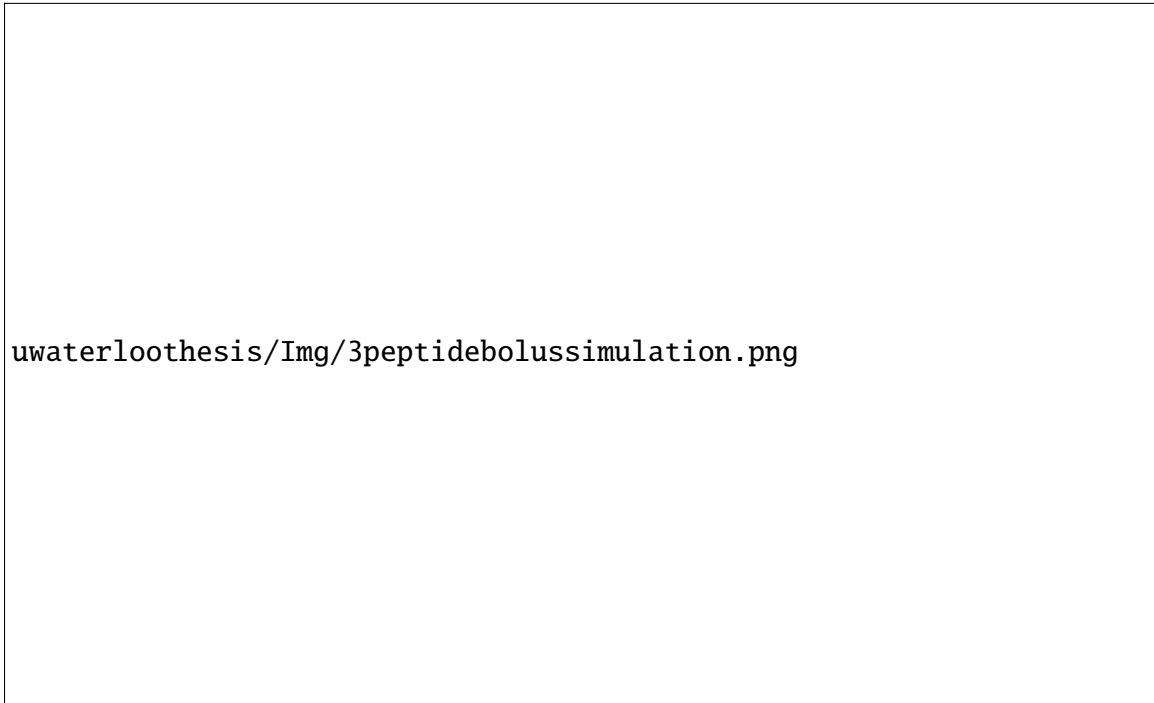
where \mathbf{D} is the electric displacement field, ρ_{el} is the electric charge density, \mathbf{E} is the electric field, and V is the electric potential. The transport mechanisms for the TDS module allow for convection and migration in an electric field.

4.2.4 Equation Coupling

Adding a multiphysics coupling between the modules allows the solutions to be solved simultaneously through a time dependent study. However, given the steady-state nature of a constant flow rate, the solution to the flow field can first be solved independently as a stationary *study step*. For a capillary, the velocity field should converge to the Hagen-Poiseuille flow solution. The same can be done for the electrostatics module which will compute a steady state solution for the potential field. Finally a time dependent study step can be applied to the concentration field. Performing the study in this manner allows for faster solutions to be obtained. When modifying parameters which affect the time dependent study only, the flow field and potential field solutions do not need to be recalculated for each iteration.

4.2.5 Peptide Simulation

The first simulation performed, as shown in Figure 4.6, shows three peptides starting together as a bolus with initial concentration of 1 mol/m^3 . Using the Nernst-Einstein relationship, the diffusion coefficient for the peptides with estimated radii of 0.5 nm each, and at a temperature of 298 K, is $4.4 \times 10^{-10} \text{ m}^2 \text{ s}^{-1}$. One peptide is neutral, simulating the pH of the buffer being at its pI point. The other two peptides have a net charge of $z = -1$ for the $t < 20$ seconds. The neutral peptide migrates as expected, referring to Figure 2.4. The two negatively charged peptides concentrate at the electrode wall. The electrode wall, having a height of the initial bolus, represents the electrode membrane of the capillary cartridge shown in Figure 2.7. At $t = 20 \text{ s}$, the step function modifies the net charge of one of the peptides to $z = 0$. This peptide begins to migrate due to the convective flow and diffuses slowly towards the center of the capillary. At $t = 40 \text{ s}$ another step function modifies the charge of the remaining peptide to $z = 0$, simulating a pH which is at its pI point.



uwaterloothesis/Img/3peptidebolussimulation.png

Figure 4.6 Three peptides with diffusion coefficients of 4.4×10^{-10} m²/s. The first peptide is electrically neutral and can be seen moving due to the convective flow field. The charged species are concentrated at the electrode membrane wall. At $t = 20$ and 40 s, the charge becomes zero for the second and third peptide respectively.

This peptide behaves the same as the second and migrates with convection and diffuses towards the center. This simulation demonstrates that in these conditions, sequential separation of proteins from high pI to low pI can be achieved, with charged peptides concentrating at the inlet membrane. The max range of the colour bands was set to be limited to the starting concentration because the concentration of the charged species increased by a factor of 40 over 20 seconds, which makes visualizing the neutrally charged species migrating to the exit nearly impossible.

4.2.6 Protein Simulation

The simulation was run again, only lowering the diffusion coefficient to 8×10^{-11} m²/s. The neutral protein behaved similarly to the peptide, however, with the lower diffusion coefficient the band remained sharper for a longer duration. This is expected since the Peclet number

for a protein would be higher because the Peclet number is inversely proportional to the diffusion coefficient. The charged species that concentrated on the membrane wall, after their release migrated as a concentrated ring. Since the L/D ratio in this simulation was so short, diffusion did not have enough time to spread the mixture.



Figure 4.7 Three proteins with diffusion coefficients of $8.0 \times 10^{-11} \text{ m}^2/\text{s}$. The first protein is electrically neutral and can be seen moving due to the convective flow field. The charged species were concentrated at the electrode membrane wall. At $t = 20$ and 40 s , the charge becomes zero for the second and third protein respectively. Flow rate = $400 \text{ nL}/\text{min}$

The above figure highlights how a decrease in the diffusion constant by 80% produces a much different picture. The charged protein upon release moves with the bulk flow near the walls for a greater length of the capillary. Also, because this simulation plots the concentration of three different proteins, it hides information about the charged proteins. Plotting only the first charged protein, which loses its charge at $t = 20 \text{ s}$ shows its behaviour more clearly. Figure 4.8 shows an oblique view of the capillary with equally spaced planes to show the radial concentration. For $t < 20 \text{ s}$, the concentration of the protein near the center of the capillary experiences a bulk flow velocity greater than the electrophoretic velocity, therefore, elutes with the neutrally charged protein. This indicates the prescribed

volumetric flow rate is too high. Concentration of protein near the wall experiences a large enough electrophoretic force to overcome the hydrodynamic drag, it further concentrates along the wall. For $t > 20$ s, concentrated protein is released, but remains close to the walls in a ring structure.

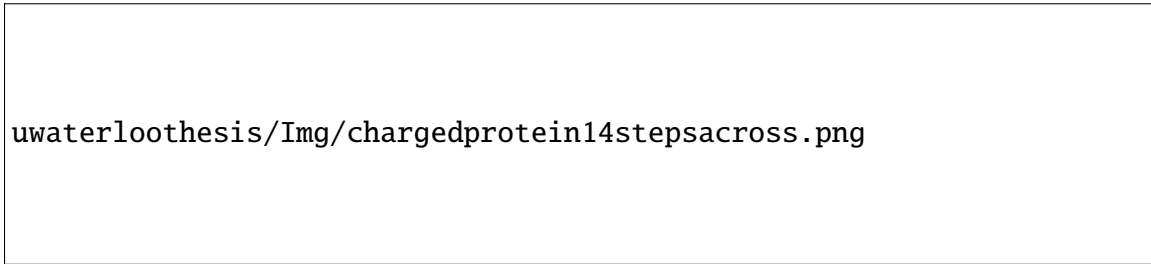


Figure 4.8 Simulation of one protein with charge step change from $z = -1$ to 0 , at $t = 20$ s. Flow rate = 400 nL/min

To improve protein capture at the inlet electrode, the flow rate needs to be reduced. Figure 4.9 shows the simulation results with the flow rate lowered to 100 nL/min. This reduced flow rate required a longer simulation duration of 240 s and the time when the charge of the protein was reduced to zero occurred at $t = 80$ s. This reduced flow rate had two obvious consequences: 1) the amount of protein lost to the bulk flow was significantly reduced; 2) the lower bulk flow rate lowered the Peclet number, which allowed proteins to spread radially to the center over the length of the simulated capillary.

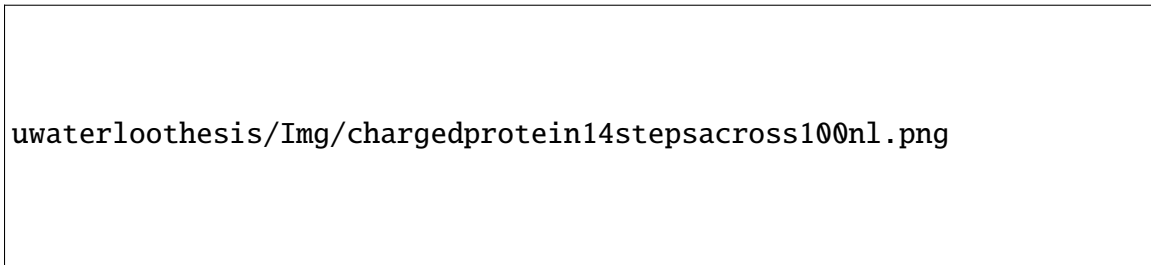


Figure 4.9 Simulation of one protein with charge step change from $z = -1$ to 0 , at $t = 80$ s. Flow rate = 100 nL/min.

To address if and how much of the proteins are lost due to the bulk flow rate, the concentration of each species was integrated over the entire simulation domain every 10 seconds to generate the plot shown in Figure 4.10. The plot shows the total molar amount

of each protein expressed as a percentage. As the proteins reach the exit, the total amount decreases.

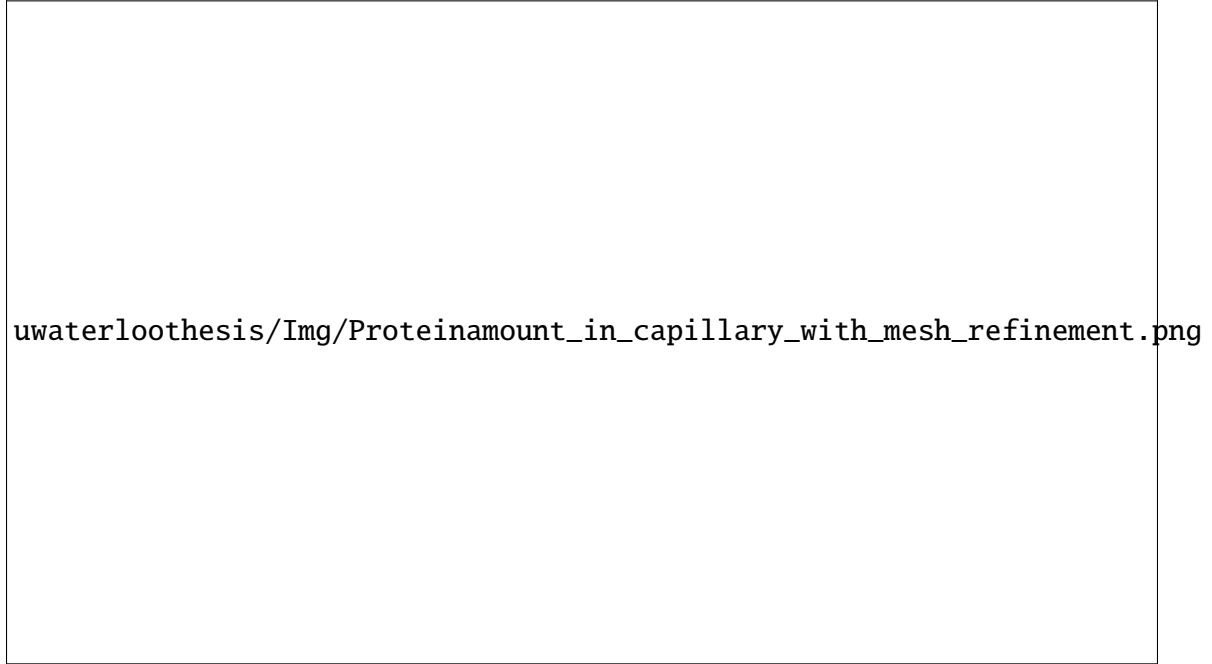


Figure 4.10 Total molar amount of three proteins within the simulation domain versus time. Dotted lines represent a coarse mesh, and the solid lines represent a finer mesh. Residence times are identical, however, the dotted lines show an error of approximately 3% in the total amount of the two charged proteins, B and C, before their charges are reduced to zero. The error is reduced to < 1% upon mesh refinement.

The dotted curves representing the first simulation showed an increase in the percentage of the two charged proteins. This nonphysical result leads to the hypothesis that this was a numerical error being a function of the mesh size. The mesh was adjusted to be a finer mesh in the region where the proteins were observed to be concentrating. The second simulation with the refined mesh illustrated by the solid curves shows a substantial reduction in the observed error. However, after the charged proteins become neutral, the dotted and solid curves overlap, indicating the original, coarse mesh, was accurate in predicting residence times. Therefore, further mesh refinement to remove the error would not lead to a more accurate solution. The corner plot visually exaggerates the error. The results of these simulation confirm that the flow rate range for proteins and peptides will lie in between 100 - 400 nL/min.

4.3 IEF Marker Separations

To visualize the separation process, fluorescent IEF markers were chosen. Figure 4.11 shows the experimental setup used for visualizing the separation process.

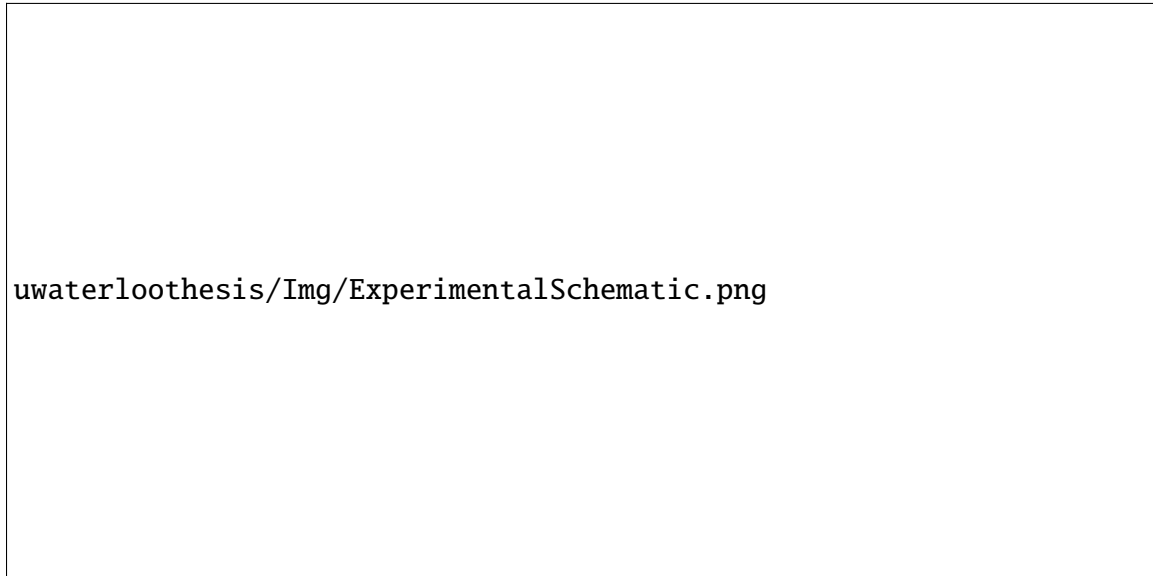


Figure 4.11 This schematic shows the equipment used in performing pH gradient elution MBE separations, and capturing fluorescent images.

4.3.1 Determining Experimental Parameters

The velocity plot and COMSOL simulations only provide guidance in choosing appropriate experimental parameters such as flow rate and electric field strength. To perform the separation process, the flow rate must be optimized such that the neutral analytes can elute, and the charged analytes experience a large enough electric force to overcome the hydrodynamic drag force. This section outlines the methodology for determining acceptable parameters.

4.3.1.1 Electric Field Response

To confirm the markers responded to the presence of an applied electric field, the intensity of the signal, measured from 0-255, was plotted against time. Figure 4.12(a) shows the

control image at the top of the sequence which was the capillary filled with only 10 mM tris buffer at pH 9.0. The lower edge of the capillary appears bright due to reflected light from the mercury burner. The control image was used to remove background intensity that did not contribute to the fluorescent images. The capillary was then filled with the buffer and pI 7.6 IEF marker at a constant flow rate of 400 nL/min. This flow rate is constant throughout the experiment. The red line indicates the pixels used to measure the image intensity. The imaging software displayed a live histogram while the CCD camera was on, and steady state was observed once the histogram stabilized, which occurred on average after one minute. After the fluorescence across the viewing region of the capillary reached a steady state, an image was taken to represent $t = 0$ min, with no electrical field. An electric field of 200 V/cm was applied across the capillary and images were taken at $t = 3, 4$ and 5 minutes.

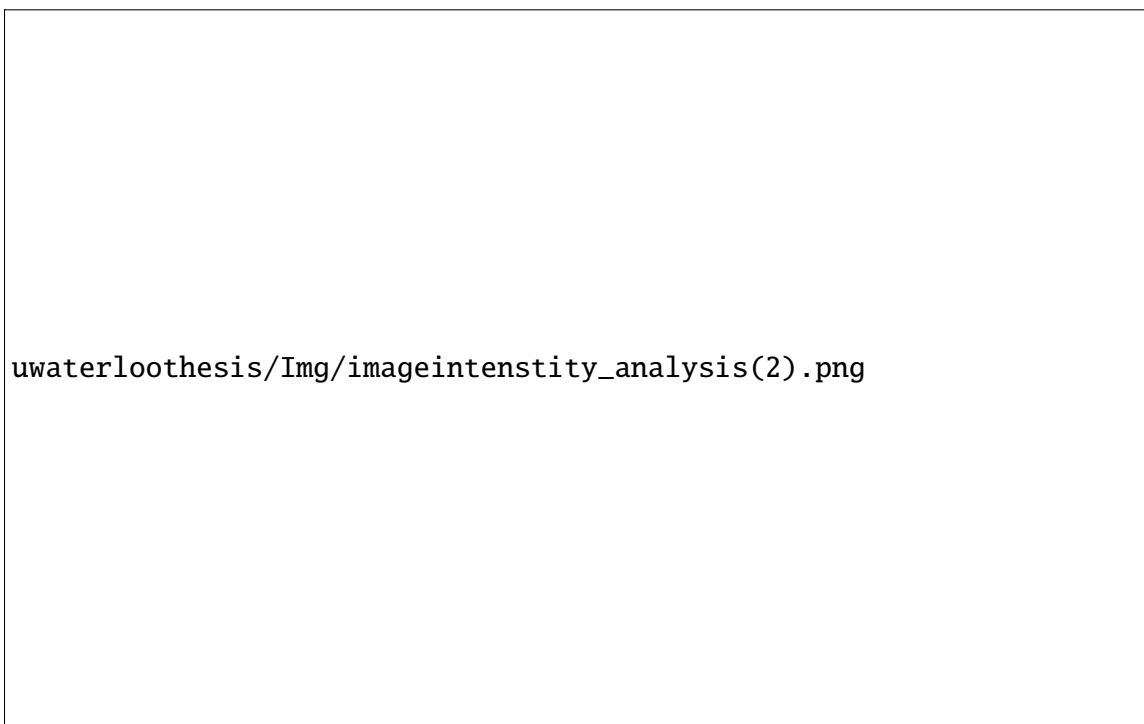


Figure 4.12 (a) Snap shots of an IEF marker with and without the presence of an electric field to show an electrophoretic response. The red lines represent the location for intensity analysis in the following plots. (b) Image intensity values plotted along the channel length. The black line is the steady-state profile of fluorescence intensity. The blue, red and yellow curves are showing a reduced intensity profile at 3, 4 and 5 minutes respectively. (c) Intensity difference plots over time to show the change relative to the steady-state curve plotted in black.

Figure 4.12(b) is a plot of intensity over the length of the capillary. The exponential decay of each curve is due to photo-bleaching [62]. The vertical shift in intensity over the viewed section of the capillary confirmed the IEF marker's response to the electric field. This test, however, does not conclude the net velocity direction being with or against the bulk flow direction. Figure 4.12(c) is the difference, or total loss in intensity for $t = 3, 4$ and 5 minutes, with respect to the black curve.

4.3.1.2 Stacking Effect

The design of the capillary cartridge prevented direct imaging of the IEF markers on the membrane and direct confirmation that they stack and concentrate at the electrode. However, as simulated in Figure 4.6, concentrated markers should show up near the inlet with increased fluorescent intensity. A 10 mM tris buffer solution at pH 9.0 was prepared. 50 μL of buffer and 2 μL of pI 7.6 was combined into a 100 μL glass syringe, which will be called the *sample solution*. The sample solution was injected into the cartridge to completely fill the separation capillary at a flow rate of 2000 nL/min. The syringe was then turned off and an electric field of 100V/cm was applied for 10 minutes. Due to photo-bleaching, the mercury burner shutter was closed so as to not diminish the fluorescent response of the marker already in the separation capillary. After 10 minutes the electric field was turned off, the mercury burner shutter was opened, and the syringe pump was set to 200 nL/min. Images were taken automatically at 30 second intervals. As shown in Figure 4.13, the presence of a concentrated band of pI 7.6 marker can be seen moving from left to right, before diminishing.



Figure 4.13 pI 7.6 IEF marker under the influence of an electric field and no bulk flow permits stacking at the inlet (left) under a constant electric field of 200 V/cm. After 10 minutes of stacking, the electric field was removed and a bulk flow of 100 nL/min was applied. Fluorescent images capture the concentrated marker band from left to right.

4.3.1.3 Flow Rate

To find a suitable flow rate, the net velocity of the markers should be towards the inlet. Without knowing the electrophoretic mobility, a simple test was performed to visualize the net velocity response. Using the method described to determine stacking, given a long enough stacking time, and capturing images close to the inlet, a distinct edge could be seen. From Equation 4.3, four cases could be qualitatively demonstrated. Figure 4.14(i) is the case where there is no bulk flow, therefore the net migration of the fluorescent markers could be seen moving in the electrophoretic velocity direction. Figure 4.14(ii) is the case where the bulk flow velocity is less than the electrophoretic velocity, whereby the markers migrate in the same direction as case (i), albeit at a slower velocity. Figure 4.14(iii) is the case where the bulk flow velocity and electrophoretic velocity balance, and the markers do not move. Finally, Figure 4.14(iv) is when the bulk velocity is greater than the electrophoretic velocity and the markers move away from the inlet.

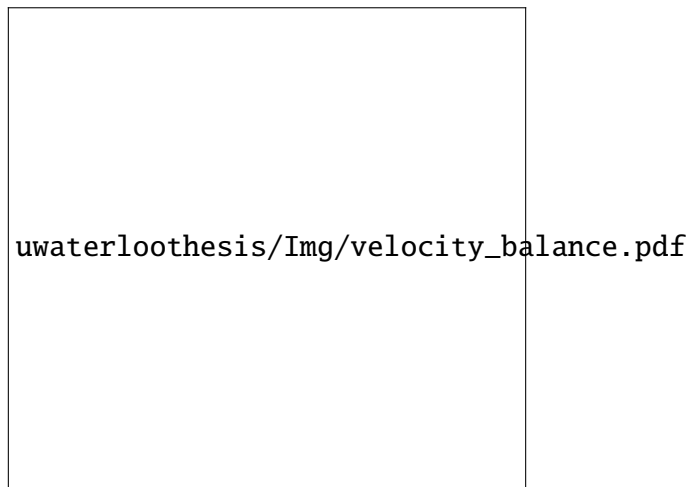


Figure 4.14 This illustration represents a method for determining the direction response of an IEF marker in a capillary. Four conditions are shown, where the first image represents the initial position of an injected IEF sample. i) Without pressure driven flow, the electric field will cause the IEF marker to migrate towards the inlet. ii) when the bulk velocity is lower than the electrophoretic velocity, the net velocity is towards the inlet, but at a slower rate than condition i). iii) shows a balance between the electrophoretic velocity and average bulk velocity, and the fluorescent boundary will appear stationary. iv) shows the electrophoretic velocity is lower than the average bulk velocity as the boundary moves towards the outlet. Case iii) can be used to experimentally indicate that the average bulk velocity set by the syringe pump should be slightly lowered to achieve condition ii).

This test was performed with 50 mM tris at pH 8.5 with pI 7.6 marker. All four cases were found with an electric field of 100 V/cm. The flow rates found for cases i - iv were 0, 180, 200, 300 nL/min respectively. Case (ii) being the ideal case, where there is a net velocity towards the inlet was chosen as the flow rate to perform separation experiments. The diagram in Figure 4.14 highly exaggerates the distinction between the edge of the protein band. This test is not intended to be as effective as other procedures for measuring electrophoretic mobility, but was done as a simple, fast, and cheap way of finding an acceptable flow rate which would allow the separation mechanism to work.

4.3.1.4 Conductivity

To reduce Joule heating effects, the current draw in the capillary should be minimized while maintaining an acceptable buffering capacity. Without a conductivity meter, the conductivity was calculated from the geometry of the capillary and by measuring the current draw for a given voltage drop. The conductance, G of a buffer in a capillary can be found from:

$$G = \frac{A_c}{L} \sigma_b \quad (4.11)$$

where A_c is the internal cross-sectional area of the capillary, L is the length of the capillary, and σ_b is the conductivity of the buffer. The current is related to the conductance through Equation 2.21, and can be used to determine the conductivity as:

$$\sigma_b = \frac{I L}{V A_c} \quad (4.12)$$

In the case of the capillary cartridge, the electrodes are not at the separation capillary membrane walls, therefore the true voltage at the inlet and outlet of the capillary is not known. To obtain a more accurate value for the conductance, the voltage at the membrane wall should be found using the reservoir area and distance from the electrode to the membrane. A 1D representation of the capillary cartridge would be three resistors in series. However, due

to the small cross-sectional area of the capillary, the conductance through the capillary is orders of magnitude larger than the reservoir. Therefore, it can be assumed that the voltage drop through the reservoir buffer is negligible and the membrane potential equivalent to the applied electrode potential.

The current for a range of tris buffer compositions are shown in Table 4.2.

Table 4.2 Calculated tris buffer conductivity by measuring current draw in the capillary cartridge with applied potential of 500V over 5cm long capillary with 320 μm internal diameter, with an uncertainty of $\pm 6\%$.

pH	Concentration (mM)	Current (μA)	σ_b (mS/cm)
7.5	20	98	1.22
7.5	50	236	2.93
7.5	90	390	4.85
8.0	20	83	1.03
8.0	50	188	2.34
8.0	100	300	3.73
8.5	18	44	0.55
8.5	50	125	1.55
8.5	100	180	2.24
8.5	100	187	2.33
9.0	20	33	0.41
9.0	50	59	0.73
9.0	100	125	1.55

The data obtained was used to plot the conductivity versus concentration for a range of pH values, shown in Figure 4.15.



Figure 4.15 Conductivity versus concentration for tris buffer at pH 7.5, 8.0, 8.5 and 9.0

In the case of tris buffer, there is a stronger correlation between conductivity and concentration at lower pH. In order to minimize current draw, lower concentrations of the buffer should perform better. For the reservoir, a higher concentration can be used to increase the buffering capacity, without increasing the current draw due to its larger conductance compared to the capillary.

4.3.2 Concentration Factor

Determining the total concentration of the purified sample could be simulated accurately if the entire domain of the capillary cartridge is modelled. Since the length of the capillary cartridge is orders of magnitude larger than the diameter, even a 2D simulation would take a very long time to run. A faster way is through a control volume analysis. Considering the geometry of the capillary, and a constant flow rate of 180 nL/min, after 180 minutes the concentration increases by a factor of 7.6. This value is only an approximation and the derivation can be found in Appendix B.

4.3.3 Separations

A separation test was performed to separate two markers with a large pI difference, in this case, pI 5.2 and 8.1. 50 μ L of 10 mM tris buffer at pH 8.1 was prepared with 2 μ L of each IEF marker stock-solution as the *sample solution*. 30 μ L of the sample solution was stored in a 0.2 μ L Eppendorf conical vial as the control sample. The sample solution was injected into the entire capillary cartridge at 2000 nL/min. Once filled, an electric field of 200 V/cm and a flow rate of 200 nL/min was applied. The experiment was run for 2.5 hours, which yielded 30 μ L of a sample collected at the outlet. This sample was expected to contain the buffer solution with only the pI 8.1 marker.

To validate the separation results, isoelectric focusing was performed at AES (Cambridge, ON) using their CE Infinite IEF machine. The control vial and pI 8.1 vial were mixed with a carrier ampholytes solution with reference markers, prepared by AES, in 25:1 and 50:1 ratio respectively. The carrier ampholyte solution is needed to generate the linear pH gradient from pH 3 - 10. The carrier ampholyte solution also contained reference markers at pI 4.22 and 9.46. These reference markers are used to calculate the pH values from the pixel location. The results of the separation test are shown in Figure 4.16. The control (black) shows the two reference markers, as well as the two pI markers. There is a discrepancy between the values reported by Sigma-Aldrich and what the CE Infinite determined the pI points to be. The pI 8.1 (red) plot shows only three distinct peaks, which is concluded to be the two reference markers and the separated pI 8.1 marker. This indicates that the separation mechanism did perform as expected.

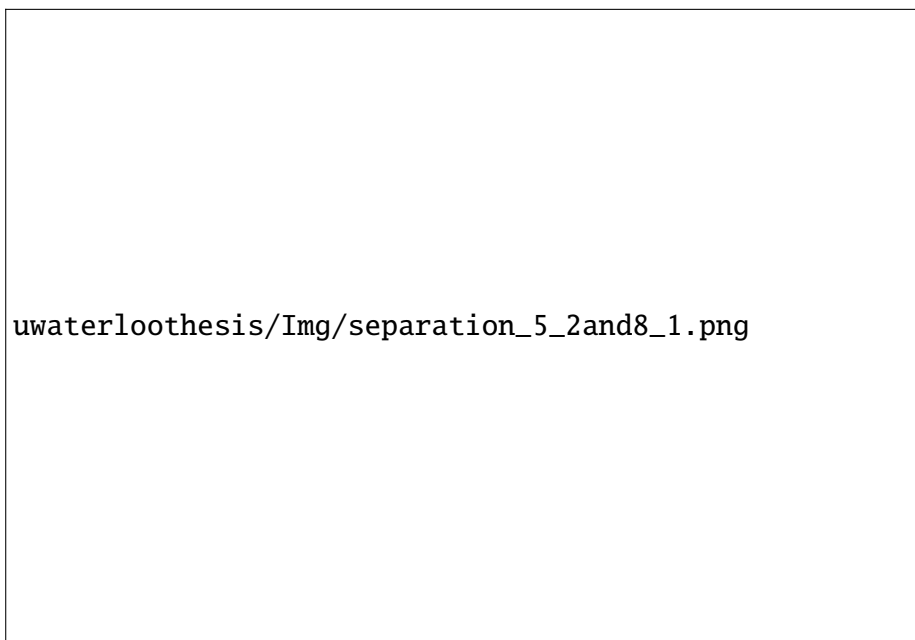


Figure 4.16 Separation results performed on the CE Infinite IEF machine. The top plot (black) is the control plot of the IEF markers 5.2 and 8.1 with the reference markers (pI 4.22 and 9.46) provided by AES. The bottom plot (red) shows the purification of the control mixture to only contain the pI 8.1 marker.

To further investigate the performance of this mechanism, three markers were chosen to be separated: pI 5.2, 7.6 and 9.0. In this test, the applied electric field was lowered to 100 V/cm to reduce Joule heating, and the flow rate was lowered to 180 nL/min. The buffer compositions for the experiment are listed in Table 4.3. The sample solution contained 80 μ L of the sample buffer and 2 μ L of each IEF marker stock solution. Due to the variability in the pI point for the markers in the first experiment, the *fractionation buffer* (FB) was made to have a slightly lower pH at 7.5, to compensate for the pI and ensure the marker would have a zero or net positive charge.

Table 4.3 Buffer compositions used in separating three IEF markers

Buffer	pH	Concentration (mM)	Type
Sample Buffer, SB	9.0	20	Tris
Fractionation Buffer, FB	7.5	20	Tris
Inlet Reservoir, RB+	9.0	100	Tris
Outlet reservoir, RB-	5.2	50	Sodium Acetate

The separation of the pI 9.0 marker lasted for 2.5 hours. During that time, the pI 7.6 and pI 5.2 were expected to stack up at inlet. Therefore, to collect the pI 7.6 using the fractionation buffer, the time to elute can be approximated using the average bulk velocity and capillary lengths to find the elution time of the marker. The marker was estimated to take 10 minutes to reach the end of the transfer capillary. To account for band broadening, collection was stopped after 12 min. For the pI 5.2 marker the electric field was removed and allowed to elute with the bulk flow velocity. The collected fractionated samples were analyzed on the CE Infinite. Figure 4.17 shows the separation results. The ratio of carrier ampholyte solution for the control, pI 9.0, pI 7.6, and pI 5.2 samples were 1:1, 1:1, 6.5:1, and 3:1 respectively.



Figure 4.17 Validation of separation for pI 5.2 (green), 7.6 (blue) and 9.0 (red). The black electropherogram is the control sample of all three IEF Markers with equal concentrations.


The graphs show excellent results for separating and collecting the pI 9.0 and 7.6. The pI 5.2 did not show up in any of the electropherograms. The absorbance signal of the pI 5.2 marker compared to the 7.6 and 9.0 is significantly lower in the control sample, therefore, the separation process most likely reduced the concentration of the pI 5.2 marker below the

absorbance threshold of the CE Infinite system.

4.4 Instrumentation Prototyping

Performing separation experiments with the setup shown in Figure 4.11 proved to be time consuming, tedious, and introduced sources of error for a number of factors. Firstly, switching between syringes filled with different buffer solutions required the syringe pump to be turned off to swap syringes. Swapping syringes manually had the potential for introducing air bubbles which would cause significant drops in current, and potentially ruin the experiment. In order to remove a syringe, the custom capillary adapter would also need to be disconnected since attempting to unscrew the syringe from the adapter would often lead to accidental tugging of the capillary cartridge which could break it. Eventually the microscope itself was unnecessary in performing the separations. To reduce errors, speed up buffer switching, improve safety, and further automate the process, a prototype system was required.

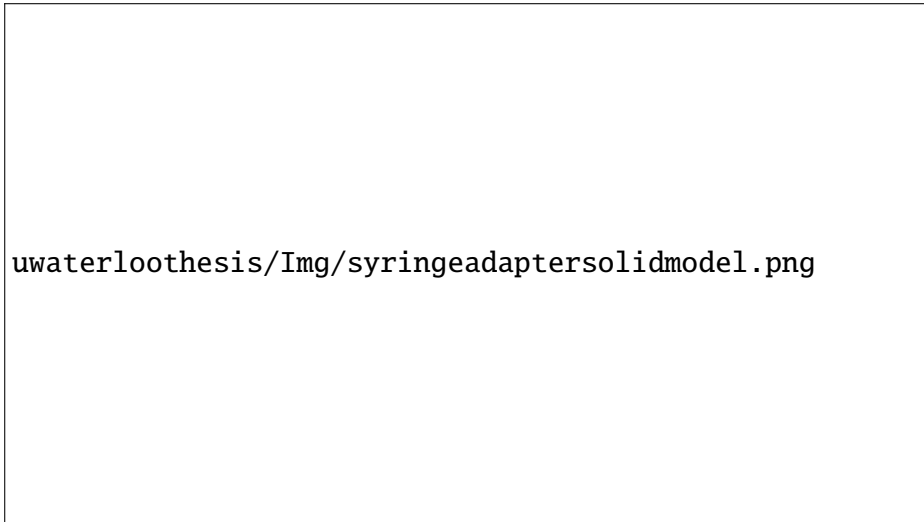
The prototype system needed three new subsystems to automate the process: 1) A syringe controller system; 2) a path selection system; 3) a collection system. Figure 4.18 is a schematic of the originally intended prototype which included custom software intended to control all components. However, due to time constraints, the automated collections system and custom software could not be developed. Despite this loss in automation, the constructed prototype proved to be effective in increasing productivity, user safety, and repeatability.



uwaterloothesis/Img/automatedprototypeschematic.png

Figure 4.18 Automated prototype schematic.

To keep costs down, the majority of the prototype was constructed with off-the-shelf components, and existing hardware was incorporated. The syringe pump was only capable of actuating two syringes. In order to expand the effectiveness of the pump, a custom adapter was designed using SolidWorks as shown in Figure 4.19, and 3D printed in ABS polymer.



uwaterloothesis/Img/syringeadaptersolidmodel.png

Figure 4.19 Solid model of syringe adapter and pusher block designed to hold up to five syringes and mounted directly to the Harvard Pico Plus syringe pump.

To switch between buffers, a path selector and microelectric actuator was needed to

direct fluid flow between different syringes loaded with different buffers. As discussed in Section 3.9, the flow-through option for the selector was required because of the syringe pump. The syringe pump actuates all five syringes during operation; therefore, the fluid must always be connected to an outlet. It is more common for the unused paths to be self-closing, which if installed in this system, would over pressurize the lines and cause damage to the equipment. Fluid paths not connected to the capillary cartridge are directed into a waste container.

The enclosure for the prototype was designed using 80/20 aluminum extrusion purchased through McMaster-Carr. The 80/20 system (8020.net) is used to simplify the construction of guards, machinery, enclosures, and other industrial equipment through standardized components. The system offers a variety of connectors, hinges, panel-mounts, and other components intended to interface with the t-slot design of the aluminum extrusion. For this reason, an enclosure was designed using 80/20 which reduced design time and construction, as well as cost. Figure 4.20 shows the enclosure designed in SolidWorks.

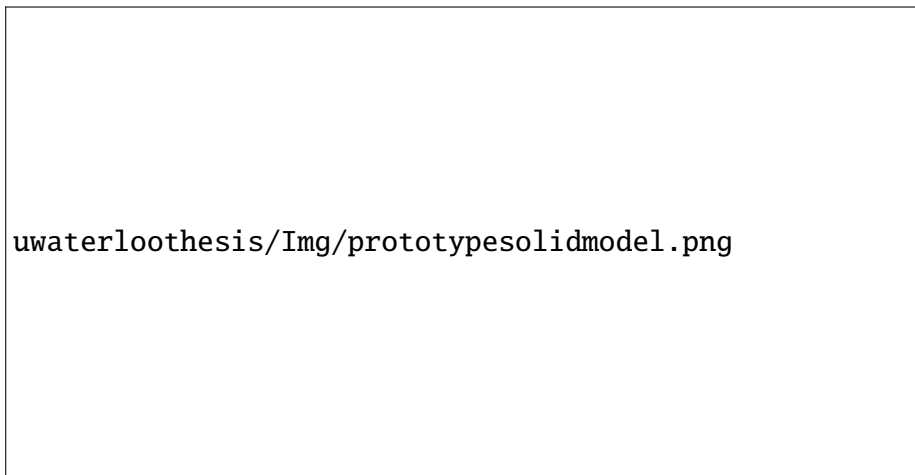


Figure 4.20 The model of the enclosure was used to determine an appropriate layout of the components so that tubing lengths connected to the syringe, actuator and capillary cartridge could be minimized.

The floor of the enclosure is made of perforated PVC sheet (not shown), chosen so that cable-ties could be used to hold down the power cables of all electrical components. This keeps cables organized and allows equipment to be removed without having to reroute

cables. Figure 4.21 shows the completed prototype.

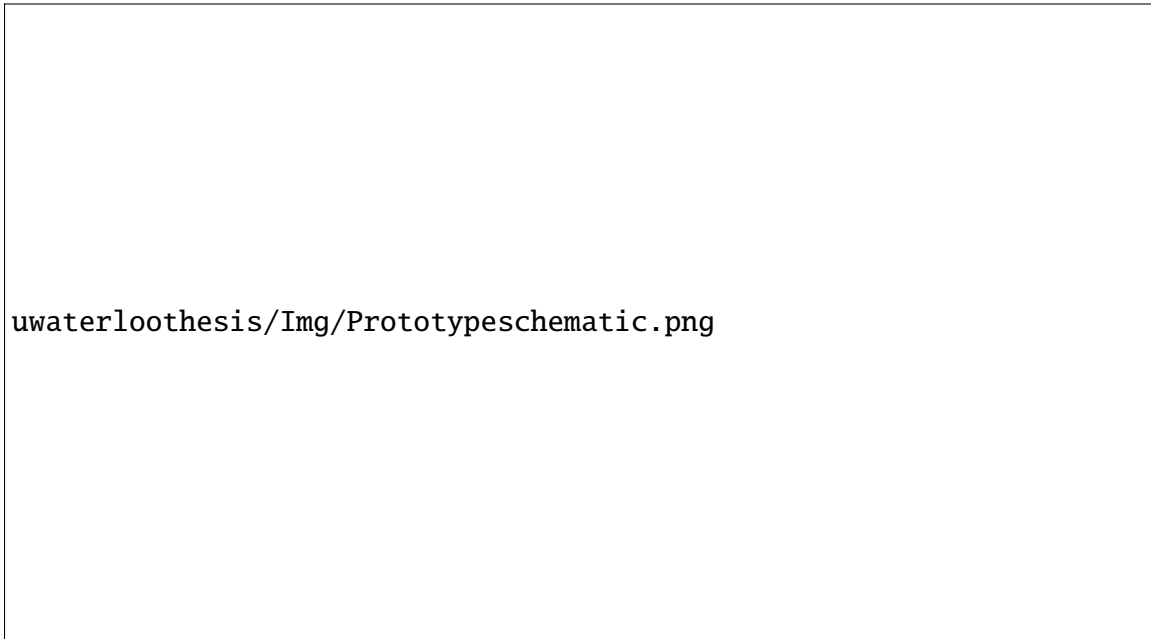


Figure 4.21 Automated fractionation system for performing pH gradient elution MBE.

The prototype system does not allow for fluorescent imaging. To monitor the experiments, a live spreadsheet was developed to record the voltage, current, and calculate the current slope. A sample of the spreadsheet used to track experiments is given in Appendix A.

4.5 Recommendations

Future works will need to explore the resolution of the technique in terms of a minimum difference between isoelectric points of neighbouring proteins. The closer the proteins are, the lower the electrophoretic mobility of the charged protein. Two paths toward high resolution separations can be taken: 1) Increase the electric field strength to larger values to ensure the electrophoretic force is high enough to overcome the countering drag force. This will ensure separation rates are maintained, but the drawback is significant Joule heating, which alters the pH of the buffer solution as the temperature changes. A method for controlling the temperature such as submerging the capillary cartridge in a water bath

may be possible. 2) reducing the bulk flow rate so that Joule heating is negligible. This will reduce the rate at which separations can occur, eliminating the advantage over using isoelectric focusing. However, due to the low cost, it may be possible to use multiple cartridges in parallel to compensate. This will produce challenges in flow control as the hydraulic resistance of each capillary cartridge would need to be very similar. In terms of the prototype, the syringe pump can only control effectively one syringe at a time, and buffers need to be made prior to experiments. Gradient generating buffers used in chromatography could be used with multiple syringe pumps. Two pumps could perform the mixing function in generating the specific buffer pH, while a third pump performs sample injection. The high voltage controller was used only out of convenience. Smaller, single channel high voltage supply can significantly reduce the footprint and cost of the device.

The stock concentrations of pI 5.2, 7.6 and 9.0 were all 1 mg/mL, however, the magnitude of their absorbance peaks in Figure 4.17 were approximately 0.05, 0.65 and 0.35 respectively. The signal of the pI 5.2 marker was likely initially too weak for the marker to be seen on its expected electropherogram (green). To validate future tests using the CE infinite, the concentration of each sample in the control solution should be adjusted such that their absorbance peaks are at least 0.35. It is expected that this change would have produced the expected signal for pI 5.2.

Chapter 5

Development of a Low Voltage Protein Separation Device

5.1 Motivation

In this chapter, the development and construction of a low voltage protein separation device using the mechanism described in Chapter 4 is described. In capillary electrophoresis, electric field strengths used can range from 300 to 800 V/cm [63], which in turn requires voltages in the kilovolt range as the lengths of capillaries are in the centimeter scale. In Chapter 4, the applied electric field was even lower at approximately 100 V/cm. The motivation to develop a low voltage system stems from a desire to eliminate electrolysis, which can be achieved if the applied potential is lower than the cell potential of water. The potential at which water will split is also a function of pH, which is described in a Pourbaix diagram or water E-pH diagram [64]. Given a low enough potential, the electrolysis reactions are unable to occur. Electrolysis is responsible for creating instability in the buffer pH. It generates gas bubbles which requires complicated fabrication processes to incorporate reservoirs and membranes to isolate them from the separation capillary. To mitigate the effects of electrolysis, platinum is preferred as it is electrochemically stable, but is an expensive precious metal [17]. Eliminating electrolysis would reduce construction

costs and simplify designs of electrokinetic devices. The experiments presented in this chapter only attempt to characterize the device's ability to generate an adequate electric field without producing electrolysis products and make suggestions about future modifications which would enable the device to work with proteins.

5.2 Development

The electrophoretic velocity of a protein is a function of its mobility and the applied electric field. The electric field is simply defined as the potential drop over the length of a channel:

$$E_z = \frac{\Delta V}{L} \quad (5.1)$$

where E_z is the electric field in the axial direction of the channel length. As a starting point, if the required electric field strength is 1000 V/cm, and the electric potential is 1 V, the length of the channel must be reduced to a length of 10 μm . Although this is not feasible using a glass capillary, it is reasonable to assume using a porous membrane with straight pores and a thickness of 10 μm is feasible. A membrane with thousands of pores can then behave as thousands of capillary cartridges, without the need for a membrane barrier and reservoirs.

5.2.1 Membrane and Electrode Selection

The components required for constructing such a device would be a membrane, electrodes, and housing. A cross-section view of the membrane-electrode configuration is shown in Figure 5.1.

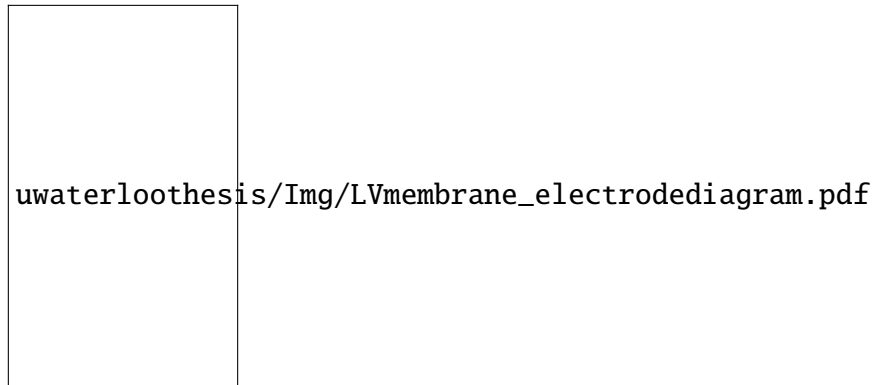


Figure 5.1 Cross sectional view of an ideal membrane pore and electrode configuration where L represents the thickness of the membrane. Electric field lines initiate and terminate at the electrodes but are parallel within the membrane pore.

The thickness, L represents the length over which the electric field is generated. The diagram also shows the anticipated electric field lines. Membranes are readily available from filter suppliers such as Sterlitech in a wide variety of pore sizes, coatings, and materials. Hydrophilic polycarbonate track-etched membranes (Sterlitech, WA) with 10 μm pore size were chosen. The properties of these membranes are listed in Table 5.1.

Table 5.1 Polycarbonate track-etched (PCTE) membrane properties.

Parameter	Value	Unit
Filter Diameter	13	mm
Pore Size	10	μm
Pore Density	1×10^5	pores/ cm^2
Thickness	10	μm
Material	Polycarbonate	
Part Number	PCT10013100	

Ideally, the membranes would be coated in a conductive layer to construct the cross-section shown in Figure 5.1. Gold coated membranes are available; however, they are cost prohibitive for the development of such a novel device. In the field of transmission electron microscopy (TEM), a wide variety of metallic TEM grids are used to capture small particles such as soot in order to take images and characterize physical properties. Although their main purpose is irrelevant for the purpose of this project, the precision of manufacturing these grids offered a cheap substitution to gold coated membranes. TEM

grids were purchased from Ted Pella (Redding, CA). A model of the TEM grid was made using SolidWorks shown in Figure 5.2. The mesh pattern creates empty boxes which will be called a *unit cell*. The figure also illustrates that there will be on average 16 pores per unit cell, which is derived from the pore density and area of the unit cell. Throughout the rest of this chapter TEM grids may simply be referred to as *grids*.

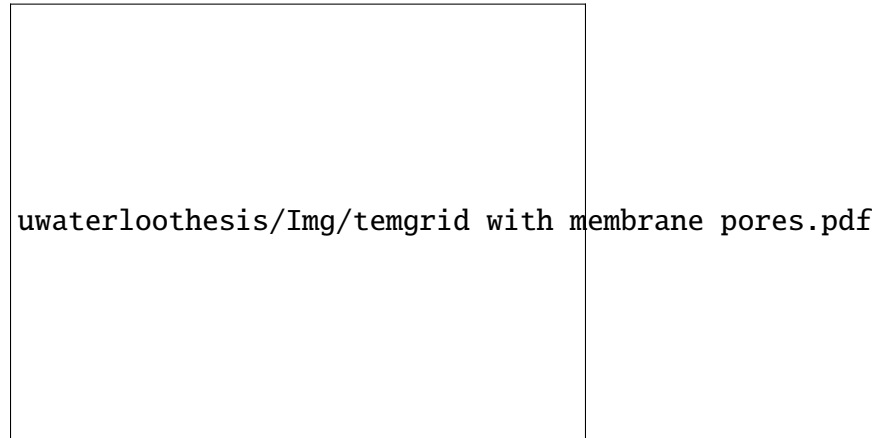


Figure 5.2 The image shows the standard TEM grid with a tab for manipulation. The zoomed in region represents a unit cell and shows the expected random distribution of pores for the PCTE membrane based on the pore density provided in Table 5.2.

TEM grids come in many different sizes, materials, and mesh shapes. Some variations include tabs to manipulate the grids with tweezers. The tabbed version was selected because it can act as an electrical connection source.

Table 5.2 TEM grid properties

Parameter	Value	Unit
Outside Diameter	3	mm
Pitch	169	μm
Hole Width	125	μm
Rim	350-400	μm
Thickness	25	μm
Bar Width	44	μm
Material	Nickel	
Part Number	3HGN150	

This geometric configuration of the TEM grid is only available in copper or nickel. Both

were purchased, however, the copper grids proved to be too easily deformable. The nickel grids were stiffer and able to be manipulated by hand without unwanted plastic deformation.

5.2.2 Chemicals

To test the effectiveness for the system to generate an adequate electric field it was beneficial to use an analyte that had a very high mobility which was not influenced by variables such as temperature and pH. For these reasons, the electrophoretic staining dye 7-naphthalenedisulfonic acid sodium salt or more commonly referred to as Ponceau S (Sigma-Aldrich Canada Co., Ontario) was chosen. The net charge of the molecule is $z = -4$ as indicated by the name. More chemical information can be found on PubChem using the identification number SID = 24898418. Literature on Ponceau S regarding the exact size or electrophoretic mobility could not be found, therefore its coefficient of diffusion can only be approximated. The molecule is a type of salt which is used to label proteins in Western blots. Based on the size of the structure, the diffusion coefficient would more closely match that of a peptide. Therefore, the coefficient of diffusion was assumed to be $1 \times 10^{-10} \text{m}^2/\text{s}$.

5.2.3 TEM Grid and Membrane Simulation (COMSOL)

The setup for the numerical simulations was the same as described in Section 4.2 in terms of the multiphysics used. The purpose of the simulations in this chapter is to show whether or not the geometry of the TEM grid and membrane structure will be able to produce the right conditions to prevent the charged species from passing through the membrane, and the exact locations the species will concentrate. From the unit cell description in the Section 5.2.1, the electric field was modeled in COMSOL using the electrostatics module.

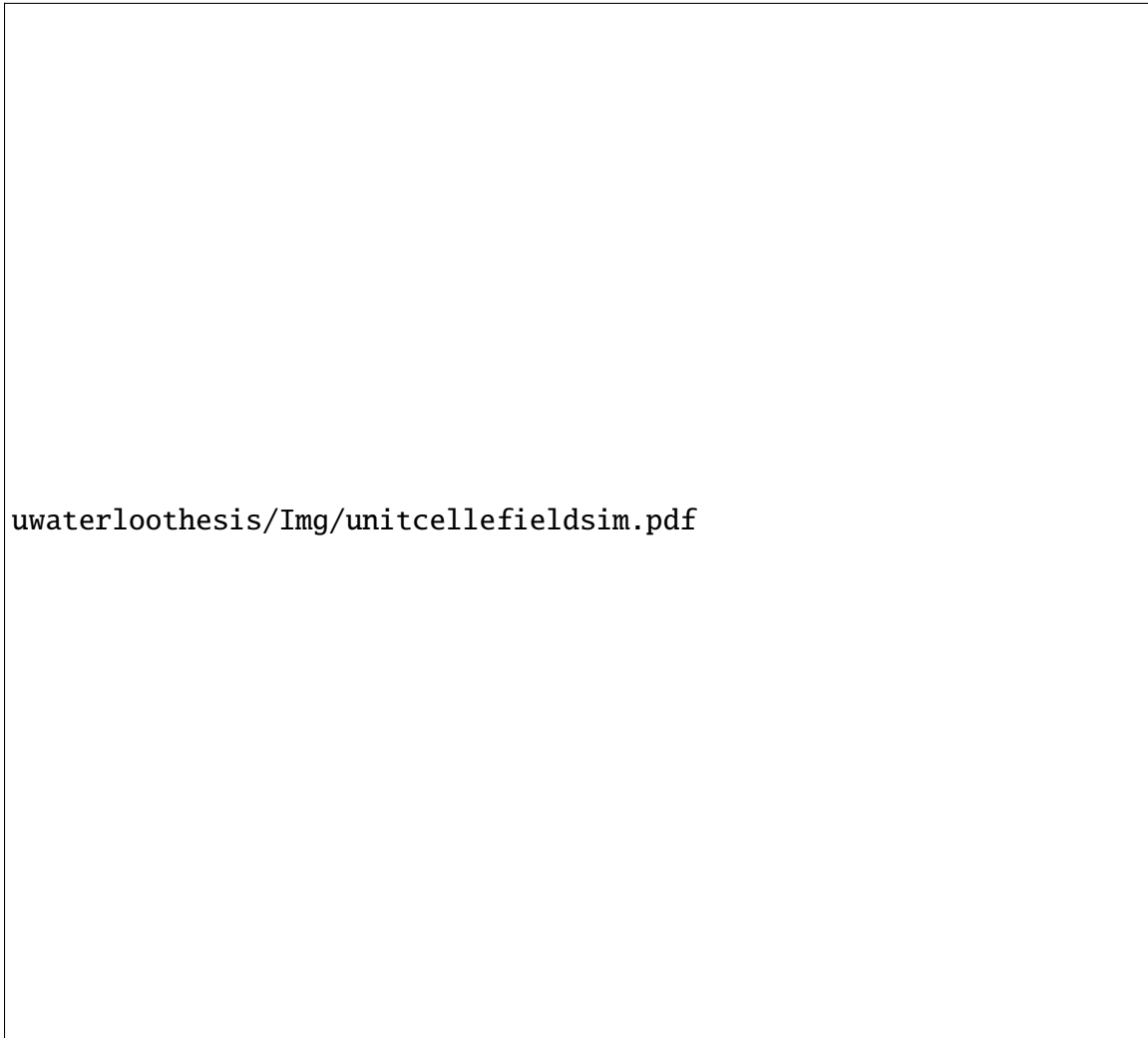


Figure 5.3 The figures show the simulation of the electric field for the TEM grid and membrane unit cell performed in COMSOL. (a) shows the geometric domain for simulation. (b) highlights the fluid filled domains which include the internal unit cells of the two grids, connected only by the membrane pores. Only one unit-cell is highlighted in blue for clarity. (c) shows the surface boundaries used as the electrodes. (d) shows the electric field within the pores, and the electric field lines initiating from the positive electrode surface and terminating at the ground electrode surface. The average electric field strength within the pores is 200 V/cm.

The simulation shows an electric field strength in the range of 200 to 300 V/cm. This is lower than the result obtained by the ideal equation for calculating the electric field but can be attributed to the variation distance of the unit cell surfaces to each individual pore. However, this electric field strength is higher than the one generated in the capillary in the previous chapter indicating it will be sufficient. Attempt were made at a full 3D simulation

involving fluid flow and TDS coupling, but this proved to be too computationally demanding and a 2D simulation was developed instead. The 2D cross section of the simulation domain is shown in Figure 5.4. The domain represents two unit cells stacked vertically. The eight connecting regions represent the pores. In the leftmost image, to the left of the pores, the blue lines represent an electric potential of 0.5 V. To the right of the pores is ground. The central image shows the spatially distributed potential field. The rightmost image shows the electric field. The strength of the electric field within the pores is between 100 to 150 V/cm. Regions of high electric field strength occur at the corners of the pore. The values generated in this 2D simulation will not be as accurate as a full 3D simulation but can still provide insight into the behaviour of the concentration field.



Figure 5.4 The first image shows the 2D simulation domain of the unit cell and membrane. The highlighted regions to the left and right of the pores are the positive and ground potentials respectively. The central image shows the electric potential field. The rightmost image shows the electric field with an average strength of 100 V/cm within the pores.

A time dependent study was conducted using the electric field shown in Figure 5.4. The charge of the Ponceau S is set to $z=-4$, and a constant flow rate of 10 nL/min is applied. Figure 5.5 illustrates the transient behavior of the molecule. The first two rows of the image sequence shows the molecule concentrating at the electrode walls. The electric field in the two central pores is too weak and allows a fraction of the sample to pass through, indicating the flow rate is too high. At $t = 60s$, the electric field is removed, allowing the molecule to

elute out of the domain.

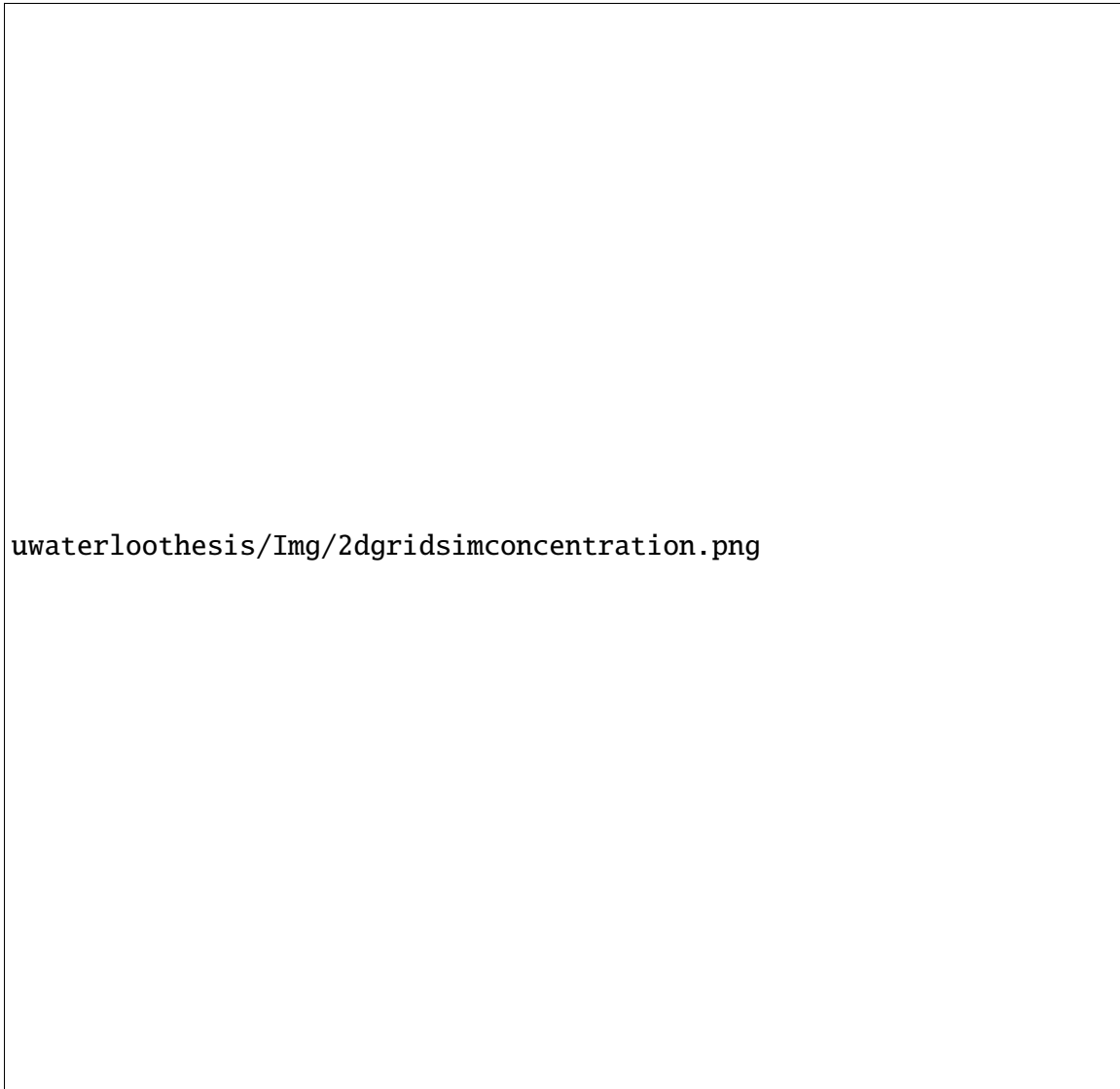


Figure 5.5 Time dependent study of the concentration field of Ponceau S. Flow rate at the left most boundary is 10 nL/min. At $t = 60s$, the electric field is removed, and the molecule elutes through the pores.

The simulation shown in Figure 5.5 showed promising results and justified the development of an experimental system.

5.2.4 Enclosure Design

In order to hold the grid-membrane-grid structure together, an enclosure was designed and machined. Other design criteria included a way of creating a water-tight seal, connecting the grids to a power supply, and a mechanism to clamp the enclosure together. Two iterations of the enclosure were made and the model of the assembly is shown in Figure 5.6. Borrowing vocabulary from the medical industry, the *proximal* connector is defined as the connector half that is closest and attached directly to the sample syringe, and the *distal* connector being the end furthest from the syringe. The proximal connector has a recessed seat for the grid-membrane-grid structure to sit. The grid tabs also have an alignment feature so that the tabs are always aligned 90 degrees apart. Steel spring pins which have a slot down one side, are pressed into the proximal connector. The slot serves to connect electrical wire which can be hooked up to a power supply. The spring pins make electrical contact with the grid tabs. The distal connector was designed to compress the grids along the rim. This is highlighted as the *gasket zone* in Figure 5.6. The gap was designed so that when the two connectors are compressed together, all of the forces are transmitted through the gasket zone. The delicate nature of aligning the grids meant the best way of compressing the connector halves together would be with pure translation. The lack of rotational symmetry of the internal feature prevented any rotation of the connectors during assembly. The inlet and outlet of the connectors are designed to work exclusively with flangeless tube end fittings. The zoomed in region of the assembly shows the 1/16" diameter bore with a flat end, which enables the end of a 1/16" diameter tubing to have a flush connection. The material of the connectors needed to be insulating, so thermoplastics were an obvious choice. Polyvinyl chloride (PVC) thermoplastic was chosen for its machinability, chemical compatibility, and was readily available at the time. Machine drawings for the device are presented in Appendix C.

uwaterloothesis/Img/LVSystemexplodedview.pdf

Figure 5.6 Exploded view of the low voltage device assembly. The cross sectional view shows the device fully assembled. The magnified region highlights the points of contact between the device and the TEM grids.

To PCTE membranes are supplied as 13 mm diameter discs. To cut the 3 mm diameter membrane, a Cricut Maker was used. The Cricut Maker is a computer-controlled pattern cutter intended for materials such as fabrics, paper, and vinyl. The machine uses a sticky mat to grip materials while being cut. This proved more than sufficient for creating test membranes. The assembly of the device is shown in Figure 5.7. Figure 5.7a shows the proximal connector with red and black wires connected to the spring pins. Figure 5.7b the proximal grid and membrane sitting in the recessed groove. Figure 5.7c shows the distal grid added and rotated 90 degrees. The end of the spring pins sit higher than the recessed groove causing the grids to not sit flush. This was done intentionally to ensure electrical contact after the connectors are compressed. Figure 5.7d shows the assembled low voltage device, which is secured by five bolts to apply an evenly distributed compression. Figure 5.7e shows how a syringe with a sample is connected to the low voltage device.

uwaterloothesis/Img/LVSystemassembly.png

Figure 5.7 Assembly of low voltage separation system. The diameter of the TEM grid is 3 mm.

Using a 5 times objective lens, Figure 5.8 shows the mesh-grid-mesh structure. The membrane is slightly transparent and allows the proximal mesh pattern to be seen below the membrane. An unexpected discovery was the misalignment of the proximal and distal mesh when rotated 90 degrees. This is due to the fact that the hole pattern of the mesh is not a perfect square.

uwaterloothesis/Img/meshoffset.pdf

Figure 5.8 Magnified view of the grid-membrane-grid assembled in the low voltage device. The magnified image was taken with a 5x objective lens. The distal grid mesh pattern is in the forefront of the image, followed by the membrane and proximal grid. The translucent membrane shows the distal and proximal are not perfectly aligned when rotated by 90 degrees, due to the rectangular shape of the mesh.

The misalignment of the grids may affect the electric field and flow rates through individual pores. If some pores are blocked, by conservation of mass the remaining pores would experience a higher average flow rate.

5.3 Experimental Results

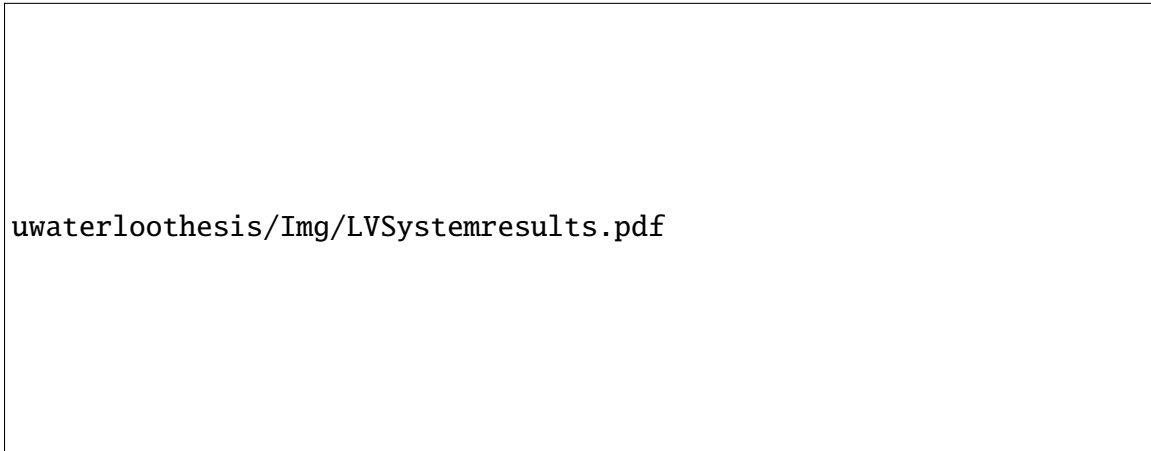
The design of the low voltage enclosure prohibited imaging at the membrane. Therefore, to evaluate the device, a dilute mixture of Ponceau S was prepared. Another lab member graciously supplied the Ponceau S solution for these experiments. The composition of the solution was 0.1% Ponceau S w/v, 20% glycerol v/v. This solution had an intense reddish-pink hue. The solution was further diluted with DI water in a 2:25 ratio by volume. This new solution had a very light pink hue.

A 100 μ L syringe was filled with the light pink solution. The assembled low voltage device was attached to the syringe and installed on the syringe pump. A camera phone was held over the end of the outlet tube to image the bubble which formed as fluid was pumped. Table 5.3 shows the test conditions and qualitative results.

Table 5.3 Test parameters for Low Voltage Separation of Ponceau S

Flow Rate (nL/min)	Voltage, V	Current, (μ A)	Comments
800	0.50	44	No
800	0.50	10	No colour change
800	0.50	6	No colour change
800	3.00	1500	Colour reduced intensity
600	3.00	750	Appears clear
600	2.00	40-75	Appears clear
200	0.70	13-140	Appears clear

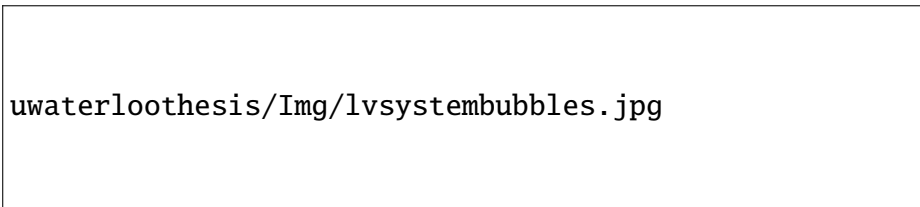
Images showing the reduce colour of the dilute Ponceau S solution is shown in Figure 5.9. Figure 5.9a shows the formation of a bubble at the tip out the outlet with a noticeable pink hue. Figure 5.9b is fully formed bubble which is used as the control image to compare visual differences. Once the voltage was applied, the bubble was wiped away with a cloth. After 5 minutes and multiple wipes of the bubbles, a bubbled formed with no colour as shown in Figure 5.9c. That image and the control were then modified using software to apply an equal increase in the saturation level, which can be seen in the Figures 5.9d and 5.9e. This was done to emphasize the colour difference between the images.



uwaterloothesis/Img/LVSystemresults.pdf

Figure 5.9 Separation results of Ponceau S. Images of the separation process taken with a camera phone (a) Image of the solution as it appeared after pumping through the membrane at 800 nL/min without an applied voltage. This image shows a light pink hue which was noticeable to the naked eye. (b) Control image used as the colour reference. (c) Applied voltage of 3.00 V and 800 nL/min. (d) and (e) are post-processed images of (b) and (c) with an equally applied increase in saturation levels to enhance the colour difference.

Applied voltages above 3 volts consistently produced bubbles in the system. The rate of bubble production was found to increase in response to an increase in voltage. Figure 5.10 shows bubbles in the outlet stream with an applied potential of 5.0 V. The Pourbaix diagram of water suggests that at $\text{pH} = 7$ and a positive potential greater than 0.6 volts relative to ground, electrolysis should occur to produce O_2 gas. The generation of O_2 gas is assumed to have occurred for voltages above this threshold, but the volumetric rate of generation was too small to form bubbles of a sufficient size to see.



uwaterloothesis/Img/lvsystembubbles.jpg

Figure 5.10 Bubbles consistently generated from electrolysis during Ponceau S separations with applied voltages above 3 volts.

After experiments, the membrane was removed from the device and viewed under a microscope as shown in Figure 5.11. The left image is at 5 times magnification and shows the pores and an impression of the mesh. The right image taken at 10 times magnification

at the rim of the mesh shows the mesh deforms enough to capture the features of the mesh but is tough enough to withstand the pressures involved.

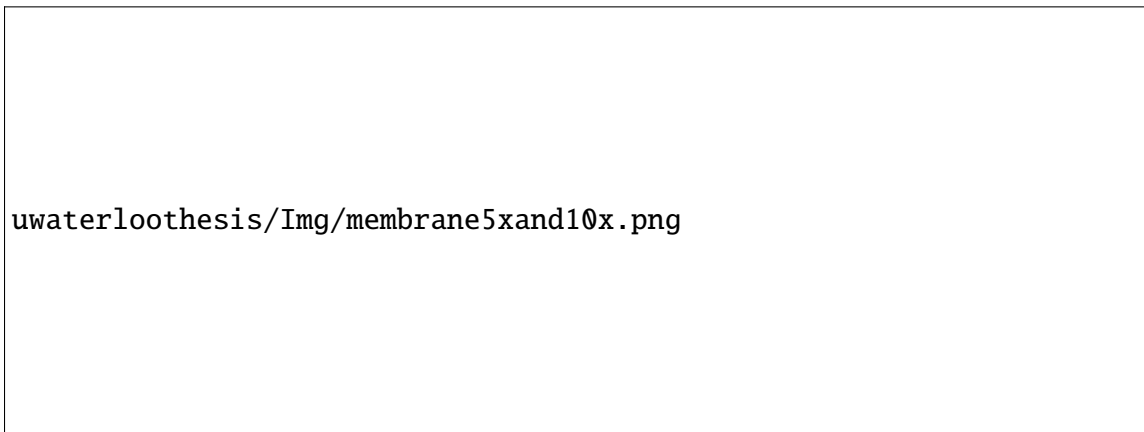


Figure 5.11 (left) image of the PCTE membrane after separation experiments showing the deformation of the membrane. (right) the same membrane at 10x magnification to show the mesh grid imprint.

The results obtained during experiments do show that the dye did respond to the applied electric field, however, the effect was difficult to quantify in terms of effectiveness.

5.4 Recommendations

The design shows promise as an alternative direction to capillary based designs. Improving the design of the mesh-grid-mesh structure to more closely resemble the design in Figure 5.1 would make numerical simulations less computationally expensive and more accurate. One potential alternative as previously mentioned would be to use gold coated membranes. The advantage of the membrane approach is scalability since the throughput of the membrane-based device is proportional to the surface area. Large membrane sheets with the proper enclosure design to pave the way for milligram per hour or potentially gram per hour scale protein separation and collection. The choice of electrode material should be investigated to ensure chemical compatibility and avoid undesirable electrochemical reactions. The Ponceau S solution included glycerol, which increased the viscosity and lowered the electrophoretic mobility. Future experiments should be done without glycerol.

Chapter 6

Conclusions and Recommendations

The purpose of this work was to develop a novel electrophoretically driven method for separating proteins which had the potential for delivering high throughput and high resolution separations. Another driving factor was developing a complete system which could perform at a fraction of the cost of commercial systems. Systems like High Performance Liquid Chromatography (HPLC) achieve high throughput and resolution separations. The high pressures involved require thoughtful engineering to safely construct such a device which drives costs to levels only large research institutions can afford. Isoelectric focusing is a high-resolution separation technique but does not offer high throughput potential. Separations of proteins within a difference of 1.5 pH units at a rate of 180 nL/min has been demonstrated (Chapter 4). The construction of a novel low voltage device using membranes rather than glass capillaries demonstrated the ability to generate an adequate electric field with voltages as low as 0.7 V to separate the charged salt Ponceau S (Chapter 5). Such low voltages can avoid electrolysis entirely.

6.1 Recommendations for Future Works

The work presented in this thesis is a proof of concept towards the path of developing a high-performance separation system. Future improvements will need to first focus on

improving the resolution of the system, followed by determining the maximum throughput capabilities.

6.1.1 High Resolution Separation

In the context of pH dependent separations, high resolution separations are realized when two proteins which differ in isoelectric points by less than 0.5 pH units can be separated. A system which can control the pH of the buffer solution to a higher degree of precision is a necessary step. Temperature variations caused by Joule heating leads to changes in pH, which makes controlling the pH to a high degree of precision very difficult. One solution would be to explore carrier ampholytes with a narrow cut in pH. This has been shown to have a very low current draw with high electric field strengths [65]. The electrophoretic mobility of neutral proteins has been shown to be nearly constant in pH ranges between 6 and 9. High resolution separations will be easier to achieve with proteins outside of this range as their electric mobility slope is steeper. The nature of the technique requires proteins to concentrate at the inlet of the separation capillary. This may put limitations on the run time of separations as concentrations of species build up at the membrane and may cause drastic changes in the electric field. Future work should explore the capacity of the system, i.e., how many proteins can be successfully separated from a narrow range of pH, and what challenges would arise.

6.1.2 Electrolysis Free Protein Separations

As part of addressing the throughput capabilities of the system, the low voltage device shows promise in scalability and high electric field strengths while avoiding electrolysis. Optimization of the electrode and membrane construction is the first step. This may come in the form of using membranes with a conductive coating. Another direction would be to first construct a laminate in a conductor-insulator-conductor construction, and then creating a highly controlled hole-pattern which can be etched through. After optimizing the laminate geometry and construction, the area can be increased far beyond the mm² area scale. One

can imagine a device with the surface area of a table, pumping litre volumes per hour of sample solution, while individual pores still experience the nL/min flow rates required for high resolution separations. The low voltage not only eliminates the effects of electrolysis, but also the need for high voltage equipment. Future devices could be controlled by low voltage electronics such as an Arduino or Raspberry Pi. This device is intended to work with the pHGEMBE method; future works should explore a comparison in performance between the low voltage device and a standard capillary cartridge with respect to throughput, capacity, and resolution.

References

- [1] MarketWatch, Protein Purification & Isolation Market 2020 Size, Growth Opportunities, Trends by Manufacturers, Regions, Application & Forecast to 2025 - MarketWatch, 2020.
- [2] I. Rodríguez-Ruiz, V. Babenko, S. Martínez-Rodríguez, J. A. Gavira, Protein separation under a microfluidic regime, *The Analyst* 143 (2018) 606–619. URL: <https://pubs.rsc.org/en/content/articlepdf/2018/an/c7an01568b>. doi:10.1039/C7AN01568B.
- [3] K. Chandramouli, P.-Y. Qian, Proteomics: Challenges, Techniques and Possibilities to Overcome Biological Sample Complexity, *Human Genomics and Proteomics* 1 (2009). URL: <https://www.ncbi.nlm.nih.gov/pmc/articles/PMC2950283/pdf/HGP2009-239204.pdf>. doi:10.4061/2009/239204.
- [4] W. C. Cho, Proteomics Technologies and Challenges, *Genomics, Proteomics & Bioinformatics* 5 (2007) 77–85. URL: <https://linkinghub.elsevier.com/retrieve/pii/S1672022907600187>. doi:10.1016/S1672-0229(07)60018-7.
- [5] A. Blokzijl, M. Friedman, F. Pontén, U. Landegren, Profiling protein expression and interactions: proximity ligation as a tool for personalized medicine, *Journal of Internal Medicine* 268 (2010) 232–245. URL: <http://doi.wiley.com/10.1111/j.1365-2796.2010.02256.x>. doi:10.1111/j.1365-2796.2010.02256.x.
- [6] A. C. Timm, P. G. Shankles, C. M. Foster, M. J. Doktycz, S. T. Retterer, Toward Microfluidic Reactors for Cell-Free Protein Synthesis at the Point-of-Care, *Small* 12 (2016) 810–817. doi:10.1002/smll.201502764.
- [7] A. D. Stroock, Microfluidics, in: *Optical Biosensors*, Elsevier, 2008, pp. 659–681. URL: <https://linkinghub.elsevier.com/retrieve/pii/B978044453125450019X>. doi:10.1016/B978-044453125-4.50019-X.
- [8] E. M. Purcell, Life at low Reynolds number, *American Journal of Physics* 45 (1977) 3–11.

- URL: <http://aapt.scitation.org/doi/10.1119/1.10903>. doi:10.1119/1.10903.
- [9] H. Bruus, *Theoretical Microfluidics*, volume 38, Oxford University Press, 2005.
- [10] B. Kirby, *Micro- and Nanoscale Fluid Mechanics*, Cambridge University Press, Cambridge, 2010. URL: <http://ebooks.cambridge.org/ref/id/CB09780511760723>. doi:10.1017/CB09780511760723.
- [11] A. d. Campo, C. Greiner, SU-8: a photoresist for high-aspect-ratio and 3D sub-micron lithography, *Journal of Micromechanics and Microengineering* 17 (2007) R81–R95. URL: <http://stacks.iop.org/0960-1317/17/i=6/a=R01?key=crossref.5f54d4397fa259758a20d0ac229f2a2c>. doi:10.1088/0960-1317/17/6/R01.
- [12] T. Glawdel, *Design, Fabrication and Characterization of Electrokinetically Pumped Microfluidic Chips for Cell Culture Applications*, 2008. URL: <http://hdl.handle.net/10012/3576>.
- [13] A. Sze, D. Erickson, L. Ren, D. Li, Zeta-potential measurement using the Smoluchowski equation and the slope of the current–time relationship in electroosmotic flow, *Journal of Colloid and Interface Science* 261 (2003) 402–410. URL: <https://linkinghub.elsevier.com/retrieve/pii/S0021979703001425>. doi:10.1016/S0021-9797(03)00142-5.
- [14] Z. A. Almutairi, T. Glawdel, C. L. Ren, D. A. Johnson, A Y-channel design for improving zeta potential and surface conductivity measurements using the current monitoring method, *Microfluidics and Nanofluidics* 6 (2009) 241–251. URL: <http://link.springer.com/10.1007/s10404-008-0320-6>. doi:10.1007/s10404-008-0320-6.
- [15] T. Glawdel, C. L. Ren, Electro-osmotic flow control for living cell analysis in microfluidic PDMS chips, *Mechanics Research Communications* 36 (2009) 75–81. URL: <https://linkinghub.elsevier.com/retrieve/pii/S0093641308000803>. doi:10.1016/j.mechrescom.2008.06.015.
- [16] M. Courtney, C. L. Ren, Counter-flow gradient electrophoresis for focusing and elution, *Electrophoresis* 40 (2018) elps.201800376. URL: <https://onlinelibrary.wiley.com/doi/abs/10.1002/elps.201800376>. doi:10.1002/elps.201800376.
- [17] A. Persat, M. E. Suss, J. G. Santiago, Basic principles of electrolyte chemistry for microfluidic electrokinetics. Part II: Coupling between ion mobility, electrolysis, and acid–base equilibria, *Lab on a Chip* 9 (2009) 2454. URL: <http://xlink.rsc.org/?DOI=b906468k>. doi:10.1039/b906468k.

- [18] J. P. Landers (Ed.), *Handbook of Capillary and Microchip Electrophoresis and Associated Microtechniques*, 3 ed., CRC Press, Boca Raton, 2007. URL: <https://www.taylorfrancis.com/books/9781420004953>. doi:10.1201/9781420004953.
- [19] A. Persat, R. D. Chambers, J. G. Santiago, Basic principles of electrolyte chemistry for microfluidic electrokinetics. Part I: Acid–base equilibria and pH buffers, *Lab on a Chip* 9 (2009) 2437. URL: <http://xlink.rsc.org/?DOI=b906465f>. doi:10.1039/b906465f.
- [20] E. F. Fabrizio, A. Nadim, J. D. Sterling, Resolution of Multiple ssDNA Structures in Free Solution Electrophoresis, *Analytical Chemistry* 75 (2003) 5012–5021. URL: <https://pubs.acs.org/sharingguidelineshttps://pubs.acs.org/doi/10.1021/ac034326c>. doi:10.1021/ac034326c.
- [21] D. Ross, M. Gaitan, L. E. Locascio, Temperature Measurement in Microfluidic Systems Using a Temperature-Dependent Fluorescent Dye, *Analytical Chemistry* 73 (2001) 4117–4123. URL: <https://pubs.acs.org/doi/10.1021/ac0103701>. doi:10.1021/ac0103701.
- [22] E. Grushka, R. M. McCormick, J. J. Kirkland, Effect of temperature gradients on the efficiency of capillary zone electrophoresis separations, *Analytical Chemistry* 61 (1989) 241–246. URL: <https://pubs.acs.org/doi/abs/10.1021/ac00178a011>. doi:10.1021/ac00178a011.
- [23] X. Xuan, Joule heating in electrokinetic flow, *Electrophoresis* 29 (2008) 33–43. URL: <http://doi.wiley.com/10.1002/elps.200700302>. doi:10.1002/elps.200700302.
- [24] A. Beskok, J. Hahm, P. Dutta, Electrokinetic Transport Phenomena in Micro-Fluidics, in: *Micromechanics and Nanoscale Effects*, 2004, pp. 81–116. URL: http://link.springer.com/10.1007/978-94-007-1013-9_4. doi:10.1007/978-94-007-1013-9{_}4.
- [25] G. I. Taylor, Dispersion of soluble matter in solvent flowing slowly through a tube, *Proceedings of the Royal Society of London. Series A. Mathematical and Physical Sciences* 219 (1953) 186–203. URL: <https://royalsocietypublishing.org/doi/10.1098/rspa.1953.0139>. doi:10.1098/rspa.1953.0139.
- [26] S. Datta, S. Ghosal, Characterizing dispersion in microfluidic channels, *Lab on a Chip* 9 (2009) 2537. URL: <http://xlink.rsc.org/?DOI=b822948c>. doi:10.1039/b822948c.
- [27] S. Devasenathipathy, J. Santiago, Electrokinetic Flow Diagnostics, in: K. S. Breuer (Ed.), *Microscale Diagnostic Techniques*, Springer-Verlag, Berlin/Heidelberg, 2005, pp. 113–154. URL: http://link.springer.com/10.1007/3-540-26449-3_3. doi:10.1007/3-540-26449-3{_}3.

- [28] X. Chen, J. Shen, Review of membranes in microfluidics, 2017. URL: <http://doi.wiley.com/10.1002/jctb.5105>. doi:10.1002/jctb.5105.
- [29] I. M. T. A. Shigidi, The Use of Bubble Point Test in Membrane Characterisation, *American Journal of Science and Technology* 1 (2014) 140–144. URL: <http://www.aascit.org/journal/ajst>.
- [30] E. Drioli, A. Criscuoli, E. Curcio, *Membrane Contactors: Fundamentals, Applications and Potentialities*, 1st ed., Elsevier, Amsterdam, 2006.
- [31] Q. Mao, J. Pawliszyn, Capillary isoelectric focusing with whole column imaging detection for analysis of proteins and peptides., *Journal of biochemical and biophysical methods* 39 (1999) 93–110. URL: <http://www.ncbi.nlm.nih.gov/pubmed/10344503>.
- [32] F. Li, R. M. Guijt, M. C. Breadmore, Nanoporous Membranes for Microfluidic Concentration Prior to Electrophoretic Separation of Proteins in Urine, *Analytical Chemistry* 88 (2016) 8257–8263. URL: <https://pubs.acs.org/doi/10.1021/acs.analchem.6b02096>. doi:10.1021/acs.analchem.6b02096.
- [33] P. Apel, I. Blonskaya, S. Dmitriev, O. Orelovitch, B. Sartowska, Structure of polycarbonate track-etch membranes: Origin of the “paradoxical” pore shape, *Journal of Membrane Science* 282 (2006) 393–400. URL: <https://linkinghub.elsevier.com/retrieve/pii/S0376738806003814>. doi:10.1016/j.memsci.2006.05.045.
- [34] A. Brunning, *A guide to the twenty common amino acids*, 2014. URL: <https://www.compoundchem.com/2014/09/16/aminoacids/>.
- [35] H.-T. Lam, J. Josserand, N. Lion, H. H. Girault, Modeling the Isoelectric Focusing of Peptides in an OFFGEL Multicompartment Cell, *Journal of Proteome Research* 6 (2007) 1666–1676. URL: <https://pubs.acs.org/doi/abs/10.1021/pr0606023>. doi:10.1021/pr0606023.
- [36] C. Armarego, Wilfred Chai, *Purification of Laboratory Chemicals*, Elsevier, 2013. URL: <https://linkinghub.elsevier.com/retrieve/pii/C20090265895>. doi:10.1016/C2009-0-26589-5.
- [37] E. J. Cohn, The Physical Chemistry of the Proteins, *Physiological Reviews* 5 (1925) 349–437. URL: <https://www.physiology.org/doi/10.1152/physrev.1925.5.3.349>. doi:10.1152/physrev.1925.5.3.349.
- [38] W. B. Hardy, W. C. D. Whetham, On the coagulation of proteid by electricity, *The Journal of Physiology* 24 (1899) 288–304. doi:10.1113/jphysiol.1899.sp000758.

- [39] D. Malamud, J. W. Drysdale, Isoelectric points of proteins: A table, *Analytical Biochemistry* 86 (1978) 620–647. doi:10.1016/0003-2697(78)90790-X.
- [40] T. Ahamed, B. K. Nfor, P. D. Verhaert, G. W. van Dedem, L. A. van der Wielen, M. H. Eppink, E. J. van de Sandt, M. Ottens, pH-gradient ion-exchange chromatography: An analytical tool for design and optimization of protein separations, *Journal of Chromatography A* 1164 (2007) 181–188. URL: <https://linkinghub.elsevier.com/retrieve/pii/S0021967307011806>. doi:10.1016/j.chroma.2007.07.010.
- [41] R. G. Wolfe, J. B. Neilands, Some Molecular and Kinetic Properties of Heart Malic Dehydrogenase, *Biological Chemistry* (1956). URL: <http://www.jbc.org/>.
- [42] M. E. Young, P. A. Carroad, R. L. Bell, Estimation of diffusion coefficients of proteins, *Biotechnology and Bioengineering* 22 (1980) 947–955. URL: <http://doi.wiley.com/10.1002/bit.260220504>. doi:10.1002/bit.260220504.
- [43] H. Fischer, I. Polikarpov, A. F. Craievich, Average protein density is a molecular-weight-dependent function, *Protein Science* 13 (2009) 2825–2828. URL: <http://doi.wiley.com/10.1110/ps.04688204>. doi:10.1110/ps.04688204.
- [44] J. V. Nauman, P. G. Campbell, F. Lanni, J. L. Anderson, Diffusion of Insulin-Like Growth Factor-I and Ribonuclease through Fibrin Gels, *Biophysical Journal* 92 (2007) 4444–4450. URL: <https://linkinghub.elsevier.com/retrieve/pii/S0006349507712444>. doi:10.1529/biophysj.106.102699.
- [45] P. G. Righetti, *Isoelectric focusing : theory, methodology, and applications*, 1st ed., Elsevier, Amsterdam, 1983.
- [46] T. Huang, Illustration of capillary diameter transfer technology (CDTT) maintaining the separation of focused peaks, 2019. URL: <https://ceinfinite.com/technologies-preparative-icief/>.
- [47] J. G. Shackman, M. S. Munson, D. Ross, Gradient Elution Moving Boundary Electrophoresis for High-Throughput Multiplexed Microfluidic Devices, *Analytical Chemistry* 79 (2007) 565–571. URL: <https://pubs.acs.org/doi/10.1021/ac061759h>. doi:10.1021/ac061759h.
- [48] D. Ross, E. F. Romantseva, Gradient Elution Moving Boundary Electrophoresis with Channel Current Detection, *Analytical Chemistry* 81 (2009) 7326–7335. URL: <https://pubs.acs.org/doi/10.1021/ac901189y>. doi:10.1021/ac901189y.

- [49] M. Bier, New principle of preparative electrophoresis, *Science* 125 (1957) 1084–1085. URL: <https://www.jstor.org/stable/1752439>. doi:10.1126/science.125.3257.1084.
- [50] Ion Exchange Chromatography Principles and Methods, 2004. URL: <https://cdn.gelifesciences.com/dmm3bwsv3/AssetStream.aspx?mediaformatid=10061&destinationid=10016&assetid=13101>.
- [51] J. W. Jorgenson, K. D. Lukacs, Zone electrophoresis in open-tubular glass capillaries, *Analytical Chemistry* 53 (1981) 1298–1302. URL: <https://pubs.acs.org/doi/abs/10.1021/ac00231a037>. doi:10.1021/ac00231a037.
- [52] A. S. Zarabadi, Optimization of Capillary Electrophoresis With Imaging Detection for Estimation of Diffusion Coefficients, 2015. URL: <http://hdl.handle.net/10012/9353>.
- [53] M. E. Sastre de Vicente, The Concept of Ionic Strength Eighty Years after Its Introduction in Chemistry, *Journal of Chemical Education* 81 (2004) 750. URL: <https://pubs.acs.org/doi/abs/10.1021/ed081p750>. doi:10.1021/ed081p750.
- [54] S. S. Bahga, M. Bercovici, J. G. Santiago, Ionic strength effects on electrophoretic focusing and separations, *Electrophoresis* 31 (2010) 910–919. URL: <http://doi.wiley.com/10.1002/elps.200900560>. doi:10.1002/elps.200900560.
- [55] R. M. Kramer, V. R. Shende, N. Motl, C. N. Pace, J. M. Scholtz, Toward a Molecular Understanding of Protein Solubility: Increased Negative Surface Charge Correlates with Increased Solubility, *Biophysical Journal* 102 (2012) 1907–1915. URL: <https://linkinghub.elsevier.com/retrieve/pii/S0006349512002822>. doi:10.1016/j.bpj.2012.01.060.
- [56] D. Erickso, D. Li, Microscale Flow and Transport Simulation for Electrokinetic and Lab-on-Chip Applications, in: M. Ferrari, R. Bashir, S. Wereley (Eds.), *BioMEMS and Biomedical Nanotechnology: Volume IV: Biomolecular Sensing, Processing and Analysis*, Springer US, Boston, MA, 2007, pp. 277–300. URL: http://link.springer.com/10.1007/978-0-387-25845-4_14. doi:10.1007/978-0-387-25845-4_{_}14.
- [57] Z. Zhao, A. Fisher, D. Cheng, Numerical Simulation in Microfluidics and the Introduction of the Related Software, in: *Microfluidics: Fundamental, Devices and Applications*, Wiley-VCH Verlag GmbH & Co. KGaA, Weinheim, Germany, 2018, pp. 147–174. URL: <https://app.knovel.com/hotlink/pdf/id:kt011NAH41/microfluidics-fundamentals/>

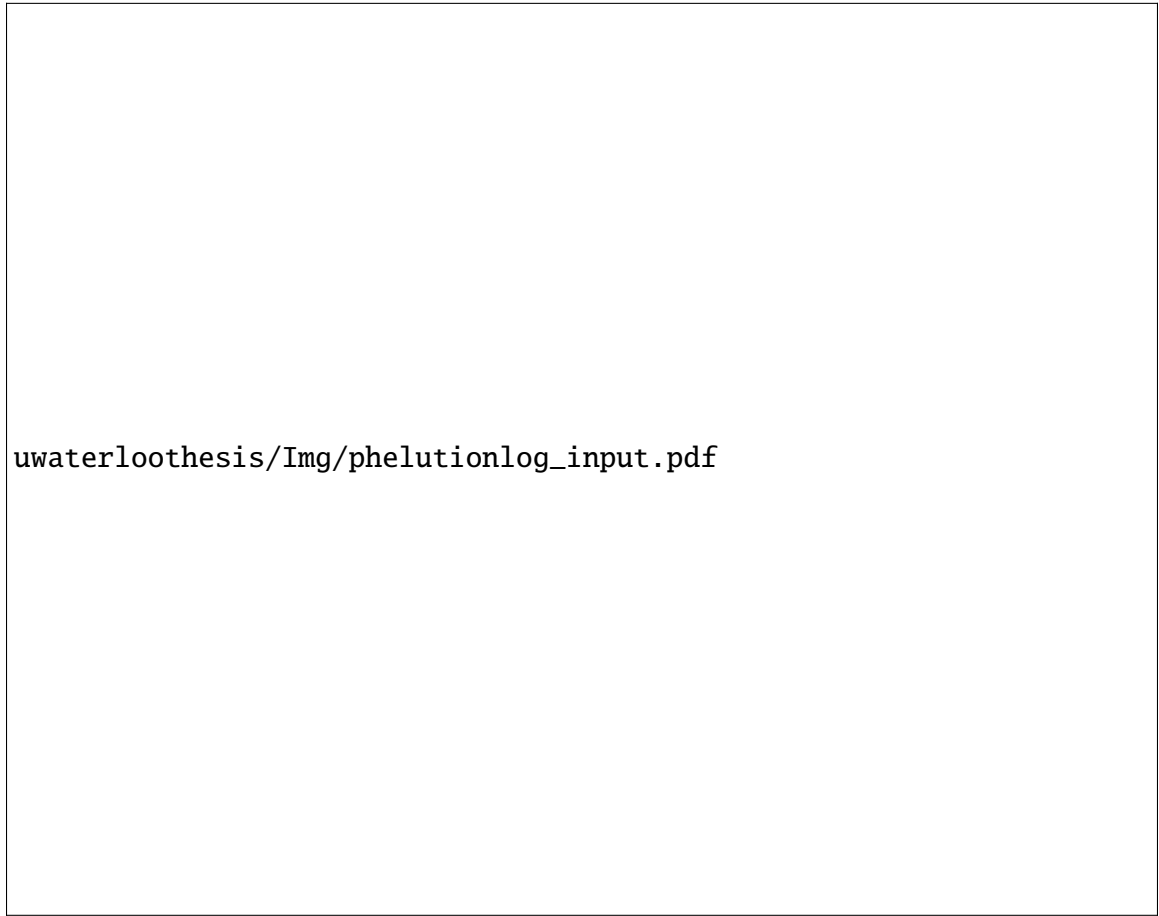
- continuum-method-cm<http://doi.wiley.com/10.1002/9783527800643.ch4>.
doi:10.1002/9783527800643.ch4.
- [58] S. V. Ermakov, S. C. Jacobson, J. M. Ramsey, Computer Simulations of Electrokinetic Transport in Microfabricated Channel Structures, *Analytical Chemistry* 70 (1998) 4494–4504. URL: <https://pubs.acs.org/doi/10.1021/ac980551w>. doi:10.1021/ac980551w.
- [59] P. Dutta, A. Beskok, T. C. Warburton, Numerical Simulation of Mixed Electroosmotic/Pressure Driven Microflows, *Numerical Heat Transfer, Part A: Applications* 41 (2002) 131–148. URL: <http://www.tandfonline.com/doi/abs/10.1080/104077802317221366>. doi:10.1080/104077802317221366.
- [60] Elveflow, Stability of syringe pumps: A question of flow rate, 2020. URL: <https://www.elveflow.com/microfluidic-reviews/microfluidic-flow-control/syringe-pumps-and-microfluidics/>.
- [61] M. Horká, T. Willmann, M. Blum, P. Nording, Z. Friedl, K. Šlais, Capillary isoelectric focusing with UV-induced fluorescence detection, *Journal of Chromatography A* 916 (2001) 65–71. URL: <https://linkinghub.elsevier.com/retrieve/pii/S0021967300010694>. doi:10.1016/S0021-9673(00)01069-4.
- [62] T. Glawdel, Z. Almutairi, S. Wang, C. Ren, Photobleaching absorbed Rhodamine B to improve temperature measurements in PDMS microchannels, *Lab Chip* 9 (2009) 171–174. URL: <http://xlink.rsc.org/?DOI=B805172K>. doi:10.1039/B805172K.
- [63] Y.-C. Lin, Design of low voltage-driven capillary electrophoresis chips using moving electrical fields, *Sensors and Actuators B: Chemical* 80 (2001) 33–40. URL: <https://linkinghub.elsevier.com/retrieve/pii/S0925400501008681>. doi:10.1016/S0925-4005(01)00868-1.
- [64] S. D. Cramer, J. Covino, Bernard S., The Water E-pH Diagram - Knovel, in: *ASM Handbook, Volume 13A - Corrosion: Fundamentals, Testing, and Protection - 6. Potential versus pH (Pourbaix) Diagrams.*, ASM International, 2003, p. 21. URL: <https://app.knovel.com/hotlink/pdf/id:kt007P0QE3/asm-handbook-volume-13a/potential-versus-ph-pourbaix>.
- [65] J.-M. Busnel, F. Kilár, V. Kašička, S. Descroix, M.-C. Hennion, G. Peltre, Carrier ampholytes-based capillary electrophoresis as an alternative to capillary zone electrophoresis in classical background electrolytes, *Journal of Chromatography A* 1087 (2005) 183–

188. URL: <https://linkinghub.elsevier.com/retrieve/pii/S0021967305006631>.
doi:10.1016/j.chroma.2005.03.109.

Appendix A


Test Logging

This appendix provides a sample of the live output of a spreadsheet which records data from the high voltage supply. The spreadsheet also functions to record all details of the experiment including sample composition, buffer composition, flow rates, and times. Under the "Voltage Trace File" cell, the start time records the standard time when the data logging started. The times shown on the graphs relates to the difference from this start time. The time derivative of the current (current slope) is plotted in green. Due to the high sampling rate of the high voltage system, the measured current was often noisy. A moving average was calculated to smooth out the signal. This is shown in the bottom graph for both the current and current slope. Fluctuations in the current at time 1:06:00 and 1:45:00 are directly attributed to stopping the pump and switching syringes, as described in the "Description" cells.



uwaterloothesis/Img/phelutionlog_input.pdf

Figure A.1 Form to record testing data



uwaterloothesis/Img/phelutionlog_output.pdf

Figure A.2 Live voltage and current plots.

Appendix B

Mass Concentration Factor

Determining the total concentration of the purified sample could be simulated accurately if the entire domain of the capillary cartridge is modelled. Since the length of the capillary cartridge is orders of magnitude larger than the diameter, even a 2D simulation would take a very long time to run. A faster way is through a control volume analysis. Figure B.1 shows the control volume (CV) which includes the separation capillary where the electric field is present and the transfer capillary.

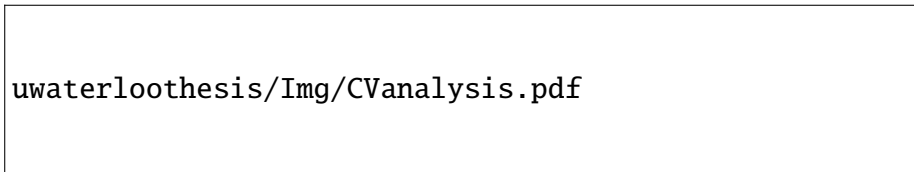


Figure B.1 Control volume analysis diagram for capillary cartridge.

As a charged protein enters the CV, it remains at the left boundary, the rate of change of mass within the CV is defined as:

$$\begin{aligned}\dot{m}_{CV} &= \rho_0 Q - \rho_{out} Q \\ \dot{m}_{CV} &= \rho_0 Q\end{aligned}\tag{B.1}$$

where \dot{m} is the mass flow rate entering the domain, Q is the volumetric flow rate set by the syringe pump, ρ_0 is the initial mass concentration entering the CV, and ρ_{out} is the mass

concentration leaving. Assuming all mass is held at the inlet by electrophoresis, ρ_{out} is zero. Separating variables and applying initial conditions that the mass within the control volume is zero, leads to the total mass accumulated within the CV, m_1 :

$$\begin{aligned} \dot{m}_{CV} &= \frac{\partial m}{\partial t} = (\rho_0 Q) \\ \int_0^{m_1} dm &= \int_0^{t_1} \rho_0 Q dt \\ m_1 &= \rho_0 Q t_1 \end{aligned} \quad (\text{B.2})$$

where t_1 is the accumulation duration.

To collect m_1 at the outlet, the volume of the separation and transfer capillary must be flushed. Ignoring diffusion, the final mass concentration can be estimated as:

$$\rho_f = \frac{m_1}{V_{CV}} = \frac{\rho_0 Q t_1}{V_{CV}} \quad (\text{B.3})$$

which can be rearranged to define the mass concentration factor, f_m :

$$f_m = \frac{\rho_f}{\rho_0} = \frac{Q t_1}{V_{CV}} \quad (\text{B.4})$$

Using the values for the capillary geometry, the control volume V_{CV} given by:

$$\begin{aligned} V_{CV} &= \frac{\pi}{4} (D_1^2 L_1 + D_2^2 L_2) \\ &= \frac{\pi}{4} [(320 \mu\text{m})^2 (50 \text{ mm}) + (50 \mu\text{m})^2 (110 \text{ mm})] \\ &= 4.24 \times 10^{-9} \text{ m}^3 \end{aligned} \quad (\text{B.5})$$

For an experiment with an accumulation duration of 180 minutes at a flow rate of 180

nL/min, the mass concentration factor is:

$$f_m = \frac{(180 \text{ nL/min})(1 \times 10^{-12} \text{ m}^3/\text{nL})(180 \text{ min})}{4.24 \times 10^{-9} \text{ m}^3} \quad (\text{B.6})$$
$$= 7.6$$

This factor is highly idealized as it does not take into account diffusion which leads to band broadening. In practice, this value will be lower as the flushed volume may be larger than the control volume defined by the capillary geometry.

Appendix C

Drawings

Machine drawings for the distal and proximal connectors were developed using SolidWorks and sent out for manufacturing.

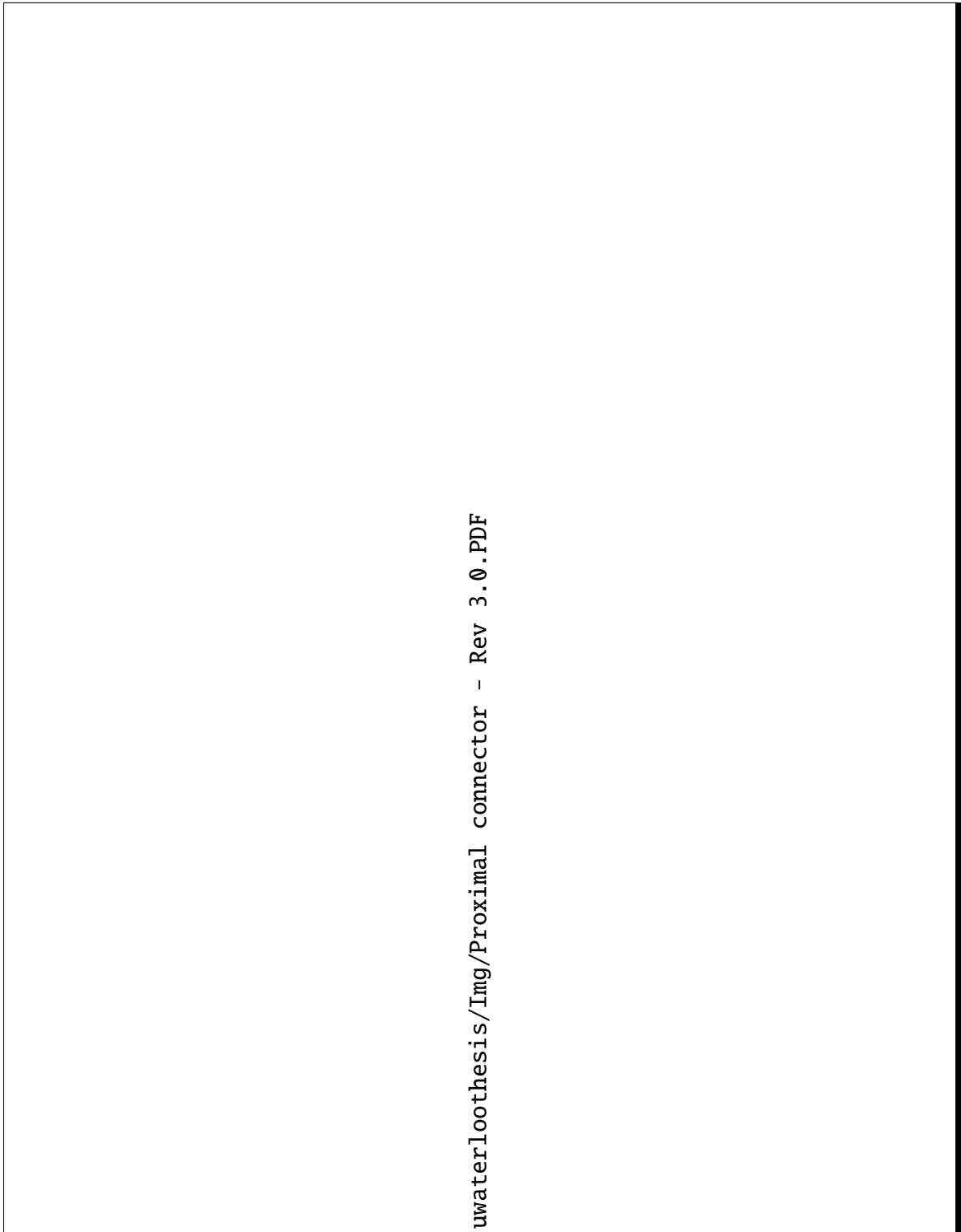
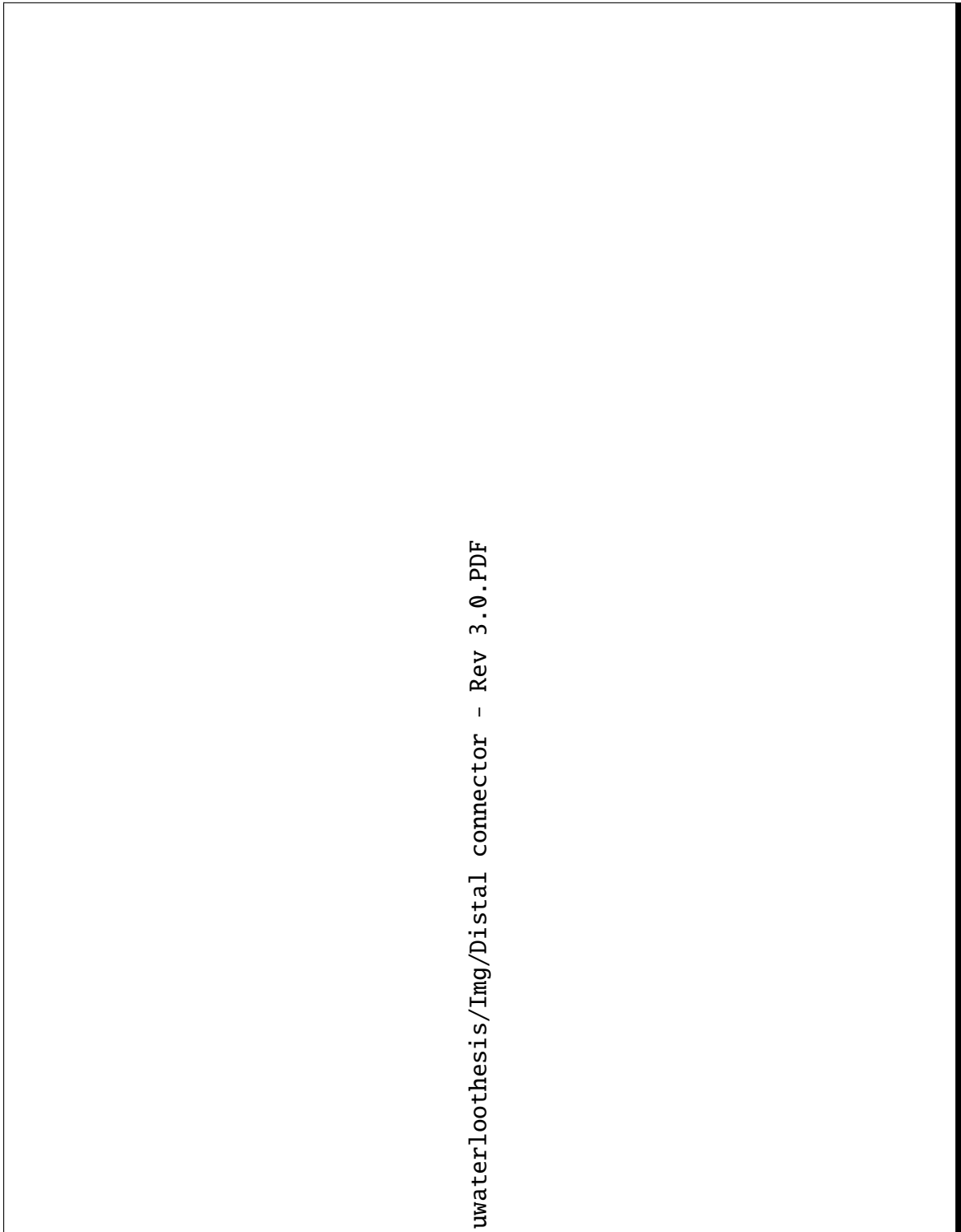


Figure C.1 Machine drawing of the proximal connector



uwaterloothesis/Img/Distal connector - Rev 3.0.PDF

Figure C.2 Machine drawing of the distal connector